



저작자표시-비영리-변경금지 2.0 대한민국

이용자는 아래의 조건을 따르는 경우에 한하여 자유롭게

- 이 저작물을 복제, 배포, 전송, 전시, 공연 및 방송할 수 있습니다.

다음과 같은 조건을 따라야 합니다:



저작자표시. 귀하는 원저작자를 표시하여야 합니다.



비영리. 귀하는 이 저작물을 영리 목적으로 이용할 수 없습니다.



변경금지. 귀하는 이 저작물을 개작, 변형 또는 가공할 수 없습니다.

- 귀하는, 이 저작물의 재이용이나 배포의 경우, 이 저작물에 적용된 이용허락조건을 명확하게 나타내어야 합니다.
- 저작권자로부터 별도의 허가를 받으면 이러한 조건들은 적용되지 않습니다.

저작권법에 따른 이용자의 권리는 위의 내용에 의하여 영향을 받지 않습니다.

이것은 [이용허락규약\(Legal Code\)](#)을 이해하기 쉽게 요약한 것입니다.

[Disclaimer](#)

공학박사 학위논문

**Development of Flexible Polymer
Electrolyte Fuel Cell Based on
Polymer Flow-Field Plates and
Silver Nanowire Current Collectors**

폴리머 유로판과 은 나노와이어 집전체 기반의
플렉서블 고분자 전해질 연료전지 개발

2016년 8월

서울대학교 대학원

기계항공공학부

박 태 현

**Development of Flexible Polymer
Electrolyte Fuel Cell Based on Polymer
Flow-Field Plates and Silver Nanowire
Current Collectors**

by

Taehyun Park

A Dissertation Submitted in Partial Fulfillment

of the Requirements for the Degree of

DOCTOR OF PHILOSOPHY

Department of Mechanical and Aerospace Engineering

Seoul National University

August 2016

Development of Flexible Polymer Electrolyte Fuel Cell Based on Polymer Flow-Field Plates and Silver Nanowire Current Collectors

지도 교수 차 석 원

이 논문을 공학박사 학위논문으로 제출함
2016 년 4 월

서울대학교 대학원
기계항공공학부
박 태 현

박태현의 박사 학위논문을 인준함
2016 년 5 월

위 원 장 _____ 안 성 훈 _____ (인)

부위원장 _____ 차 석 원 _____ (인)

위 원 _____ 전 누 리 _____ (인)

위 원 _____ 유 성 중 _____ (인)

위 원 _____ 안 지 환 _____ (인)

Abstract

Development of Flexible Polymer Electrolyte Fuel Cell Based on Polymer Flow-Field Plates and Silver Nanowire Current Collectors

Taehyun Park

Department of Mechanical and Aerospace Engineering

Seoul National University

The technological level of various electronics has been intensively progressed in 21st century. This progress has also increased the demand for portable energy storage technology due to its contribution on the miniaturization of several electronics like smartphones. A lithium-based rechargeable battery currently leads the portable energy storage market while it already approached its theoretical maximum of gravimetric and volumetric energy density. Unfortunately, the demand for portable power sources with higher energy density keeps increasing as long as the level of other electronic components continues to be highly technologized. Accordingly, it is needed to find out the alternative for current lithium-ion battery technology.

Another technological variation in future electronics is that it demands ‘flexibility’, *i.e.* ‘bendability’. So-called “wearable electronics”, including flexible displays, bent smart phones, or “epidermal electronics” have been highly spotlighted as future electronics. Here, such electronics also require portable energy sources because they are also kind of portable electronics.

This study proposes the new type of fuel cell to cope with aforementioned demand for future electronics. Flexible fuel cell, *i.e.* ‘bendable fuel cell’, was fabricated based on polymer electrolyte fuel cell (PEFC) technology which is considered as one of the candidates to overcome the limitation of current energy density arising from the lithium-ion batteries. Here, Ag nanowires were used as a current collector inside the flexible fuel cell since it is highly stretchable and bendable with reliable electrical conductivity, corrosion-resistance, and chemical stability. This property enables the Ag nanowires to be used in chemically harsh environments such as anode and cathode in fuel cells. This current collector was coated on chemically highly stable polymer, polydimethylsiloxane, to realize the flexible flow-field plates for flexible fuel cells.

The performance of the flexible fuel cell based on the aforementioned flow-field plates was measure at various bending radius. The peak power densities at flat and highly bent shapes were 43 and 71 mW/cm², respectively. The variation of the performance was related to normal compressive stress (assembly pressure) to MEA (Membrane-electrode assembly), which was calculated using FEM (Finite-element method). The result showed that the electrochemical performance is increased as the compressive stress generated by bending is increased. The EIS (Electrochemical impedance spectra) corresponding to the measured polarization curves showed that the increase of the performance resulting from bending is due to the decrease of both ohmic and charge transfer resistances. It was also successfully demonstrated that the flexible fuel cell powered a small electronic fan, showing its technical level

close to real applications.

However, the highest peak power density in twisting test was 17 mW/cm^2 , lower than that from the bending test. It is speculated that the lower peak power density resulted from the damaged MEA by twisting. In this experiment, internal stress distribution was also calculated using same FEM model as in the bending test. The result was that there was almost no difference of stress intensities on MEA between flat and twisted shapes. Instead, strain was partially very high, which was not the case in the bending test. Because gas-diffusion layer (GDL) is not stretchable while Nafion[®] is kind of stretchable polymer membrane, the detachment between GDL and Nafion[®] is induced by strain. It would lead to the loss of triple-phase boundary and resulting performance decrease inside the fuel cell. Another cause of the decrease in the performance would be the damaged GDL itself from the twisting test and regarding strain. Considering that the peak power density at flat position was 43 mW/cm^2 in the bending test, it is weird that same experiment but the peak power density of 17 mW/cm^2 is lower than one-third of that at the bending test. Accordingly, the current MEA used in normal PEFC is not suitable to be used in flexible fuel cells in that it is fragile in the stretched position. It means that it is required to develop the MEA of new structure exclusively for flexible fuel cells.

In the real use environment of flexible electronics, such electronics will be exposed to not only bending but also twisting environment. In order to investigate the compatibility of the flexible fuel cell in such environment, it was also characterized as it is under both bending and twisting loads simultaneously.

In this experiment, bending components were set to flat and 36.3 cm of bending radii and twisting angles were 0, 5, 10, 15, 20, and 25°. The measured polarization curves showed that the peak power density at flat position was 27 mW/cm² and the performance was decreased as it was twisted. Here, the power density of 27 mW/cm² is again lower than 43 mW/cm² measured in the bending test. This result corresponds with the results of twisting test. To investigate the internal stress distribution inside the fuel cell again, the stress distribution was calculated employing same FEM model as in bending and twisting test. The result showed that the bending and twisting components affect the generation of the internal compressive stress independently. Only bending component generates the compressive stress onto MEA, while twisting component does not. It means that the compressive stress partially contributed to the increase of the performance, although the MEA is permanently damaged by twisting.

It was also experimentally reproduced that the compressive stress onto MEA veritably increased the performance of the flexible fuel cell. The performance was measured together with precisely and quantitatively controlled compressive stress. The peak power density was converged to 110 mW/cm² as the compressive stress was increased. It represents the maximum of the peak power density of the flexible fuel cell with current template. It means that the performance of the flexible fuel cell can be increased more by improving the design, or components. In addition, the variation of several electrochemical constants such as an exchange current density, charge transfer coefficient and ohmic resistance with respect to the compressive stress were extracted from the experimental data. Simulation result based on a standard

polarization model of a fuel cell using the extracted electrochemical parameters corresponded well with the experimental data reported in the literature. It means that the performance of the flexible fuel cell at various shape can be predicted by using the developed model in this study. It is expected that the experimental results and the simulation model here will contribute to the engineering of the flexible fuel cell as well as further development in the future.

Keywords: Flexible Fuel Cell, Polymer Electrolyte Fuel Cell, Bipolar Plate, Ag Nanowire, Flexible Electronics, Polydimethylsiloxane
Student Number: 2010-23216

Contents

Abstract	i
Contents.....	vi
List of Tables	ix
List of Figures	x
Nomenclature	xv
Chapter 1 Introduction	1
1.1 Motivation.....	1
1.2 Background Studies	11
1.3 Thesis Outlines.....	18
Chapter 2 Fabrication of Flexible PEFC.....	21
2.1 Ag Nanowire Current Collectors	21
2.2 Flexible Flow-Field Plates	25

Chapter 3 Flexible PEFC: Flexibility Test	29
3.1 Bending Test.....	29
3.2 Twisting Test	48
3.3 Mixed Bending and Twisting Test	59
Chapter 4 Flexible PEFC: Direct Compression Test.....	69
4.1 Introduction.....	69
4.2 Experimental	70
4.3 Results and Discussion	74
4.4 Conclusion	86
Chapter 5 Flexible PEFC: Modeling and Validation	87
5.1 Introduction.....	87
5.2 Model and Simulation.....	87
5.3 Validation	94
5.4 Conclusion	105
Chapter 6 Conclusion and Future Work.....	106
6.1 Conclusion	106
6.2 Future Work	111

Bibliography.....	112
국문초록	124

List of Tables

Table 1.1.1 Classification and characteristics of the fuel cells.

Table 4.1 The numbers marked in Figs. 4.2 and 4.3, and corresponding
assembly pressure onto MEA.

Table 5.1 Parameters and values used in the model of the PEFC.

List of Figures

Fig. 1.1.1 Examples of flexible electronics [4-6].

Fig. 1.1.2 Comparison of the energy densities of a fuel cell and lithium-ion battery with respect to volume and weight.

Fig. 1.1.3 The schematic of representative fuel cell using hydrogen as a fuel.

Fig. 1.1.4 Ragone plot of various power sources such as fuel cells, batteries, and capacitors [13-15].

Fig. 1.1.5 Prototypes of portable fuel cell systems [26].

Fig. 1.2.1 Architectural schematics of various flexible fuel cells reported in the literatures [27-34].

Fig. 1.2.2 Comparisons of (a) absolute powers and (b) powers to respective catalyst loading in the literature [27-34].

Fig. 2.1.1 (a) Schematic of SMG method for Ag nanowires with very high aspect ratio. (b) SAED pattern of Ag nanowires by TEM. (c, d) FE-SEM images of very long Ag nanowires by SMG method and short Ag nanowires, respectively. (e) shows the durability of Ag nanowire current collector by repetitive stretching test.

Fig. 2.2.1 Fabrication process of flexible flow-field plate in this study. (a) Coating step of Ag nanowires on mold. (b) Solidifying step of PDMS and bonding Ag nanowires on it. (c) Peeling off step of solidified PDMS with Ag nanowires. The picture shows the cathode flow-channels.

Fig. 2.2.2 Sequential assembly step of flexible fuel cell.

Fig. 2.2.3 Schematic of assembled flexible fuel cell.

Fig. 3.1.1 The OCVs of the flexible fuel cell (a) before and (b) after supplying H₂ and air, respectively. (c) Pictures of bent flexible fuel cells and corresponding bending radius. (d) I-V and I-power curves of the flexible fuel cell at the bending radius indicated in (c). (e) EIS corresponding to (d) at 0.5 V.

Fig. 3.1.2 (a) Picture of a bent flexible fuel cell. (b) Schematic of the generation of assembly pressure by bending in the flexible fuel cell.

Fig. 3.1.3 Boundary conditions of the flexible fuel cell as it is (a) flat and (b) bent in FEM solid-mechanics model.

Fig. 3.1.4 The results of the internal assembly pressure calculated by FEM. Left and right columns show the picture of the fuel cell and corresponding FEM von Mises stress distribution results, respectively.

Fig. 3.1.5 FEM results of the distribution of assembly pressure as the flexible fuel is (a) flat and (b) bent. (c) shows the stress tensor of the assembly pressure (red and blue arrows mean tensile and compressive stress, respectively). (d) shows the relation between ohmic/charge transfer resistances and curvature of the flexible fuel cell.

Fig. 3.1.6 The digital camera images of (a) symmetric and (b) asymmetric designs of the flexible fuel cells. (c) and (d) are the I-V and I-P curves of the flexible fuel cell indicated in (a) and (b), respectively.

Fig. 3.1.7 (a) Bending durability tests of 120 cycles (Red blue and green arrows

indicate 5, 25, and 110 cycles of repetitive bending, respectively). Impedance spectra of the flexible fuel cell with (b) $R = 17.7$ cm, and (c) $R = 36.3$ cm. FE-SEM images of Ag nanowires current collector coated on PDMS (d) before and (e) after repetitive bending test.

Fig. 3.1.8 Application of the flexible fuel cell. (a) An electric fan does not operate as the fuel cell is flat (b) but it operates as it is bent.

Fig. 3.2.1 Photographs of rotational vises for the twisting test of the flexible fuel cell. Twisting angles were set from (a) 0° to (b) 25° . (c) Flexible fuel cell under the twisting angle of 25° .

Fig. 3.2.2 Current-voltage and current-power density curves of the flexible fuel cell measured at the twisting angles of 0, 5, 10, 15, 20, and 25° . Filled and empty marks represent voltage and power density, respectively.

Fig. 3.2.3 The electrochemical impedance spectra of the flexible fuel cell at 0.5 V vs. RHE in Fig. 3.2.2, measured at the twisting angles of 0, 5, 10, 15, 20, and 25° .

Fig. 3.2.4 Finite element analysis of the generated von Mises stress by twisting in the flexible fuel cell. (a) Side view of 3-dimensional model of flexible fuel cell and (b) top view of center slice of the model.

Fig. 3.3.1 The picture of the flexible fuel cell under mixed bending and twisting load.

Fig. 3.3.2 I-V and I-P curves of the flexible fuel cell. (a) and (b) are the cases of the flexible fuel cell with flat and bent ($R = 36.3$ cm) shapes, respectively. The performances were measured with respect to the

simultaneous twisting angles of 0, 5, 10, 15, 20, and 25°. (a) is same as the graph in Fig. 3.2.2 but reprinted here for the comparison with (b).

Fig. 3.3.3 Compressive stress distribution of the flexible fuel cell under (a) twisting and (b) mixed twisting and bending loads. (c) Compressive stress onto MEA with respect to the variation of the twisting angle in the cases of (a) and (b).

Fig. 3.3.4 The (a) electrolyte (ohmic) and (b) electrode (charge transfer) resistances with respect to the twisting angle corresponding to Fig. 3.3.2.

Fig. 4.1 (a) Schematic of experimental setup. (b) Picture of the force sensor and the experimental setup corresponding to (a).

Fig. 4.2 (a) I-V curves of the flexible fuel cell under various assembly pressures shown in Table 1. (b) Magnified graph of the dashed box in (a). (c) I-P curves of the flexible fuel cell corresponding to (a). (d) Magnified graph of the dashed box in (c).

Fig. 4.3 (a) EIS corresponding to the current-voltage curves at 0.5 V in Fig. 4.2. (b) Magnified graph of the dashed box in (a).

Fig. 4.4 (a) Quantitative comparison of (a) peak power densities, (b) ohmic and (c) charge transfer resistances at various assembly pressures. All insets are magnified graphs at low assembly pressure onto MEA.

Fig. 4.5 (a) Magnified graph at low assembly pressure onto MEA in Fig. 4.4 (a). (b) Quantitative comparison of power densities at 0.5 V with respect to the assembly pressure. (a) is quite similar to the inset in Fig. 4.5(a) but

shown here again to compare it to (b).

Fig. 4.6 3-dimensional mapping of (a) current-voltage-assembly pressure and (b) $Z'-Z''$ -assembly pressure of the flexible fuel cell.

Fig. 5.1 The variations of an exchange current density and a charge transfer coefficient in the flexible fuel cell with respect to the variation of compressive stress.

Fig. 5.2 Comparison of the simulation and experimental I-V curves of the flexible fuel cell. The experimental data here is same as the I-V curves in Fig. 4.2. The numbers marked in the figure indicate the assembly pressure in Table 4.1.

Fig. 5.3 Comparison of the simulation and experimental I-V curves of the flexible fuel cell in [46]. The numbers (1, 2, 3, 4, 5, and 6) in the figures indicate the bending radius of infinite (flat), 36.3, 25.4, 20.6, 17.7, and 15.6 cm, respectively.

Fig. 5.4 Comparison of the simulation and experimental I-V curves of the flexible fuel cell in [47]. The numbers (1, 2, 3, and 4) in the figures indicate the bending radius of infinite (flat), 20.6, 17.7, and 15.6 cm, respectively.

Fig. 5.5 The calculated charge transfer resistance of the I-V curve of the flexible fuel cell in Fig. 5.2, legend number 11 at 0.5 V.

Fig. 5.6 The variations of charge transfer resistance with respect to (a) charge transfer coefficient and (b) concentration of hydrogen. The corresponding I-V model is from Fig. 5.2, legend number 11.

Fig. 6.1 Comparisons of (a) the power densities divided by their amount of

catalyst and (b) the absolute powers measured from the flexible fuel cells including the research here [27-34,46,47].

Nomenclature

V	Operating voltage of fuel cell [V]
j	Operating current density of fuel cell [A/cm^2]
E_{thermo}	Thermodynamically predicted ideal voltage [V]
η_{act}	Voltage loss by activation [V]
η_{ohm}	Voltage loss by ohmic resistance [V]
η_{conc}	Voltage loss by mass transport (concentration) [V]
(ASR)	Area-specific resistance ($\Omega \cdot cm^2$)
j_{leak}	leakage current density [A/cm^2]
$j_{0,anode}$	Anodic exchange current density [A/cm^2]
$j_{0,cathode}$	Cathodic exchange current density [A/cm^2]
α_{anode}	Anodic transfer coefficient [No unit]
$\alpha_{cathode}$	Cathodic transfer coefficient [No unit]
n	Number of electrons transferred [No unit]
F	Faraday constant [=96485 C/mol]
η_{anode}	Anodic voltage loss by activation [V]
$\eta_{cathode}$	Cathodic voltage loss by activation [V]
R	Ideal gas constant [8.314 J/mol·K]
T	Temperature [K]
σ	Conductivity of electrolyte [S/cm]
$t_{electrolyte}$	Thickness of electrolyte [cm]
λ	Water content in electrolyte [No unit]
H_r	Relative humidity [No unit]

c_{H_2}	Concentration of hydrogen [mol/cm ³]
c_{O_2}	Concentration of oxygen [mol/cm ³]
p	Assembly pressure [kPa]
R_{ct}	Charge transfer resistance [$\Omega \cdot \text{cm}^2$]
c^*	Bulk concentration [mol/cm ³]
c^0	The concentration at the surface of reaction [mol/cm ³]

Chapter 1. Introduction

1.1 Motivation

The so-called ‘flexible electronics’ are recently under active research because this is one of the key issues for the next generation electronics, ‘wearable electronics’ or ‘epidermal electronics’ [1–3]. In the last decades, flexible displays, stretchable circuit, bendable semiconductor and so forth have been developed and their commercialization is ongoing, as shown in Fig. 1.1.1. All these examples have one thing in common: They are all small electronics, thereby focused on portable applications. The development trend of such electronics is to miniaturize to make them portable. Here, the most distinguishable difference between normal and portable electronics is that the portable electronics require portable power sources. In other words, it is also the case in the flexible electronics that portable power sources are essentially required. Accordingly, if it is desired to make one portable device fully bendable and pliable, ‘flexible power sources’ should also be developed.

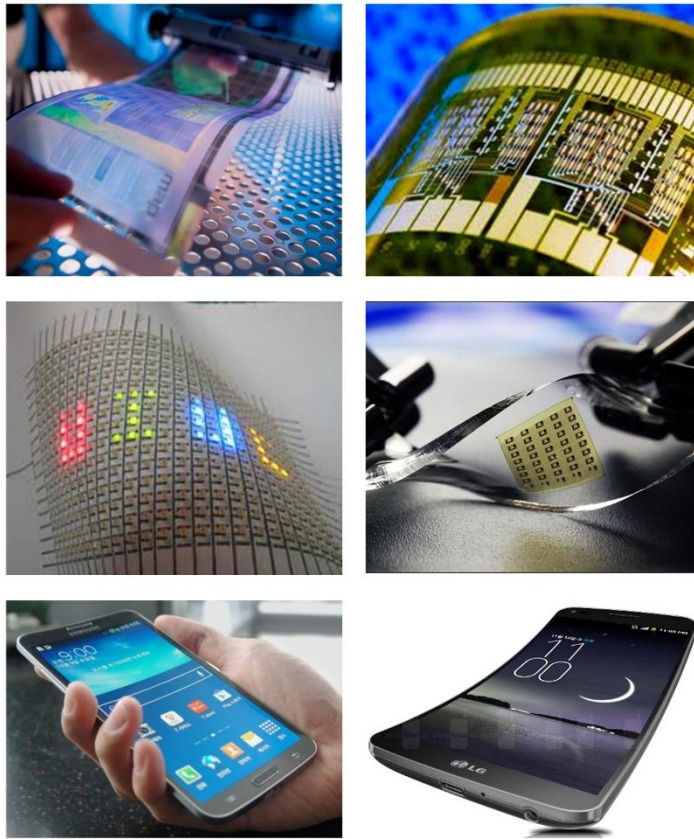


Fig. 1.1.1 Examples of flexible electronics [4–6].

Upto now, lithium-ion batteries have been widely used as a portable power source for most of portable electronics thanks to its highest energy density among other portable power sources. Unfortunately, the lithium-ion battery is confronting its theoretical maximum of energy density while the development of a portable device is incomplete and demands more power for a better performance. One example of this problem in our life is that many of individuals carry external battery recharger or recharging cable wherever they go. Similarly, it may happen again when wearable electronics are commercialized and a lithium-ion battery is used again as a power

source. Although there have been several researches about bendable lithium-ion batteries for the applications of wearable applications [7–9] and it is expected that bendable lithium-ion battery will first open up the commercialization of the wearable electronics, the portable power source with higher energy density should be developed in order to cope with the increasing demand of the power consumption by future electronics.

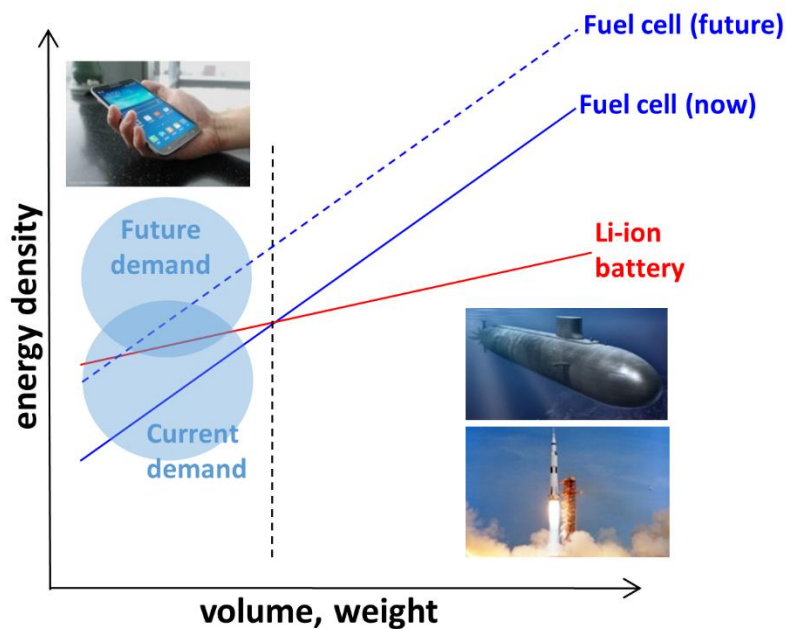
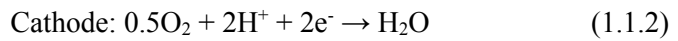


Fig. 1.1.2 Comparison of the energy densities of a fuel cell and lithium-ion battery with respect to volume and weight.

Fuel cell is considered as an alternative power source for current lithium-ion battery because it can potentially have higher energy density than a lithium-ion battery (Fig. 1.1.2). It is an electrochemical device which converts chemical fuel directly to an electricity. It is same as internal combustion engine in that it converts chemical energy to an electricity, while there is the difference that there are three energy conversion steps in internal combustion engines from chemical energy to electrical energy (chemical – thermal – kinetic – electric energy). That is why the energy conversion efficiency of the fuel cell is higher than the efficiency of the combustion engine. Inside the fuel cell, there are three main components composing one unit fuel cell: anode, electrolyte, and cathode. The representative electrochemical in the anode and cathode are as follows:



Between the reactions in the anode and cathode, the electromotive force is generated by the difference of electron affinity. The electron affinities of eqs. (1.1.1) and (1.1.2) induce the powers of oxidation and reduction. It is well established as a standard electrode potential and is tabularized elsewhere [10]. The voltage difference between the eqs. (1.1.1) and (1.1.2) is 1.229 V. The net electrochemical reaction of the fuel cell can be expressed as eq. (1.1.3) from the sum of eqs. (1.1.1) and (1.1.2).



Eq. (1.1.3) is the basic equation of the fuel cell. It means that the fuel cell requires two reactants, *i.e.* hydrogen and oxygen, for its operation and the final byproduct from the operation is only a pure water. For this reason, fuel cells are considered as renewable energy devices. Figure 1.1.3 shows the schematic of the fuel cell using hydrogen as a fuel.

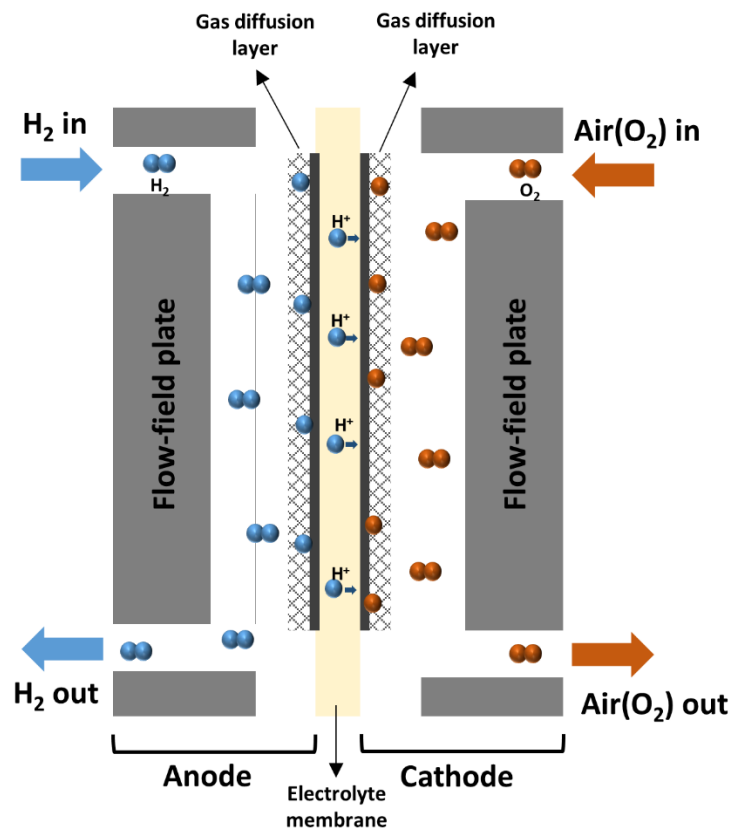


Fig. 1.1.3 The schematic of representative fuel cell using hydrogen as a fuel.

Thanks to the high energy density, fuel cells would be used as power sources in some spaceships and submarines [11,12], because the fuel cell with the size for these applications already has higher density than the battery. According to Fig. 1.1.2, although current technological level of the fuel cell shows superior energy density in large applications such as submarines and spaceships, it is expected that the fuel cell technology will exceed the energy density even in portable scale in the future. Several literature reports that the fuel cells may have an order of magnitude higher energy density than lithium-ion batteries, as shown in Fig. 1.1.4.

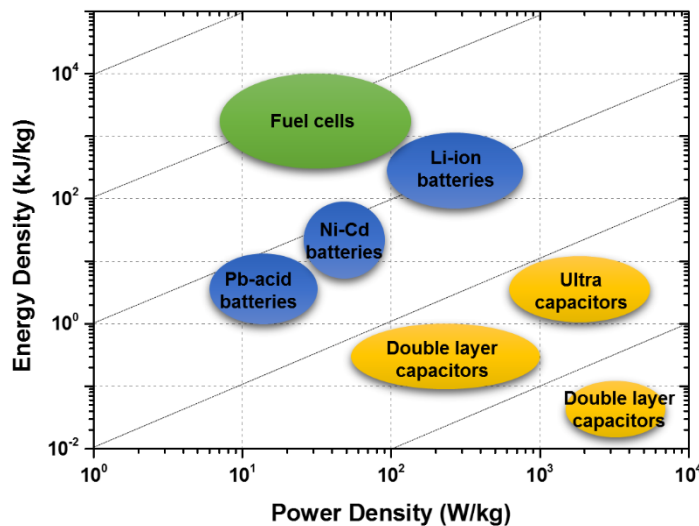


Fig. 1.1.4 Ragone plot of various power sources such as fuel cells, batteries, and capacitors [13–15].

The fuel cells are classified as typical 6 types: PEFC, phosphoric acid fuel cell, alkaline fuel cell, molten carbonate fuel cell, and solid oxide fuel cell [16]. Table 1.1.1 shows the fuel cells with several characteristics. The fuel cell types here are classified by the type of an electrolyte. Among the fuel cells in Table 1.1.1, PEFC has been taken into account as a type for portable applications due to its high power density as well as energy density at low temperature ($< 100\text{ }^{\circ}\text{C}$) and mature technological level among other fuel cell types. Although other fuel cell types may offer other advantages, the operating temperature is the most serious problem in portable applications. The high operating temperature requires an excellent thermal insulation of the system and warm-up time for the start of operation. The thermal insulation can be resolved technologically but warm-up time is crucial in portable applications because the portable electronics are turned on and off frequently. In this case, long warm-up time is not desired. Fortunately, PEFC can be operated even in room temperature, as shown in Table 1.1.1. That is why there have been several efforts to employ the PEFC for portable devices [17–25]. Even there have been other commercialized external fuel cell systems as auxiliary power sources for the portable electronics.

	Polymer Electrolyte Fuel Cell	Phosphoric Acid Fuel Cell	Alkaline Fuel Cell	Molten Carbonate Fuel Cell	Solid Oxide Fuel Cell
Electrolyte	Polymer Membrane	Liquid H ₃ PO ₄ (immobilized)	Liquid KOH (immobilized)	Molten carbonate	Ceramic
Charge Carrier	H ⁺	H ⁺	OH ⁻	CO ₃ ²⁻	O ²⁻
Operating Temperature	25 - 80 °C	200 °C	60 - 220 °C	650 °C	450 - 1000°C
Catalyst	Pt	Pt	Pt	Ni	Ceramic (perovskite)
Cell Components	Carbon based	Carbon based	Carbon based	Stainless based	Ceramic based
Fuel Compatibility	H ₂ , CH ₃ OH	H ₂	H ₂	H ₂ , CH ₄	H ₂ , CH ₄ , CO

Table 1.1.1 Classification and characteristics of the fuel cells.



- Panasonic



- MTI



- Horizon



- Medis Tech.



- Powertrekk



- Lilliputian



- Brunton



- Intelligent Energy

Fig. 1.1.5 Prototypes of portable fuel cell systems [26].

Figure 1.1.5 shows the examples of the prototypes of the portable fuel cells. Considering that wearable electronics or epidermal electronics are the next-generation electronics and power sources for such devices should also be pliable, fully flexible fuel cells can be considered as future portable power sources. In this sense, flexible fuel cells can cope with the needs for its higher energy density as well as environmental flexibility.

1.2 Background Studies

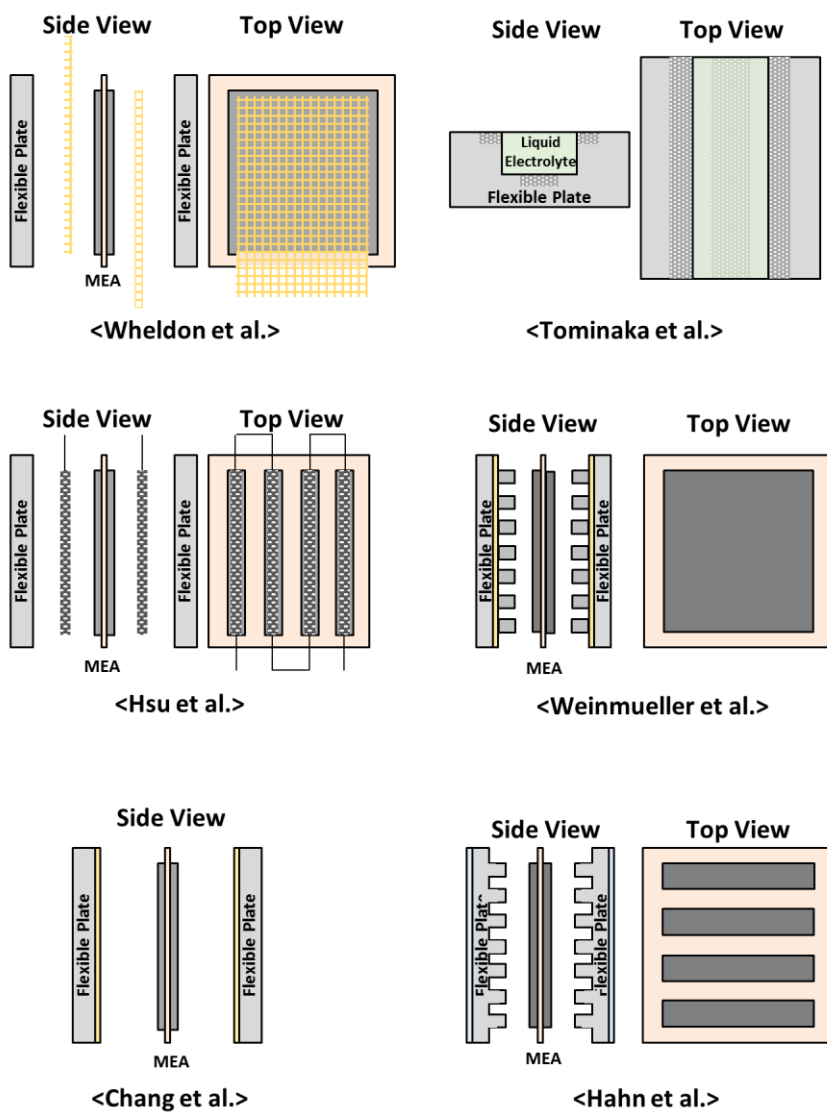


Fig. 1.2.1 Architectural schematics of various flexible fuel cells reported in the literatures [27–34].

There have been seven representative researches about flexible PEFCs in literatures [27–34]. The schematics of the flexible fuel cells are shown in Fig. 1.2.1. Wheldon et al. fabricated a flexible and scalable PEFC with a power density of 57 mW/cm². They used metal mesh (Au coated on Cu) as a current collector and flow-field material as a polyester transparency sheet. Particularly, this study showed that the fuel cell is scalable. But they did not analyze the performance characteristics of their fuel cell at bent or twisted positions [27]. Even the maximal scalable reaction area was 1 cm x 1 cm, which is still not large to be used in real applications.

Tominaka et al. realized a bendable fuel cell by employing a membraneless-type fuel cell design [28,29]. The membraneless-type fuel cell has one advantage: the flexibility and bendability can be maximized thanks to no limitation of materials. However, the special ion-conducting solution is needed and the performance of the fuel cell is generally very low. The fuel cell in this study was fabricated based on cycloolefin polymer. The total size of the system was in micro-scale so that the power density was too low (83 μW/cm²) to be used in real applications.

Weinmueller et al. developed a flexible direct methanol fuel cell with a power density of 19 mW/cm². They successfully employed lithography and patterning techniques to fabricate flow-channels and flow-field plates. But the researcher only examined the performance characteristics at one specific S-shaped bent configuration defined by a specially designed test mold (In flexible polymer electrolyte fuel cells (PEFCs), the assembly type and resulting pressure onto an electrochemical reaction site are the most important issue, which are discussed later in this thesis) [31].

The bendable fuel cell recently disclosed by Hsu et al. has attained the highest

performance to-date (around 220 mW/cm², exact value not specified) [30]. The high performance may be due in part to high Pt/C catalyst loading used in this fuel cell (5 mg Pt/cm² vs. the typical 0.2 – 0.5 mg Pt/cm²). In addition, the design is likely limited to small fuel cell areas as thick carbon lump electrodes are used as current collectors with individual parallel connections between each small fuel cell unit in order to achieve high bendability. Even all these previous researches have one limitation in common that the reactive areas are too small to be commercialized (≤ 1 cm²).

There has been also an effort to enlarge the reactive area in flexible fuel cells. Chang et al. fabricated the flexible fuel cell based on polydimethylsiloxane (PDMS) as a flow-field plate. In order to make the flow-field plate electrically conductible, Cu and Au were coated on the surface of PDMS [32]. The reactive area was 3 x 3 cm², higher than the above references, but there was a severe performance as it was bent. The problem was actually inside the thin metal film current collector since it was vulnerable to even little strain. Hahn et al. also developed a flexible air-breathing PEFC with the power density of 120 mW/cm² [33]. This power density seems high but this fuel cell also has smaller reactive area (< 0.5 cm²) and shares same problem with the fuel cell by Hsu et al. that the flexibility was realized by designing each reactive area as a grid. Hollinger et al. realized a flexible direct methanol fuel cell based on polyimide films [34]. Because polyimide is very stable mechanically and chemically, it can be a suitable material for direct methanol fuel cells. Even this research realized extremely thin design of final assembly of the fuel cell, showing its excellent portability. However, still low peak power density (< 11 mW/cm²) is the problem for its commercialization.

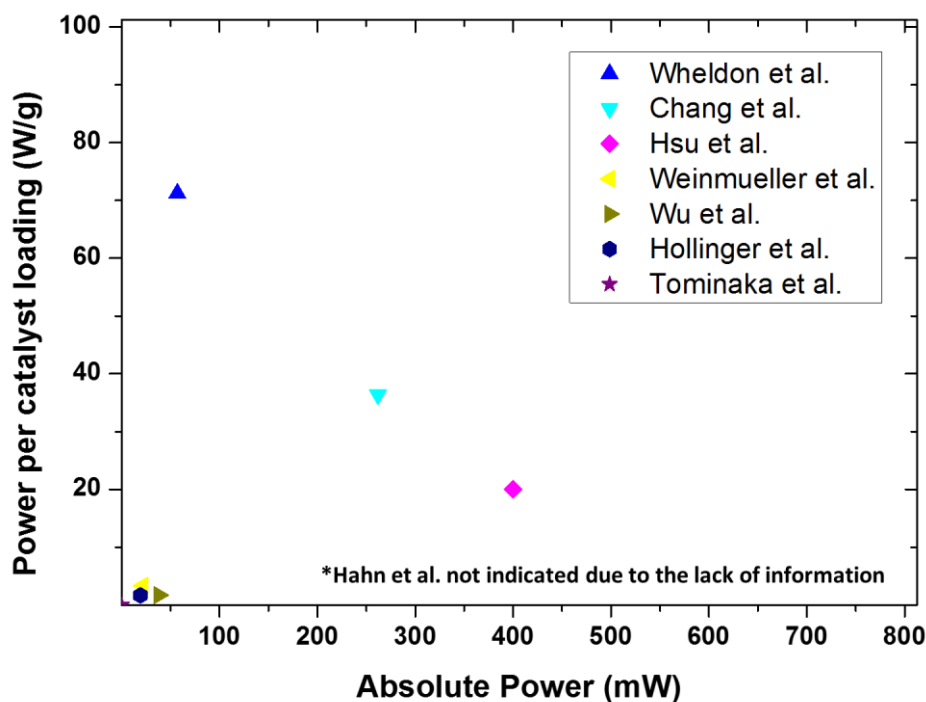


Fig. 1.2.2 Comparisons of (a) absolute powers and (b) powers to respective catalyst loading in the literature [27–34].

The previous researches about flexible PEFCs are compared with each other in Fig. 1.2.2. They are compared based on two parameters: absolute power and power per catalyst loading. The absolute power was calculated by multiplying a peak power density with a total reactive area. The power per catalyst loading was calculated by dividing the peak power density by the Pt/C catalyst loading. Although the peak power density can be another good factor to compare the performances of fuel cells, this study approaches more basically on effectiveness. If only peak power density is considered, the fuel cell by Hsu et al. is the highest. However, the measured the power

per catalyst loading is also important in that this factor is directly related to the commercialization scheme owing to the expensive cost of Pt/C. Meanwhile, the amount of catalyst loading in MEA is crucial for the performance of the fuel cell. From the calculation, the fuel cell by Wheldon et al. showed the highest power per catalyst loading [27]. In the scale of absolute power, the fuel cell by Hsu et al. showed the highest performance in spite of their low power per catalyst loading [32]. Here, another important factor is the absolute power. This factor is also significant in that one of the barriers for the commercialization of the fuel cell is to enlarge its reactive area. When it comes to the size of the fuel cell, several problems are additionally regarded: current collection, durability of MEA, uniform gas distribution to MEA, and so on. In real, it is clearly seen in Fig. 1.2.2 that the power per catalyst loading of the performance champions of the flexible fuel cells decrease with the increasing absolute power. It means that there are really some factors of performance losses as mentioned above.

In order for the flow-field to be used in PEFCs, several material properties should be satisfied. According to Fig. 1.1.3, the flexible fuel cell in this study can be divided into major two parts: flow-field plates and MEA. Here, the MEA is composed of a polymer electrolyte membrane coated with Pt/C layer and additional gas diffusion layer (GDL) at each side. As shown in the name, *i.e.* polymer electrolyte, the electrolyte for a PEFC is generally polymer, thus it is bendable and even foldable. Although carbon papers are mostly used as GDLs in PEFCs, carbon papers are kind of ‘papers’, meaning that it is also bendable. Accordingly, only one component within the PEFC is left to be considered for its bendability and flexibility: flow-field plates.

The flow-field plates are mostly made of a graphite, a metal with high corrosion-resistance, or carbon-based composites [35–43] . These materials have something in common that they are all rigid materials. Accordingly, all-new material for flow-field plates should be developed for the flexible fuel cell. Borup et al. and Mehta et al. proposed numerically the criteria for the qualification of bipolar or monopolar plates in PEFCs as follows [44,45]:

- Electrical conductivity: plate resistance $< 0.01 \Omega \cdot \text{cm}^2$.
- Thermal conductivity: as high as possible.
- Hydrogen/gas permeability: $10^{-4} \text{ cm}^3/\text{s} \cdot \text{cm}^2$.
- Corrosion resistance: corrosion rate $< 0.016 \text{ mA}/\text{cm}^2$.
- Compressive strength: $> 151.7 \text{ kPa}$.
- Density: $< 5 \text{ g}/\text{cm}^3$.

It is noticed that aforementioned PDMS coated with Ag nanowires satisfies 4 of them (electrical conductivity, corrosion resistance, compressive strength, and density). Other unsatisfied requirements, *i.e.* thermal conductivity and gas permeability, actually stem from PDMS, not from Ag nanowires. However, it is thought that thermal conductivity may be the problem when it comes to the PEFC stack. The reason for the high thermal conductivity is the heat generated from the reaction in eqs. (1.1.1) and (1.1.2). The heat dissipation would be disturbed in the fuel cell stack, since the reaction site can be insulated by other bipolar plates. However, it is not the case in this study because this study deals with only unit cell operation. The

gas permeability, especially for hydrogen, is also the limitation of intrinsic property of PDMS. PDMS shows excellent flexibility while its molecular structure is quite close to porous structure. Hydrogen is known as the most ‘easy-penetrating’ gas due to its molecular size. These two factors actually make it not easy to employ PDMS as a material for the flow-field plates in flexible fuel cell. However, the gas permeability is not an intrinsic but an extrinsic material property. by considering this high gas permeability of PDMS, this study designs the Ag nanowire-coated PDMS thicker than what will be permeable to hydrogen.

1.3 Thesis Outlines

As described in Ch. 1.2, the thesis here elaborates upon all the fabrication, characterization, and simulation method of the flexible fuel cell based on PDMS and Ag nanowire current collectors. It comprises total 4 main chapters. Here are the summarizations and contributions on all chapters.

- Chapter 2 elaborates on the fabrication process of the flexible fuel cell based on PDMS flow-field plates coated with Ag nanowires so that all readers can catch up with all the processes. All the flexible fuel cells characterized in this study are based on the same platform as described here and shared in all the chapters. Dr. Ikwhang Chang and I devised the architecture and fabrication process of the flexible fuel cell unit. For the fabrication of the Ag nanowires, Dr. Jinhwan Lee and Mr. Ha Beom Lee partially participated in the fabrication of Ag nanowires.
- Chapter 3 elaborates on the flexibility test of the flexible fuel cell. Because the main issue of flexible electronics is whether it operates as it is bent or twisted, the fuel cell is characterized at various bending shapes (defined by bending radius) and twisting angle, or even both. As the fuel cell is bent or twisted, the performance fluctuates. This phenomenon is elucidated based on the effect of assembly pressure (compressive stress) generated by bending. Or in the case of twisting, it is proposed that the performance loss stems from the permanent

damage of MEA by partially stretched spots by twisting. The pressure is indirectly estimated by using FEM solid-mechanical model and the variation tendency of the performance was hypothesized to be affected by bending and corresponding assembly pressure. Dr. Ikwhang Chang and I devised and prepared the experiment. Bending test was implemented together with Dr. Ikwhang Chang and me. Twisting test and mixed twisting/bending test were devised and conducted by me. I implemented all FEM analyses.

- Chapter 4 describes the effort to investigate the causes of the performance variation with respect to various bending or twisting load. Here, the experiment setup was specially designed to precisely measure the compressive stress onto MEA and all the performances and corresponding electrochemical impedance spectra are related to the compressive stress (Assembly pressure). I devised and implemented the experiment here and Dr. Juhae Jung helped partially to prepare for the MEA and its activation, and discussion. Dr. Ryan O'Hayre provided deep discussion on the analysis of the data.
- Chapter 5 proposes the simulation model of the flexible fuel cell here. Based on the results described in Ch. 4, the variations of all the electrochemical parameters such as a charge transfer coefficient, exchange current density, and ohmic resistance are fitted in accordance with the variation of the assembly pressure. Using the obtained parameters from the experimental data in Ch. 4, one-dimensional model

of the fuel cell is proposed and it is validated by comparing the simulation results with the previous experimental results. I am fully responsible for the work of this chapter.

Dr. Suk Won Cha, Dr. Seung Hwan Ko, and Dr. Sung Jong Yoo supported this work as advisors and project instructors. Although not mentioned above, they have always provided me the deep discussion and direction of the next research on each experiment. Most of the contents here have been already published in scientific journals [46–51]. All the references for them are noted in every chapters.

Chapter 2. Fabrication of Flexible PEFC

2.1 Ag Nanowire Current Collectors

According to the previous studies, the most severe technical barrier for the development of the flexible PEFC is a bendable and stretchable current collector. It is featured that most of flexible materials come from polymer which has little or no electrical conductivity. Recently, though, Lee et al. developed new material satisfying this characteristic. So-called “very long Ag nanowire percolation network” is a current collector and shows the conductivity loss of less than 30 % at a strain of 460 % [52]. As seen in the name, this current collector is based on Ag nanowires. However, unlike other Ag nanowires, the aspect ratio of the nanowire here is higher than previous studies about various metal nanowires [53–57]. This study, however, grew the Ag nanowires by more than 7 repetitive steps so that their average aspect ratio of higher than 10000 (equivalent to the length of 200 μm). In addition, not only single but the network composed of many nanowires was deposited on a surface to constitute one current collector. Each Ag nanowire was connected to each other so that they are all electrically connected. This electric conductor thus shows excellent electrical conductivity as well as the stretchability. Here, the stretchability comes from the narrowed grids, not from the material stretch itself. That is why the flexible fuel cells here were fabricated based on very long Ag nanowires percolation network [52].

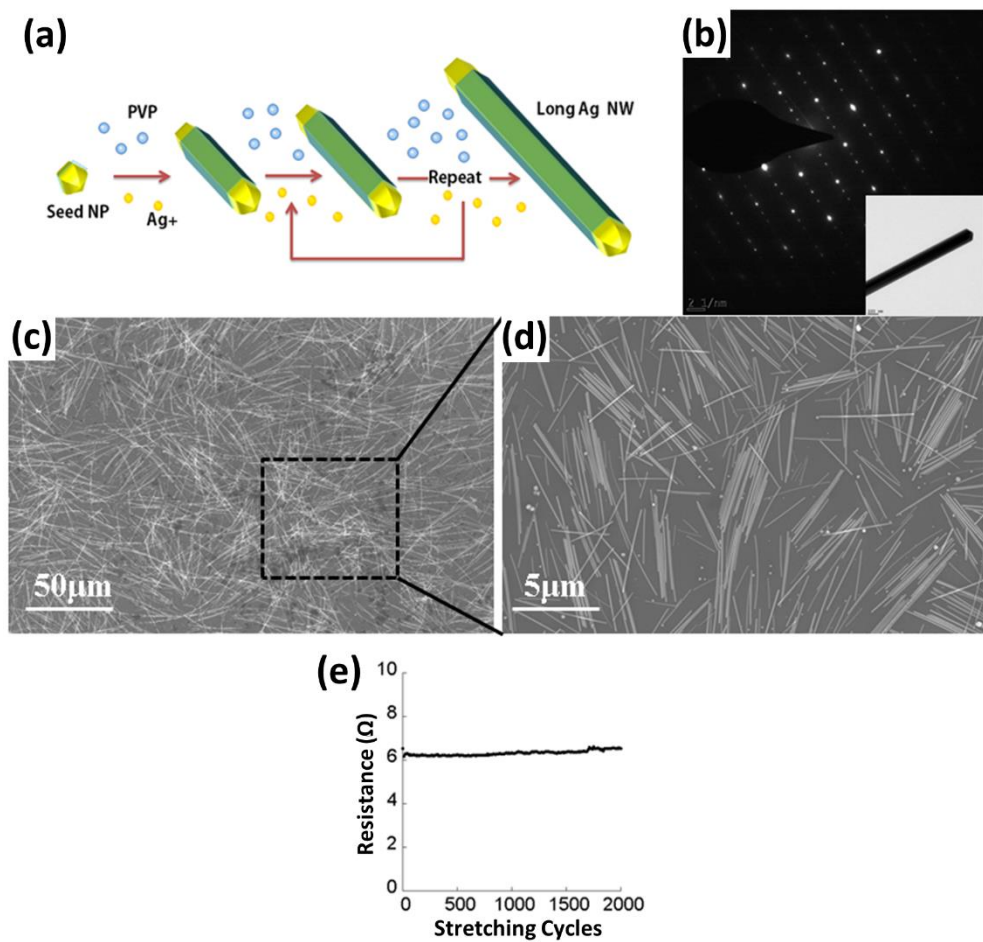


Fig. 2.1.1 (a) Schematic of SMG method for Ag nanowires with very high aspect ratio. (b) SAED pattern of Ag nanowires by TEM. (c, d) FE-SEM images of very long Ag nanowires by SMG method and short Ag nanowires, respectively. (e) shows the durability of Ag nanowire current collector by repetitive stretching test.

Short Ag nanowires with $<15\ \mu\text{m}$ length were fabricated via the conventional polyol synthesis as shown in Fig. 2.1.1(a). The structure of Ag nanowires was investigated using a field emission scanning electron microscope (SEM; SUPRA 55VP, Germany) and transmission electron microscopy (TEM; JEOL-3000F, Japan). A successive multi-step growth (SMG) method was also adopted to enhance the length of the Ag nanowires (Fig. 2.1.1(a)) [52,58,59]. During the SMG of long Ag nanowires, capping agent and additional silver ions were continually injected. To reduce reaction time and increase synthetic yield, Cu additive solution was added to 5 ml of heated ethylene glycol at $151.5\ ^\circ\text{C}$. After 10 minutes, 1.5 ml of 147 mM polyvinylpyrrolidone (PVP) solution and 1.5 ml of 94 mM AgNO_3 solution were added sequentially. Subsequent to the first synthesis, the obtained Ag nanowire was used as seed for further increase and repeated growth steps; PVP and AgNO_3 injection. After several steps, synthesized Ag nanowires were cleaned using acetone and ethanol for several times for the next deposition step on a mold. As shown in the transmission electron microscopy (TEM) analysis (Fig. 2.1.1(b)), Ag nanowires synthesized with the modified growth step method also have a good crystalline structure (inset image shows the characterized Ag nanowire sample). The pattern was obtained at the electron transmission angle vertical to the growth direction $[1\ 1\ 0]$ giving clear diffraction spots and confirmation of its crystallinity. The diffraction pattern shows a series of one strong and two weak spots. It is same as the pattern in Fig. 2D in a previous report by Chen et al. where a pentagonal pillar-like Ag nanowire is well described [60]. We demonstrated that longer Ag nanowires (Fig. 2.1.1(c)) could improve the electrical conductance and

mechanical stability under various mechanical stresses compared to the high-density shorter Ag nanowires (Fig. 2.1.1(d)). As the nanowire density is increased to improve the electrical conductivity, the Ag nanowires percolation behaves like Ag metal films and results in the decrease of its electrical conductance. This problem can be solved by using very long Ag nanowires at low nanowires number density. This is attributed to a higher chance of maintaining the electrical connection through interweaved networks of longer Ag nanowires even under large stress conditions than the shorter Ag nanowires. In detail, the number density of Ag nanowires was optimized to achieve both mechanical stretchability and electrical conductivity. The dispersion state of such percolation networks was explained in our previous research [52]. Figure 2.1.1(e) shows the durability of the Ag nanowire current collector. It was repetitively stretched and released for more than 2000 times and there was no increase of its ohmic resistance.

2.2 Flexible Flow-Field Plates

To fabricate the flexible fuel cell based on PDMS and Ag nanowires network, steel molds for anode and cathode flow-field plates were first fabricated. The molds were fabricated to have the inverse patterns of the flow channels corresponding to the anode and cathode, respectively. The cross sectional dimensions of the flow channels were 1 mm x 1 mm (anode) and 2 mm x 1 mm (cathode), respectively. Rib widths of 1 mm were used in both cases. Total reactive area of each flow channel pattern was 3 cm x 3 cm (total 9 cm²). A total plate area of the flow-field plate including sealing area was 6 cm x 6 cm.

The Ag nanowire percolation network was coated on PDMS to compose the flow-field plates of the flexible fuel cell. Cleaned Ag nanowires were dispersed in isopropyl alcohol (IPA) with 0.006 mg/ml concentration. The mixed solution was deposited onto the mold to make the bendable electrode for the fuel cell. After the IPA was dried, deposited Ag nanowires and mold were annealed at 120 °C to decrease the resistance by improving the connection between the Ag nanowires (Fig. 2.2.1 (a)). After one hour, Ag nanowire film was additionally cured at 60 °C for 2 hours. After that, to create the flexible flow-field plates, a PDMS solution and curing agent were poured onto the Ag-nanowire-coated molds (Fig. 2.2.1 (b)). The weight ratio of the PDMS solution and the curing agent was 10:1. The filled molds were heated at 70 °C for 4 hours to solidify the PDMS. The Ag nanowires bond more strongly to the solidified PDMS than to the molds; thus, when the flexible PDMS flow-field plates are removed from the molds, they retain the strongly-bonded, conductive Ag-

nanowire coating on their surface (Fig. 2.2.1(c)).

The measured electrical resistance of the Ag nanowire layer on the PDMS pad was $6.9\ \Omega$, indicating that the in-plane electrical conductivity of the Ag nanowires on PDMS is one order of magnitude higher than that of a gas diffusion layer (electrical conductivity of GDL = 100–300 S/m) [61]. Therefore, most of the electronic current will flow dominantly through the Ag nanowire percolation network layer and this is why the highly conductive layer (Ag nanowires) is employed although the GDL is electrically conductive. These PDMS flow-field plates meet both requirements of electrical conductivity and mechanical stability.

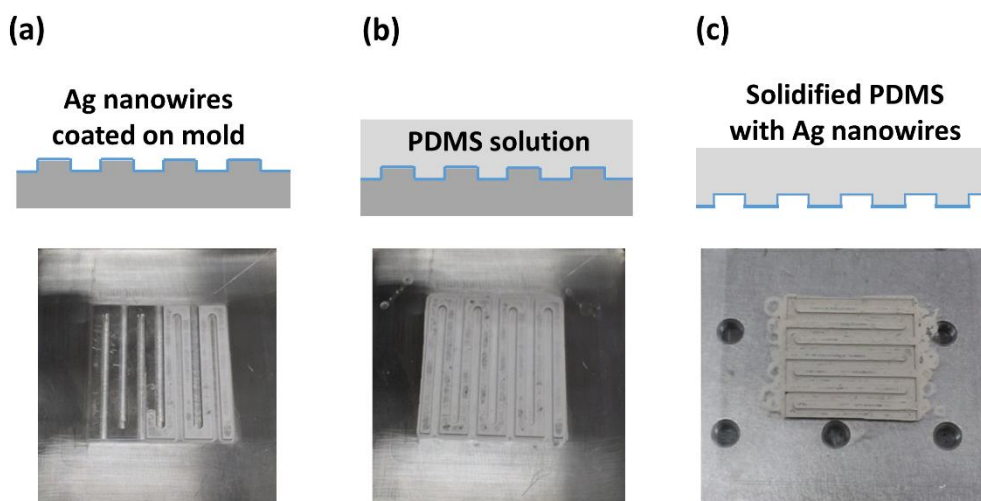


Fig. 2.2.1 Fabrication process of flexible flow-field plate in this study. (a) Coating step of Ag nanowires on mold. (b) Solidifying step of PDMS and bonding Ag nanowires on it. (c) Peeling off step of solidified PDMS with Ag nanowires. The picture shows the cathode flow-channels.

A 3 cm x 3 cm commercial MEA (Fuel Cell Power Co., Republic of Korea) was used in this study. The commercial MEA was based on a 50 μm thick Nafion[®] 212 membrane, anode and cathode Pt/C catalyst loadings of 0.45 mg/cm^2 , and 350 μm thick carbon-paper GDLs. The MEA was sealed between the anode and cathode monopolar plates using a silicone sealant paste (SR500, Daeheung Chemical Co., Republic of Korea) (Fig. 2.2.2).

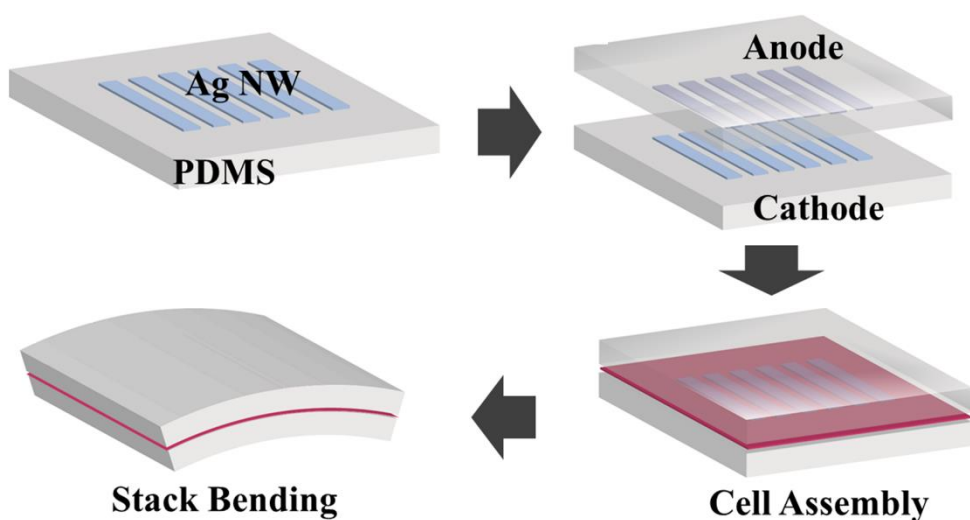


Fig. 2.2.2 Sequential assembly step of flexible fuel cell.

The Ag nanowires network layers were connected to external electric wires to measure the electrochemical performance. The electric wires were contacted to the Ag nanowire current collector and fixed by the clamping force induced by the sealant paste. The connected wires came out directly through the sealant paste. Fig. 2.2.3 shows the schematic of the finalized assembly of the as-fabricated flexible fuel cell.

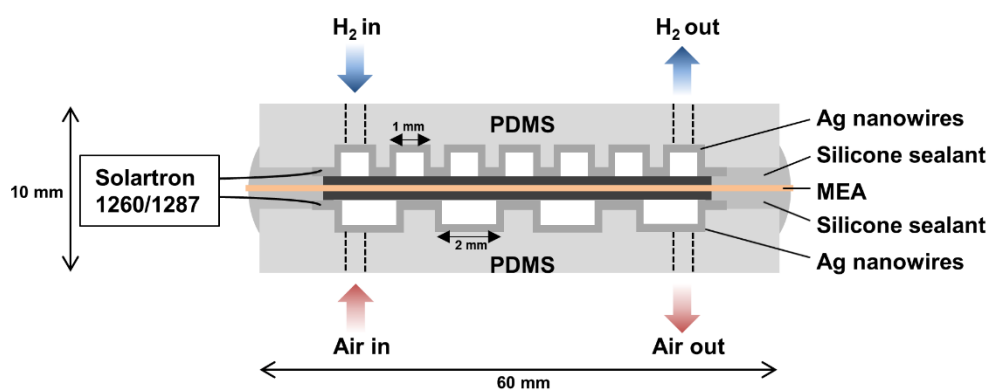


Fig. 2.2.3 Schematic of assembled flexible fuel cell.

Chapter 3. Flexible PEFC: Flexibility Test

3.1 Bending Test

3.1.1 Introduction

The flexible fuel cell described in Ch. 2 was tested. If one flexible electronics is developed, it should be tested whether it is able to operate without critical performance loss as its shape is changed. This flexibility test is generally implemented by bending the flexible electronics. Accordingly, the flexible fuel cell here was characterized by gradually bending it.

3.1.2 Experimental

The as-fabricated flexible fuel cell was tested in this study. The thickness of the flow-field plate here was 6 mm for the first bending test. The other flow-field plates with the thicknesses of 4 mm and 6 mm were also fabricated to prove the performance enhancement by the increased compressive stress induced from the asymmetric design [47]. To supply fuel gases, a flexible silicon tube was inset each side. The flow rates of H₂ and air were 500 cm³/min and 1000 cm³/min, respectively. The I–V and electrochemical impedance spectroscopy (EIS) were measured utilizing Solartron 1287/1260 (Solartron Analytical Co., United Kingdom). The I–V was measured by

using galvanodynamic mode with a scanning rate of 30 mV/s. EIS measurements were performed with 30 mV of AC perturbation under a constant bias of 0.5 V and in the frequency range of 10^5 –2 Hz. Humidified H₂ and air at 25 °C were supplied to the anode and the cathode, respectively. Experimental sequences were (i) supply fuel gases, (ii) OCV measurement for steady state condition, (iii) galvanostatic measurement at 0.5 V for an hour each for membrane and catalyst layer humidification, (iv) repeating I–V and EIS measurements. The measurement mode was a potentiostat at 0.5 V in the activation process of MEAs. The performances at the bending radius of 36.3, 25.4, 20.6, 17.7, 15.6 cm, and flat shape were measured in the flexible fuel cell of symmetric design. In the fuel cell of asymmetric design, the performances were measured at the bending radius of 36.3, 17.7, 15.6 cm and flat shape.

3.1.3 Results and Discussion

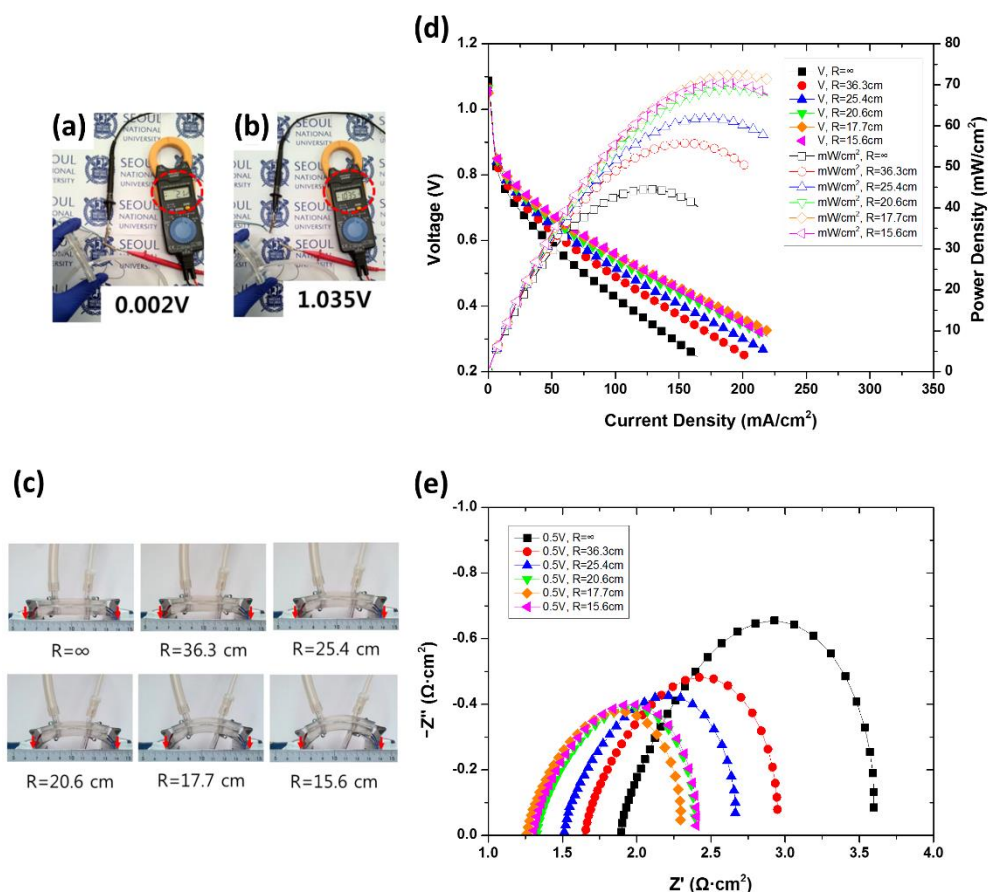


Fig. 3.1.1 The OCVs of the flexible fuel cell (a) before and (b) after supplying H₂ and air, respectively. (c) Pictures of bent flexible fuel cells and corresponding bending radius. (d) I-V and I-power curves of the flexible fuel cell at the bending radius indicated in (c). (e) EIS corresponding to (d) at 0.5 V.

Open circuit voltages (OCV) were measured when no fuel was fed and 500 cm³/min of hydrogen was fed to the flexible fuel cell. The resulting OCVs were 0.021 V (no fuel) and 1.035V (with H₂), respectively, as shown in Figs. 3.3.3 (a) and (b). As the

fuel cell was bent, the bending radius was measured by the horizontal distance between the two edges of the fuel cell as shown in Fig. 3.1.1 (c). As shown in Fig. 4(d), the power density with the maximum bending (the bottom-right image in Fig. 3.1.1 (c)) was 71 mW/cm^2 whereas the flat cell without bending (the top-left image in Fig. 3.1.1(c)) was 41 mW/cm^2 . The performance of highly bent fuel cell is increased by 73 % compared to that of original flat condition. It is thought that such performance enhancement is attributed to the increased compressive force between the two PDMS flow-field plates by bending, and resulting decreased ohmic and charge transfer resistances. Firstly, as shown in Fig. 3.1.1 (e), the charge transfer resistance decreases consistently and somewhat exponentially from the flat ($R = \infty$) to the highly bent condition ($R = 15.6 \text{ cm}$). The performance difference is also partly ascribed to the easier water removal in the catalyst layer (CL) and GDL. The cathode side is at the bottom side while the anode is on the top in this experiment. Water formed in the CL and GDL grows into larger droplets, which eventually will fall (*i.e.* will be detached from the cathode). The decreased width and depth of flow channel in the bent condition may facilitate this process. It is reported that the flow channels with smaller dimension can prevent the severe water flooding at the cathode, and then the decreased flow channels in bent conditions can enhance mass transport (or decreased flooding) because of a reduced dead zone and an increased air speed [62]. As shown in Fig. 3.1.1 (e), it is seen that the ohmic loss decreases from $1.89 \text{ } \Omega \cdot \text{cm}^2$ to $1.26 \text{ } \Omega \cdot \text{cm}^2$. We need to postulate two possible reasons: the decreased resistance between Ag nanowire layer and GDL, and the decreased resistance of MEA itself. The contact resistance between the Ag nanowires and GDL was high in a flat

condition. When the fuel cell assembly was bent from flat to the bending radius of 15.6 cm, the overall ohmic resistance decreases from $1.89 \Omega \cdot \text{cm}^2$ to $1.26 \Omega \cdot \text{cm}^2$ and power density sharply increased by 70 %. As another factor, PDMS pads pressurize the MEA, resulting in the decrease of the ohmic loss. Asghari et al. and Lee et al. investigated such behaviors of ohmic resistances, in which they reported the ohmic resistance of an MEA decreases as clamping pressure increases [63,64]. As the high clamping force pressurizes the MEA, the effect of mass transport loss generally could increase remarkably due to the decreased porosity of GDL. However, from the I-V and EIS results, it can be inferred that the normal force only played a role in decreasing the ohmic loss, not in reducing the porosity of GDL and regarding mass transport. This phenomenon is valid only up to the bending radius of 17.7 cm; the ohmic resistance increases slightly from $R = 17.7 \text{ cm}$ to $R = 15.6 \text{ cm}$. It is supposed that the decreased ohmic resistance in highly bent condition is due to the damaged GDL by bending. Although GDLs are kind of paper, many cracks are generated by bending. Such cracks could increase the ohmic resistance. Similar phenomenon was observed elsewhere [32]. Interestingly, the variation tendency can be observed in not only the ohmic but also the charge transfer resistances. As mentioned above, the decrease of the charge transfer resistance was induced by the enhanced diffusion from the accelerated speed of H_2 and air by narrowed cross-sectional area of flow channels. In addition, if the gap between a GDL and a rib is pressed optimally, flow channels can distribute the reactants to edge region effectively. It may lead to the decrease of the charge transfer resistance. It is thought that there is not significant loss of pores and resulting mass transport loss in GDLs up to the bending radius of 17.7 cm.

However, the pores might be decreased by the highly generated compressive stress from bending [65]. The increase of the charge transfer resistance in that region is attributed to this clogged pores in GDL and resulting mass transport loss.

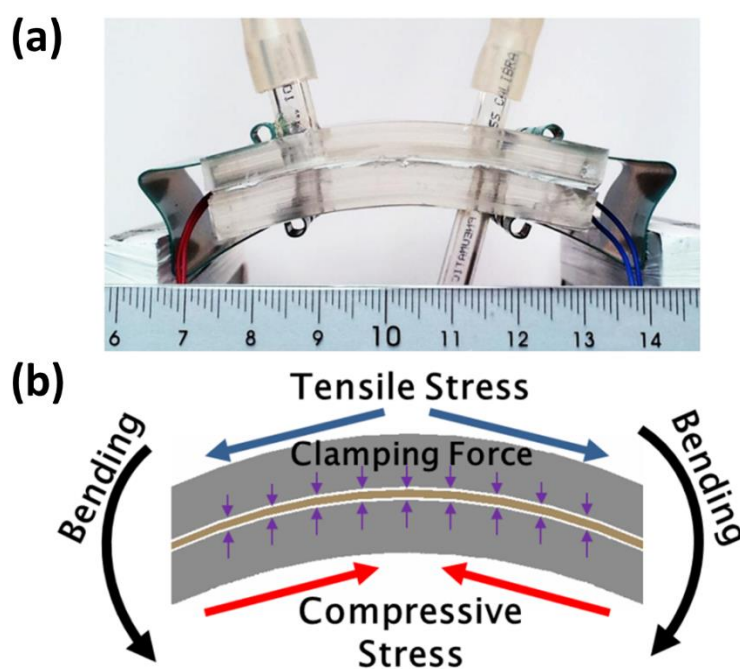


Fig. 3.1.2 (a) Picture of a bent flexible fuel cell. (b) Schematic of the generation of assembly pressure by bending in the flexible fuel cell.

Bending which is the key factor for the variation of the performance as indicated in Fig. 3.1.1. It influences the internal stress in PDMS flow-field plates and MEA as described in Fig. 3.1.1. In order to investigate the stress within the flexible fuel cell, the bending of the flow-field plates was simulated using finite element method (FEM) where Mooney-Rivlin model was adopted [66–68]. When the flexible fuel cell is subject to compression by the method indicated in Fig. 3.1.2 (a), bending moment is generated because the lower part of the flexible fuel cell is compressed while the upper part is stretched, as indicated in Fig. 3.1.2 (b). In such case, the flexible fuel cell is bent upward, and this changes the direction of the compressive and tensile stresses which are initially laid horizontal to the curved direction, as described by the blue and red arrows. The turned directions of the tensile and compressive stresses accordingly generate compressive clamping force vertical to the center layer where the MEA is located.

In order to verify this concept, FEM was used to investigate the stress distribution inside the flexible fuel cell. Comprehensive simulations were processed using COMSOL Multiphysics 4.2. Because the PDMS used in the experiment is an extremely elastic material, the Mooney-Rivlin (MR) model was applied, as it has been used in many studies to calculate the internal stress inside the PDMS [66–68]. The governing equations of this model are as follows:

$$\begin{aligned}
-\nabla \cdot \boldsymbol{\sigma} &= \mathbf{F}\mathbf{v}, \boldsymbol{\sigma} = (\mathbf{S} \cdot (\mathbf{I} + \nabla \mathbf{u})) \\
\mathbf{S} &= \frac{\partial \mathbf{W}_s}{\partial \boldsymbol{\varepsilon}} \\
\mathbf{W}_s &= \mathbf{C}_{10}(\bar{\mathbf{I}}_1 - 3) + \mathbf{C}_{01}(\bar{\mathbf{I}}_2 - 3) + \frac{1}{2} \kappa (\mathbf{J}_{\text{el}} - 1)^2 \\
\boldsymbol{\varepsilon} &= \frac{1}{2} [(\nabla \mathbf{u})^T + \nabla \mathbf{u} + (\nabla \mathbf{u})^T \nabla \mathbf{u}]
\end{aligned} \tag{3.1.1}$$

Here, $\boldsymbol{\sigma}$, \mathbf{W}_s , κ , \mathbf{C}_{10} , \mathbf{C}_{01} , $\bar{\mathbf{I}}_1$, $\bar{\mathbf{I}}_2$, and \mathbf{u} denote the Cauchy stress, the strain energy density, the bulk modulus, the first MR constant, the second MR constant, the first invariant of the uni-modular component, the second invariant of the uni-modular component, and the deformation, respectively. The material properties of the PDMS used in this study were as follows: density = 965 kg/m³, bulk modulus = 600 kPa, Poisson's ratio = 0.499, \mathbf{C}_{01} = 254 kPa, and \mathbf{C}_{10} = 146 kPa [66,69]. The Poisson's ratio was set to 0.499 rather than 0.5 to avoid divergence of the calculation [68].

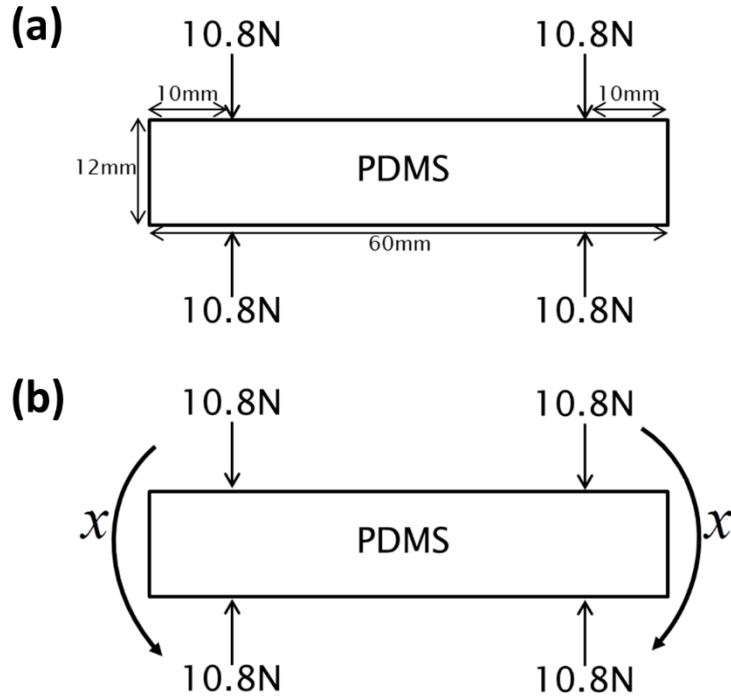


Fig. 3.1.3 Boundary conditions of the flexible fuel cell as it is (a) flat and (b) bent in FEM solid-mechanics model.

The boundary conditions are indicated in Fig. 3.1.3. The vertically compressing force, 10.8 N, is the clamping forces by the clip, which were measured experimentally. As shown in Fig. 3.1.3 (a), clamped spots were located 10 mm apart from each edge. The dimensions of the width and height were 60 mm and 12 mm. In this case, although the total thickness of the flexible fuel cell included the MEA, it was ignored because the thickness of the MEA is comparatively thinner than 12 mm. The bending moment was therefore set as a parameter to control the deformation of the flexible fuel cell, as shown in Fig. 3.1.3 (b).

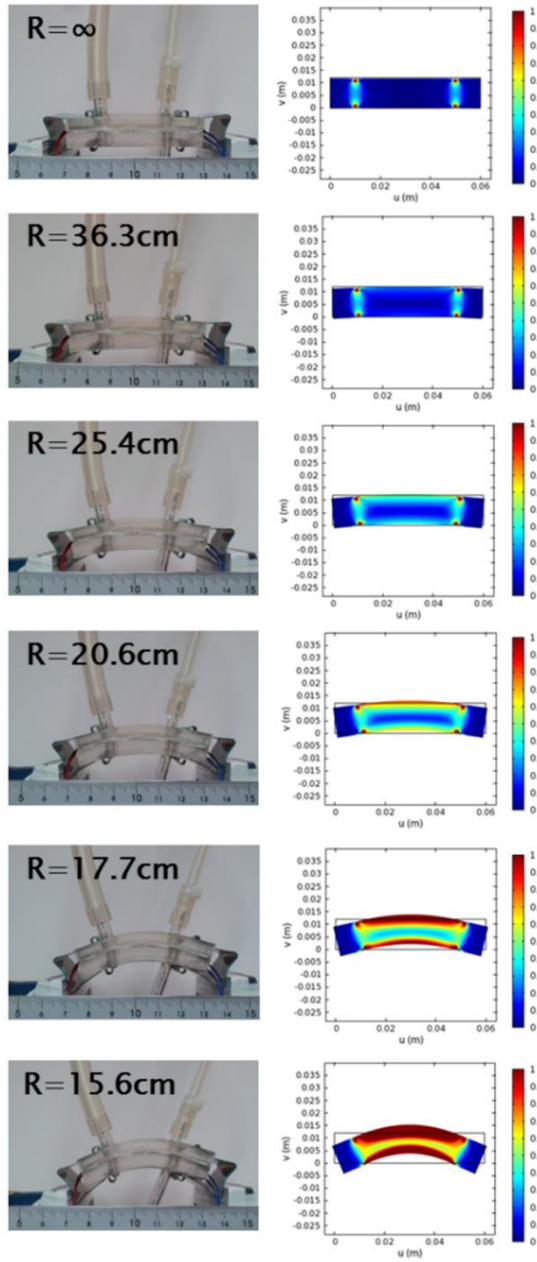


Fig. 3.1.4 The results of the internal assembly pressure calculated by FEM. Left and right columns show the picture of the fuel cell and corresponding FEM von Mises stress distribution results, respectively.

Fig. 3.1.4 shows the results of the stress analysis and digital camera images of the flexible fuel cell. As expected, the internal stresses generated by bending propagates as the bending increases. The representative simulation results are indicated in Fig. 3.1.5. Fig. 3.1.5 (a) and (b) are the cases of the first and last row of Fig. 3.1.4. In Fig. 3.1.5 (a), it was apparently visualized that only the spots contacting the clamps are subject to stress. Even if this state is distorted more by bending, the stress concentration at the clamping spots are still shows higher compressive stress, as shown in Fig. 3.1.5 (b). Particularly, Fig. 3.1.5 (c) shows the directions of the principal stresses; the internal compressive stresses vertical to the MEA are clearly visualized. The calculated forces are given in Fig. 3.1.5 (d) where it is evident that the ohmic/charge transfer resistances and the average normal forces are negatively correlated.

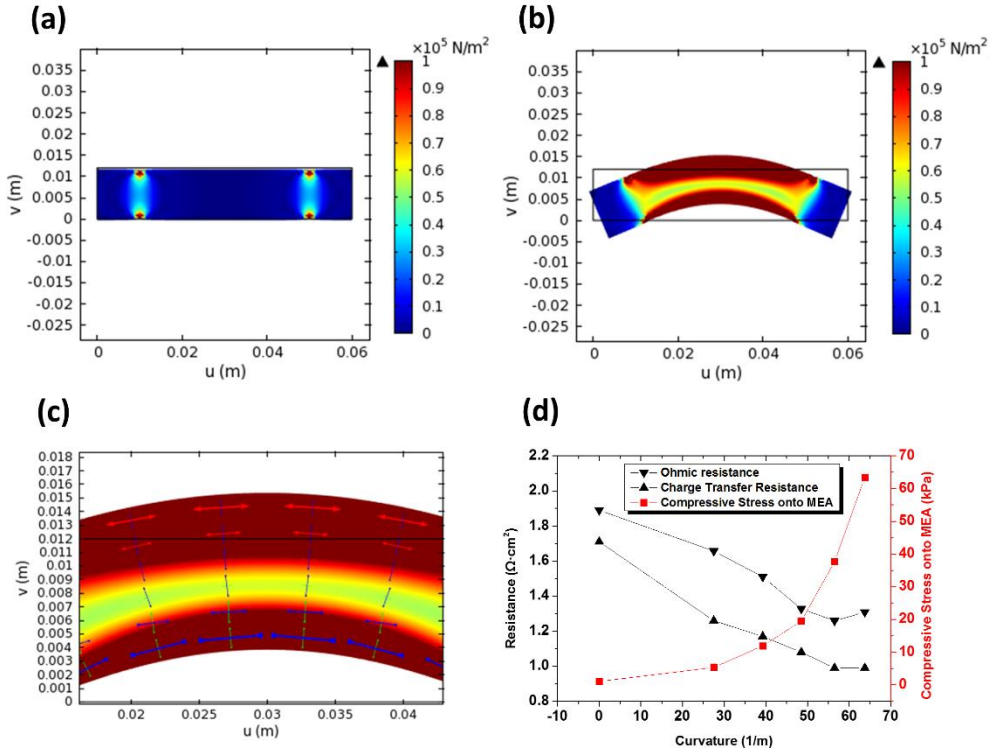


Fig. 3.1.5 FEM results of the distribution of assembly pressure as the flexible fuel is (a) flat and (b) bent. (c) shows the stress tensor of the assembly pressure (red and blue arrows mean tensile and compressive stress, respectively). (d) shows the relation between ohmic/charge transfer resistances and curvature of the flexible fuel cell.

In addition, as indicated in Fig. 3.1.5 (a), the stress was concentrated on the spot where the cell was clipped for the flat condition. However, Fig. 3.1.5 (b) shows that rather the larger stress was expanded into the center part of the fuel cell where the MEA was located under a bending condition. The compressive stress occurs at the concave side of the cell and the tensile stresses at the convex side in Fig. 3.1.5 (c). In this situation, the vertical component of the stress in the convex side is in the

downward direction, while that of the compressive stress at the concave side is in the upward direction, generating effective compressive stress in the direction normal to the MEA plane. This result corresponds to the schematic shown in Fig. 3.1.5 (c). Fig. 3.1.5 (d) indicates the calculated average normal force to the MEA with the size of $3\text{ cm} \times 3\text{ cm}$, and measured ohmic and charge transfer resistances with respect to various curvatures of the flexible fuel cell. The average normal force increases exponentially with the increasing curvature. Interestingly, the ohmic and charge transfer resistances show a similar trend with the force; they both showed decreasing tendency up to the curvature of 60 /m . The vertical compressive stress onto the MEA is considered as the main reason for decreasing the ohmic resistance, enhancing the performance of the flexible fuel cell. This is further supported by a report showing that the contact resistance between MEA and Ag nanowires decreases with the increase of the pressure applied on it [64]. As mentioned above, the tendency of the decreasing resistance in higher curvature range is valid only up to a specific curvature ($\sim 60\text{ /m}$). It is further attributed to the fact that the ohmic resistance consists of not only contact but ion-conducting resistance. From the specific curvature, the ohmic resistance seems to be dominated by the contact resistance; that is, the ion-conducting resistance becomes negligible compared to the contact resistance in MEA [63,64]. As the curvature of the bent fuel cell increases, a cross-sectional area of flow channel decreases by generated compressive stress. Because the flow rates of hydrogen and air in the experiment were fixed to 500 and $1000\text{ cm}^3\text{/min}$, respectively, the flow speeds of hydrogen and air increases as the cross-sectional area of flow channels decreases. As a result, it induces enhanced diffusion into GDL, decreasing charge

transfer resistance in the flexible fuel cell [62]. The simulation results are coincident with the results mentioned at the previous discussions on Fig. 3.1.1 (d).

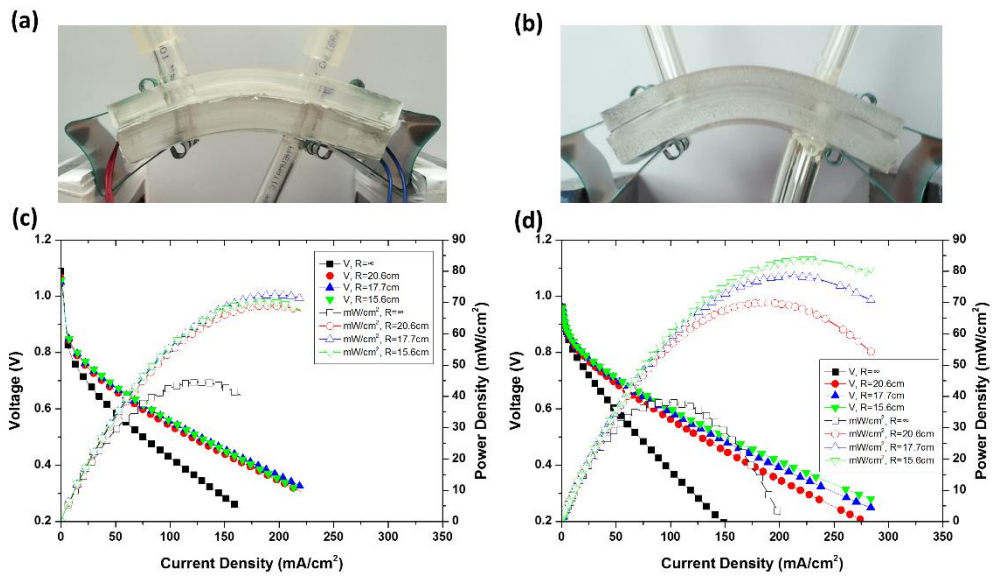


Fig. 3.1.6 The digital camera images of (a) symmetric and (b) asymmetric designs of the flexible fuel cells. (c) and (d) are the I-V and I-P curves of the flexible fuel cell indicated in (a) and (b), respectively.

Here, if the generated compressive stress by bending is the main factor of increasing the performance, it can be supposed that the location of the MEA near the surface of the fuel cell, *i.e.* the site where there is higher compressive stress than center line, will bear higher performance than the performance indicated in Fig. 3.1.1. In real, as shown in Fig. 3.1.6, the flexible fuel cell of asymmetric design shows higher peak power density (82 mW/cm^2) than that of original design (71 mW/cm^2 , Fig. 3.3.6(c)) as the fuel cell is bent with the bending radius of 15.6 cm (Fig. 3.1.6 (d)). The lower performance in the fuel cell with $> R = 15.6 \text{ cm}$ is attributed to the total thickness thinner in the asymmetric design (12 mm vs. 10 mm). It was revealed through FEM simulation that thinner thickness with same material bears higher compressive stress by bending [47].

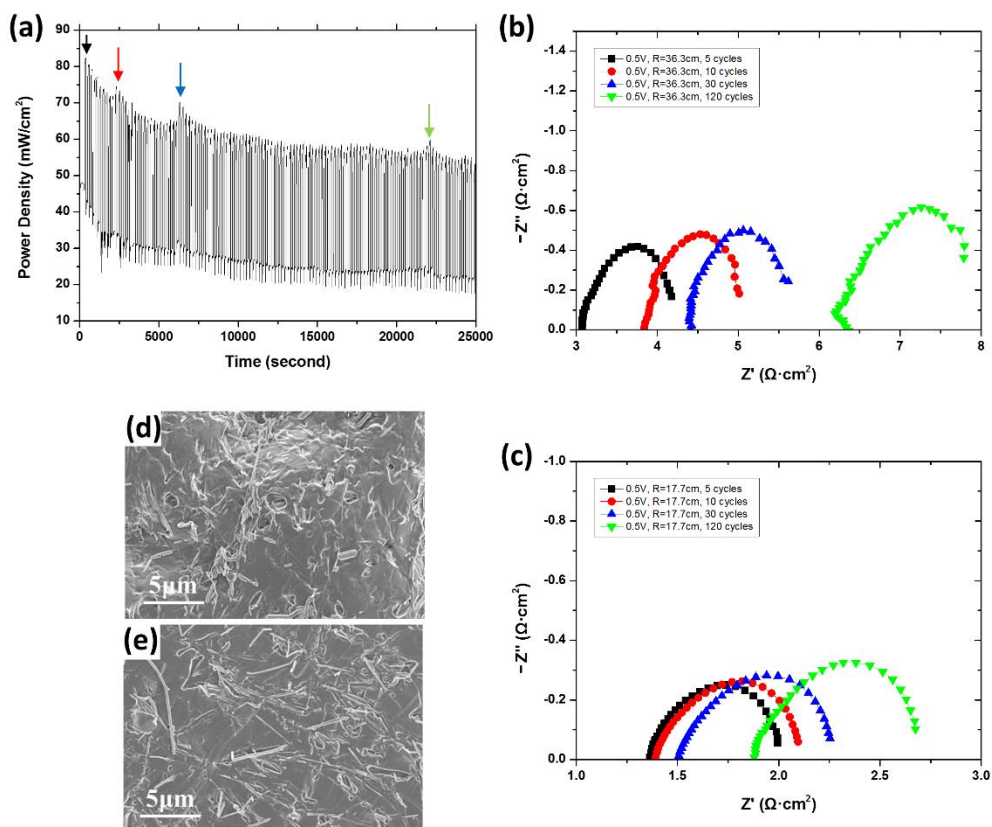


Fig. 3.1.7 (a) Bending durability tests of 120 cycles (Red blue and green arrows indicate 5, 25, and 110 cycles of repetitive bending, respectively). Impedance spectra of the flexible fuel cell with (b) $R = 17.7$ cm, and (c) $R = 36.3$ cm. FE-SEM images of Ag nanowires current collector coated on PDMS (d) before and (e) after repetitive bending test.

A set of durability tests of the flexible fuel cell was also carried out as shown in Figure 3.1.7. The power densities in Fig. 3.1.7 (a) are the power densities at 0.5 V with $R=17.7$ cm. The impedance spectra were measured at a fixed dc bias of 0.5 V vs. RHE. Fig. 3.1.7 (a) shows that the power density sharply decreases by 0.5 mW/cm^2 per cycle from 0 cycle to 25 cycles and by 0.1 mW/cm^2 per cycles after 25 cycle. The vertical arrows in Fig. 3.1.7 (a) shows the cycles where impedance measurements were performed. The temporary increase of the measured power densities at the points indicated by arrows are attributed to the disturbance caused by the impedance measurements. Figures 3.1.7 (b) and (c) show impedance spectra measured at the bending radii of 36.3 cm and 17.7 cm (Figure 3.1.1 (c)), respectively. These spectra suggest that the ohmic loss increases as the fuel cell undergoes the bending fatigue. However, the structures and morphologies of the Ag nanowires have not been changed significantly as shown in Fig. 3.1.7 (d) (as-prepared) and (e) (after 110 cycles). It corresponds with the result in Fig. 2.1.1 (e) that the electrical resistance of the long Ag nanowire cluster kept almost its initial value even after 2,000 cycles of bending; this result shows its initial and final resistances. Further, even when the Ag nanowire/PDMS structure was mechanically extended by 157 %, it maintained its good electrical conductivity. These results show that the electrical resistance of fabricated Ag nanowire percolation network electrode can be retained successfully under various mechanical stresses including bending and stretching conditions. In addition, because the environment of fuel cells is chemically tough due to the oxidizing and reducing conditions and there was no severe problem such as oxidation or ionization of Ag nanowires, it is also possible to speculate that not only mechanical

properties but chemical stability of Ag nanowires is compatible with fuel cells. Given that, we confirmed that the delamination of MEA occur either between the GDL and CL or between the CL and membrane.

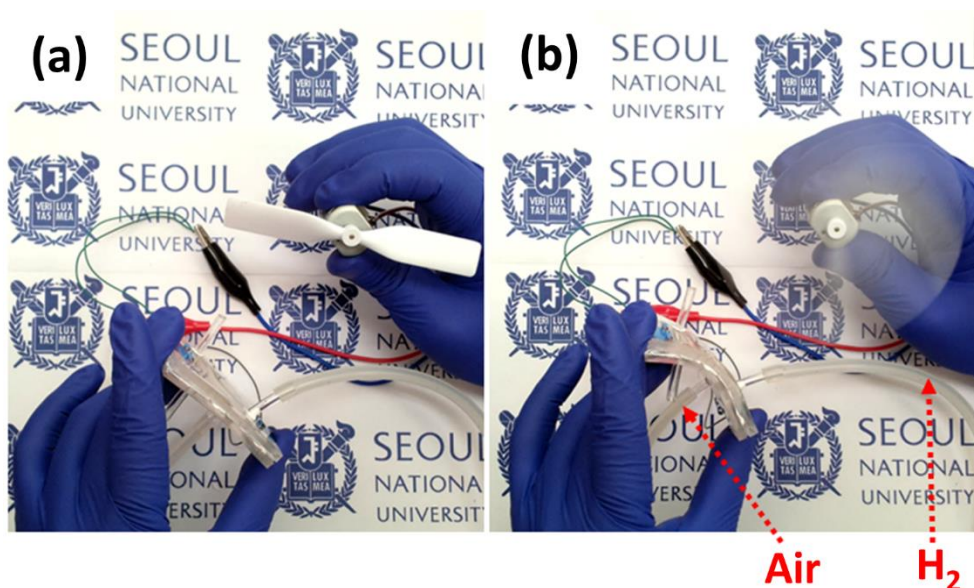


Fig. 3.1.8 Application of the flexible fuel cell. (a) An electric fan does not operate as the fuel cell is flat (b) but it operates as it is bent.

To verify the feasibility and the concept of our novel flexible fuel cells, we demonstrated the flexible fuel cell to power an electric fan; Figs. 3.1.8 (a) and (b) show its operation in flat and bent conditions, respectively. The fan operates by the fuel cell with bent position due to the enhanced power higher than the minimal power required to operate it in Fig. 3.1.8 (b), while it does not as it is flat in Fig. 3.1.8 (a). It means that the technological level of the flexible fuel cell in this study reaches at its direct application in the small electronics like electric fan.

3.1.4 Conclusion

In summary, we fabricated and demonstrated the bendable/flexible fuel cell based on PDMS flow-field plates and stretchable Ag nanowire percolation network based current collectors. The enhanced performance under a bending condition is mostly attributed to the significantly increased compressive stress onto MEA. Even though the low performance of the flexible fuel cell generally originates from the relatively low compressive stress inherently due to PDMS-based architecture, the flexible Ag nanowire electrodes significantly improves the electrical conductivity even in highly bent shape. We believe such application will contribute to the development of the flexible power sources for flexible electronics such as flexible displays, bio sensors, and epidermal applications.

3.2 Twisting Test

3.2.1 Introduction

This chapter complements the previous study that same flexible PEFC based on PDMS with Ag nanowire current collectors was characterized as it is twisted. The performances of flexible PEFC under various positions, torsion for example, should also be evaluated in order to investigate if it can be operated in the application of flexible electronics such as wearable or epidermal electronics. In this chapter, unlike the previous experiment about the bending test, the performance of the fuel cell rather decreases as it is twisted. In addition, the peak power density of the fuel cell is lower than even half of the peak power density in the bending test. This chapter investigates the reason for such results by similarly analyzing through FEM with same model used in Ch. 3.1.

3.2.2 Experimental

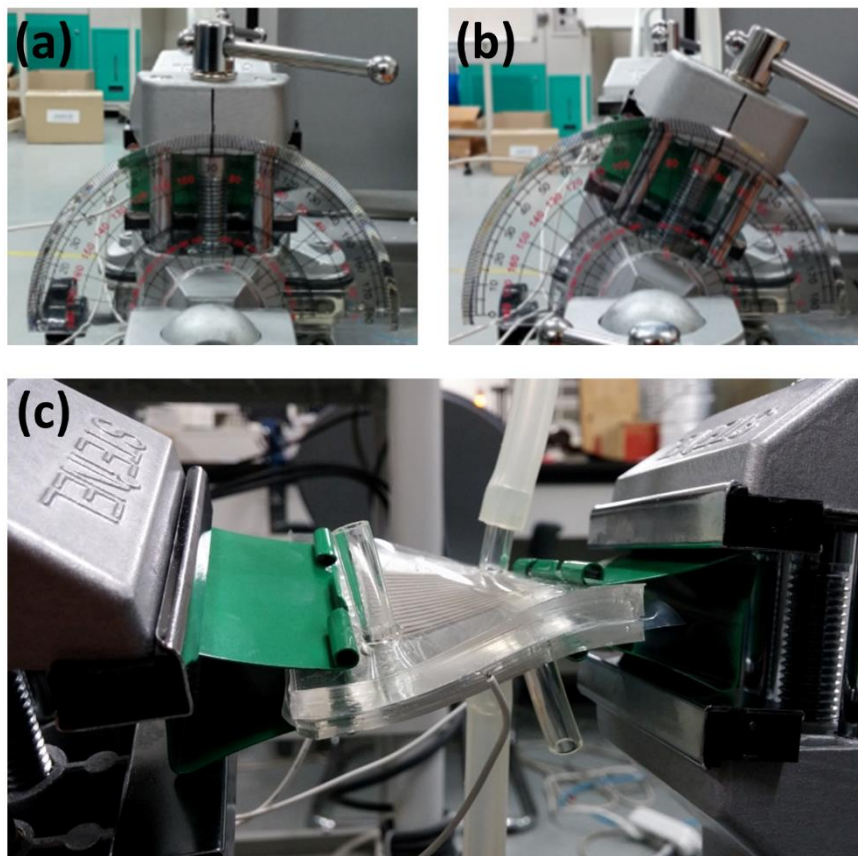


Fig. 3.2.1 Photographs of rotational vises for the twisting test of the flexible fuel cell. Twisting angles were set from (a) 0° to (b) 25° . (c) Flexible fuel cell under the twisting angle of 25° .

The flexible fuel cell was twisted using two same rotational vises (SV-1, Steinel, Germany). Here, a protractor was mounted on each rotational vise in order to twist the fuel cell precisely. Figures 3.2.1 (a) and (b) show the real pictures of protractor-mounted rotational vise at flat shape and 25° twisted conditions. The electrochemical

performances of the flexible fuel cell were measured at the twisting angles of 0, 5, 10, 15, 20, and 25°. Humidified pure hydrogen and air at standard temperature and pressure were supplied to the anode and cathode with the volumetric flow rates of 100 and 200 cm³/min, respectively. Before measuring the performances, the fuel cell was repetitively twisted and released in order to avoid measuring the performance at fresh conditions. After that, it was activated at constant 0.5 V for 30 minutes. The electrochemical characteristics of the fuel cell were investigated by using Solartron 1260/1287 (Solartron Analytical Co. United Kingdom). The I-V curves were measured from open-circuit voltage with the sweeping speed of 30 mV/s. After measuring the I-V curve, the fuel cell was stabilized by loading 0.5 V of constant voltage, same as the conditions of initial activation process, and electrochemical impedance was measured at 0.5 V. Sinusoidal voltage amplitude was 30 mV and frequency range was from 10⁵ to 2 Hz. The measured data was visualized through Nyquist plot as done in the previous chapter. Here, the electrochemical measurements started from the twisting angle of 0 to 25°. This characterization process was repeated in order to secure the reliability of the data. Figure 3.2.1(c) indicates the picture of flexible fuel cell at the twisting angle of 25°. Finally, FEM was performed using COMSOL multiphysics 4.2 tool again in order to find out the distribution of generated stress by twisting inside the fuel cell.

3.2.3 Results and Discussion

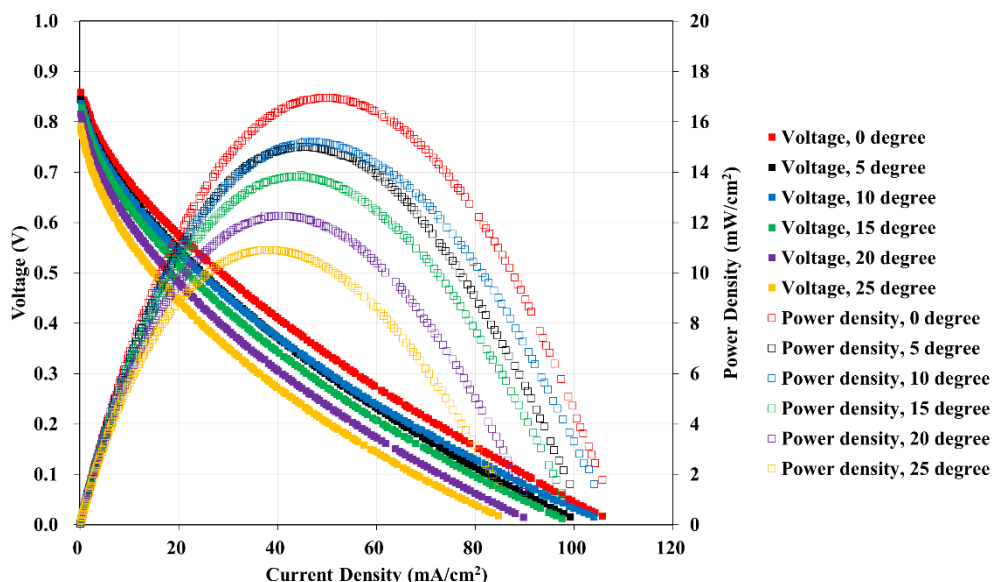


Fig. 3.2.2 Current-voltage and current-power density curves of the flexible fuel cell measured at the twisting angles of 0, 5, 10, 15, 20, and 25°. Filled and empty marks represent voltage and power density, respectively.

The I-V characteristics of the flexible PEFC under twisting are indicated in Fig. 3.2.2. OCV at flat condition was 0.86 V, and this OCV decreased to 0.8 V as it is twisted up to 25°. Because the OCV is directly related to Nernst potential, it can be thought of that the concentrations, or pressure, of hydrogen and air inside fuel cell were changed as long as reaction site temperature was constant and there was no side reaction. In real, an OCV of fuel cell is measured as a mixed potential by non-uniformly distributed hydrogen and air in electrochemically reactive site. It was

reported in literature that the concentration of the reactant is different partially from each point of MEA, although only one kind of reactant is supplied carefully to one side of the MEA [70].

The peak power densities of the flexible PEFC at flat and 25° twisted shapes were 16.8 and 10.9 mW/cm², respectively. Here, it is thought that the aforementioned non-uniform distribution of the reactants not only reduces OCV but also impedes the electrochemical reaction kinetics. The I-V characteristics of the fuel cell follow Butler-Volmer behavior at current-flowing region, and there are also reactants concentration terms in Butler-Volmer equation [10]. Not only the OCV but also the performance do the concentrations of the reactants affect to. Accordingly, it is speculated that the flexible PEFC showed the decreasing tendency of the power density as it is gradually twisted.

The peak power density of 16.8 mW/cm² as the fuel cell is flat is comparatively lower value as compared with the previous studies [46,47]. We previously showed that the electrochemical performance of the flexible PEFC with the Ag nanowire-coated PDMS is highly affected by the internal stress generated by bending [46]. Here, the difference between previous and this study is that the ratios of PDMS and curing agent were 10:1 and 15:1, respectively. Young's moduli of 15:1 and 10:1 of PDMS ratios are 3.60×10^5 and 7.50×10^5 Pa, respectively [71]. It means that generated internal stress within flexible PEFC made of 10:1 PDMS is more than 2 times higher than that of 15:1 PDMS. Accordingly, the performance difference of flexible PEFC might be caused from the difference of generated internal stress even at neutral

position. However, the decreasing tendency of the performance as the fuel cell is gradually twisted is still not clear to understand. It is discussed hereafter.

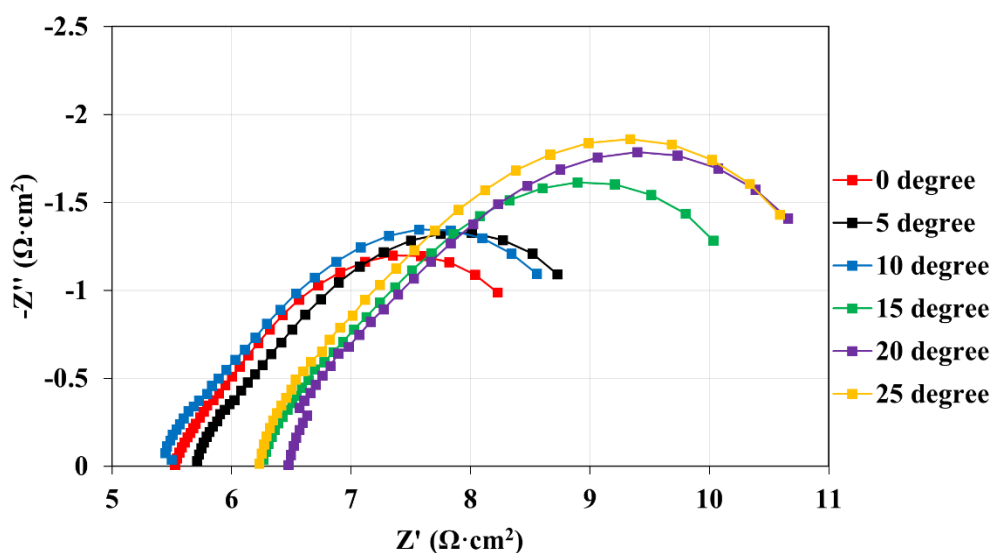


Fig. 3.2.3 The electrochemical impedance spectra of the flexible fuel cell at 0.5 V vs. RHE in Fig. 3.2.2, measured at the twisting angles of 0, 5, 10, 15, 20, and 25°.

Fig. 3.2.3 shows the variation of the EIS of the flexible PEFC with respect to the twisting angle from 0 to 25° at 0.5 V of the I-V curves in Fig. 3.2.2. In this graph, the ohmic and charge transfer resistances generally show increasing tendency as it is twisted. In other words, the torsion applied to the flexible PEFC increases both the ohmic and charge transfer resistances. Ohmic resistance depends on the temperature of reaction sites, water content in electrolyte membrane, electrical resistance including contact resistance between every components, while charge transfer resistance is related to reactants concentration, temperature, activation energy of reaction, and exchange current density [16]. In this experiment, the water content in electrolyte membrane, temperature of reaction site, and exchange current density are constant because only torsion is applied to one fuel cell without the change of any components composing the fuel cell. It means that all the components such as catalyst layer and electrolyte membrane which is directly related to activation energy and exchange current density were kept same. Accordingly, concentrations, or pressures, of hydrogen and air and electrical resistance were affected and changed by twisting. Two variables, concentrations of reactants and electrical resistance, particularly might affect charge transfer and ohmic resistances.

It is speculated that, as mentioned above, the charge transfer resistance can be deduced from Butler-Volmer behavior and inhomogeneous distributions of hydrogen and air are considered as main factors for the increase of the charge transfer resistance. Especially, the inhomogeneous distributions of the reactants inside the fuel cell could lead to the decreasing effect of electrochemically active area, by which charge transfer resistance increases [62]. In our flexible PEFC, the as-described effect seems

to occur and that is why charge transfer resistance was increased. This result corresponds with the variation of the OCV in Fig. 3.2.2 that the OCV was decreased by the partially decreased concentration at the edge of the reactive area in the MEA.

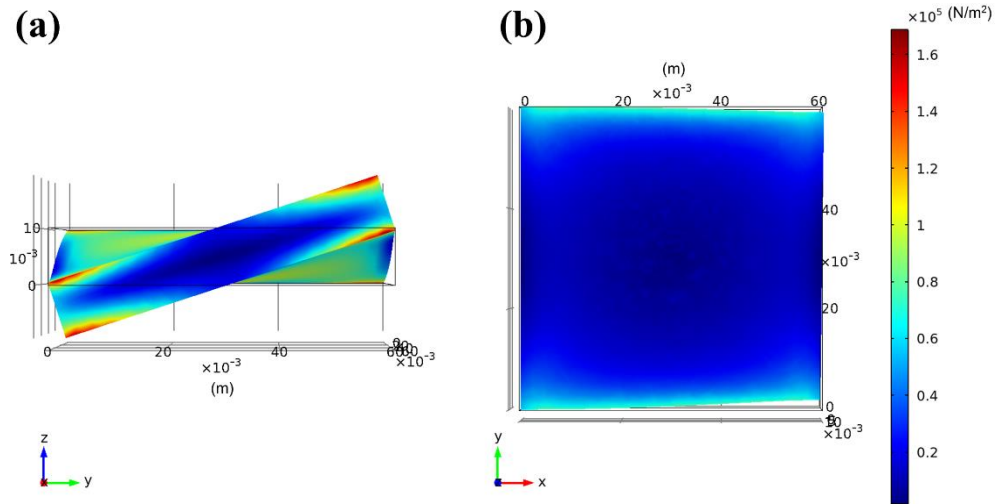


Fig. 3.2.4 Finite element analysis of the generated von Mises stress by twisting in the flexible fuel cell. (a) Side view of 3-dimensional model of flexible fuel cell and (b) top view of center slice of the model.

Contact resistance between electrolyte membrane, GDL, and Ag nanowires can be the cause for the increase of the ohmic resistance in the flexible PEFC. Contact resistance has interesting characteristic that it decreases exponentially as the compressive stress generated between two conducting objects increases [64]. In order to estimate this contact resistance between MEA and CL or Ag nanowires in this study, solid-mechanical FEM was used again. Because PDMS is kind of hyperelastic materials, Mooney-Rivlin model was adopted again to describe the PDMS. Although the model presented here is 3-dimensional, which is 2-dimensional in Ch. 3.1, the same material properties were used here in order the data here with the previous data in Ch. 3.1. The only difference between the FEM model in Ch. 3.1 and here is Young's modulus of PDMS. In the previous chapter, the ratio of PDMS solution and a curing agent was 10:1 while it is 15:1 here (This study intentionally employed 15:1 PDMS because the size of the fuel cell is not big and thickness is relatively thick so it is not easy to apply the twisting load.). Young's modulus used in this study is 360 kPa. The information of the analysis in detail is indicated elsewhere [46,47]. Figs. 3.2.4 (a) and (b) show the side view of the calculated result of the flexible PDMS by using the as-described conditions and the top view of the center-slice, respectively. In Fig. 3.2.4 (b), this stress distribution can be regarded as the stress applied on MEA because the MEA is located at the center plane. According to this stress distribution, the generated stress by twisting is concentrated to the edge of the fuel cell. However, it is observable that almost no stress is generated at the center part in Fig. 3.2.4 (b) because the absolute value of the stress is significantly low. It can be found from Fig. 3.2.4 (a) that generated stress by torsion is heavily focused on the edge of top and

bottom surfaces while it is not in the center. As a result, stress is not the main reason for the decrease of the electrochemical performance of the flexible PEFC.

If the variation of contact resistance by internal stress is not the main cause, there would be a counter-balancing effect of the normal and shear stress in von Mises stress which is composite stress of principal stresses. If it is the case, shear stress could detach hot-pressed GDL from MEA and lead to the performance loss. Interestingly, it corresponds with the result in Fig. 3.2.3 that the ohmic resistance increases and the charge transfer resistance decreases as the flexible fuel cell is twisted. Such variation of the resistances is attributed to the detachment of the GDL from the MEA and regarding the decreased of TPBs. If it is true, the performance variation of flexible PEFC highly depends on ruggedness of the MEA. Consequently, it is speculated that the operation of the flexible PEFC is not significantly affected by torsion as long as the MEA endures the twisting.

3.2.4 Conclusion

The flexible fuel cell based on PDMS flow-field plates coated with Ag nanowire current collectors was fabricated and characterized as it is twisted. It showed the decreasing tendency of electrochemical performance as it is gradually twisted. Through the EIS investigation, it was found that the increase of the ohmic and charge transfer resistances were the causes for the performance loss of the flexible PEFC. Although there was no negative effect from the stress on the performance of the flexible PEFC because there was little variation of internal stress by twisting, the inhomogeneous distributions of hydrogen and air are speculated to be a reason for decrease of performance. Damaged MEA by shear stress was also thought of as another factor for the decrease of the performance.

3.3 Combined Bending and Twisting Test

3.3.1 Introduction

This study shows the performance variation of the flexible fuel cell based on Ag nanowire current collectors under simultaneous bending and twisting. Because most of wearable electronics are subject to both bending and twisting in the environment of real applications, it should be investigated whether it operates well in this environment. In this manner, this study first shows the possibility that this type of flexible fuel cells can be used in real applications. The performance here was also decreased as it was twisted. Interestingly, the performance of the fuel cell with bending was higher than that without bending at the same twisting degree. Based on the previous results about the relation between the assembly pressure and the performance, this study conducted 3-dimensional stress analysis using FEM. As a result, mixed bending and twisting load generated higher assembly pressure than only twisting load. Only twisting load also generated the assembly pressure but its intensity was not dominant than the pressure by bending. The higher performance in the case with mixed bending and twisting load is thought to be induced from the difference of the pressure by ‘bending component’. When it was highly twisted, the pressure reaches at not negligible range while this pressure seems to be canceled by unknown factors suggested in the previous research [48]. This correlation is visualized by relating the calculated stresses to the performances and electrode/electrolyte resistances.

3.3.2 Experimental

Hydrogen and air were supplied to the fuel cell with the volumetric flow rate of 100 and 200 cm³/min, respectively. Those were humidified by flowing through a water canister at room temperature. Before measuring the performance, the fuel cell was activated by operating it at 0.5 V for an hour in order to avoid the instable operation resulting from the deficient hydration of the Nafion[®] and self-heat-up. I-V curves were measured using Solartron 1260/1287 (Solartron Analytical Co., United Kingdom). Potentiodynamic mode was used here. The voltage sweep rate was 30 mV/s and started measuring from OCV. Right after measuring the I-V curve, corresponding electrochemical impedance was measured. Sinusoidal voltage input at 0.7 V with the amplitude of 30 mV was applied to the cell. The range of frequency was from 10⁵ to 2 Hz, from high to low frequency. The measured impedance spectra were then fitted to theoretical equivalent circuit to calculate electrolyte and electrode resistances using Z plot software (Solartron Analytical Inc., United Kingdom). This sequence was repeated from the twisting degree of 0 to 25° (0, 5, 10, 15, 20, and 25°, total 6 cases). After measuring the I-V curves and corresponding impedance spectra, bending load was additionally applied on it with the bending radius of 36.3 cm. Accordingly, total 12 cases were investigated (0 - 25° of twisting, infinite and 36.3 cm of bending radius). The bending and twisting load was applied using two ball-joint bises (SV-1, Steinel Co., Germany) with add-on protractors. Figure 3.3.1 shows the picture of the flexible fuel cell described above under both bending and twisting load. Compressive stress distribution inside the fuel cell was calculated using

COMSOL Multiphysics 4.2 software. 3-dimensional solid-mechanical model was used and stationary solution was obtained.

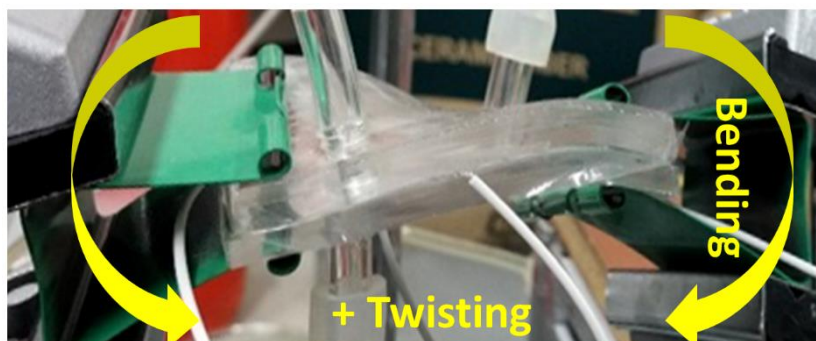


Fig. 3.3.1 The picture of the flexible fuel cell under mixed bending and twisting load.

3.3.3 Results and Discussion

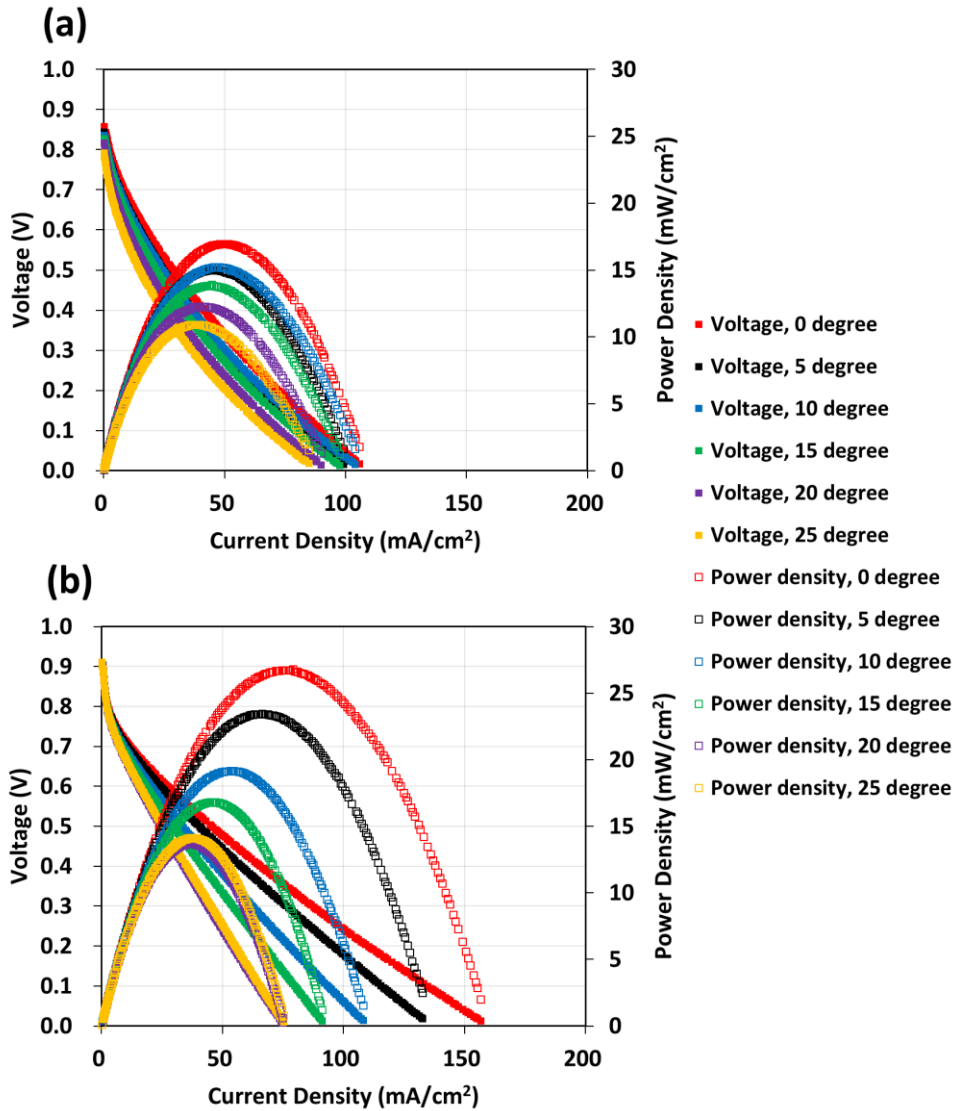


Fig. 3.3.2 I-V and I-P curves of the flexible fuel cell. (a) and (b) are the cases of the flexible fuel cell with flat and bent ($R = 36.3 \text{ cm}$) shapes, respectively. The performances were measured with respect to the simultaneous twisting angles of 0, 5, 10, 15, 20, and 25°. (a) is same as the graph in Fig. 3.2.2 but reprinted here for the comparison with (b).

All the previous chapters about the flexible fuel cells based on this template (PDMS with Ag nanowire current collectors) showed that the variation of the performance by bending or twisting is due to the internal stress generated by bending [46,47,50,72]. Based on it, the results of this study are hereafter interpreted in the same manner. Figures 3.2.2 (a) and (b) show the I-V curves of the as-fabricated flexible fuel cell at various twisting degree with bending and without bending, respectively. The OCV in Fig. 3.2.2 (a) slightly decreases from 0.86 to 0.8 V with the increasing twisting degree while the OCV in Fig. 3.2.2 (b) stays at 0.91 V regardless of twisting degree. The OCV can be described as Nernst potential and is affected by two parameters: environmental temperature and concentrations of the reactants (hydrogen and oxygen in the case of fuel cells). In both fuel cells in Fig. 3.2.2 (a) and (b), the temperature is same so the concentrations of hydrogen in anode and oxygen in cathode are the factors for this difference of the OCV variations. Because hydrogen and air were supplied with same volumetric rate in both cases, it is supposed that the hydrogen and air were not distributed uniformly in the reactive area. Asghari et al. showed experimentally that the non-uniform assembly pressure on MEA deteriorates the performance of the fuel cell by causing non-uniform distributions of hydrogen and air [63]. Same phenomena have been reported elsewhere [73–78]. Accordingly, it is thought that the reason for the higher OCVs in Fig. 3.2.2 (a) than (b) is the assembly pressure induced by bending, leading to the uniform distribution of hydrogen and air. The detrimental effect by twisting seems to be compensated by the advantageous effect from bending in Fig. 3.2.2 (b). However, it is not the case in Fig. 3.2.2 (a) that there might be not enough assembly pressure because there was no bending.

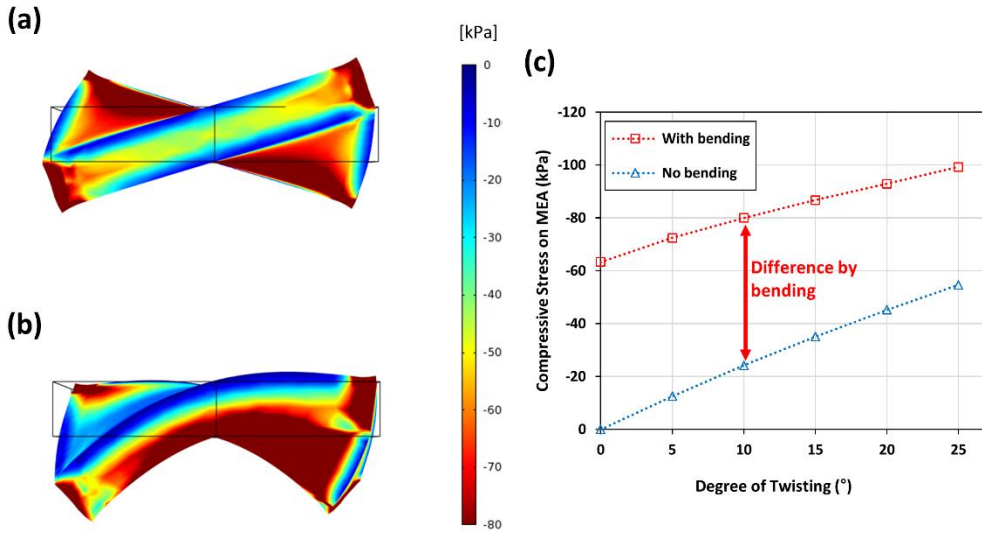


Fig. 3.3.3 Compressive stress distribution of the flexible fuel cell under (a) twisting and (b) mixed twisting and bending loads. (c) Compressive stress onto MEA with respect to the variation of the twisting angle in the cases of (a) and (b).

In real, the calculated assembly pressure, *i.e.* the compressive stress on MEA, is higher in the case with bending. Figure 3.3.3 shows the simulation results of the compressive stress perpendicular to MEA. In order to simulate the displacement and resulting stress, one of hyperelastic model, Mooney-Rivlin model, was used. This model is same as that used in the previous researches [46,47,50] (The contents of the previous chapters), where the details such as governing equations, boundary conditions, and all the physical constants for the model. According to Fig. 3.3.3 (a) and (b), it is clearly seen that the center part in Fig. 3.3.3 (b) is redder than in Fig. 3.3.3 (a), meaning that the compressive stress onto MEA is stronger as the bending component is additionally applied with twisting. The compressive stresses at the grids

corresponding to the location of MEA were averaged and plotted with respect to the degree of twisting in Fig. 3.3.3 (c). As expected, the compressive stress on MEA by mixed bending and twisting load is quite higher than by only twisting in all degrees of twisting. In particular, it is noticed that the difference between two cases is constant regardless of the degree of twisting. It is thought that although bending and twisting are applied simultaneously, each load component affects to the final compressive stress on MEA independently. This results correspond with the variation of the I-V curves in Fig. 3.3.2 that only additional bending load led to the performance increase in all twisting cases.

However, as discussed in the previous research, it is still not clear why the performance decreases with the increasing twisting angle [48]. It was suggested that it is because the MEA is permanently damaged by twisting. The bending load does not generate relatively high strain because the MEA is located at the center line which corresponds with the neutral axis [79]. However, twisting generates the strain although the intensity is not strong [51]. Here, the MEA is composed of stretchable electrolyte membrane (Nafion[®]) and brittle GDL (carbon paper) and these were all attached with each other. That is why the strain induced from twisting would detach the Nafion[®] and carbon papers. Furthermore, twisting the fuel cell might tear the carbon papers if the adhesion between Nafion[®] and carbon paper was stronger than the fractural limitation of the carbon paper. If it is the case, it affects to not only the OCV but also the performance of the flexible fuel cell. Both Fig. 3.3.2 (a) and (b) correspond well with this explanation that the OCV and overall performance decrease as it is twisted.

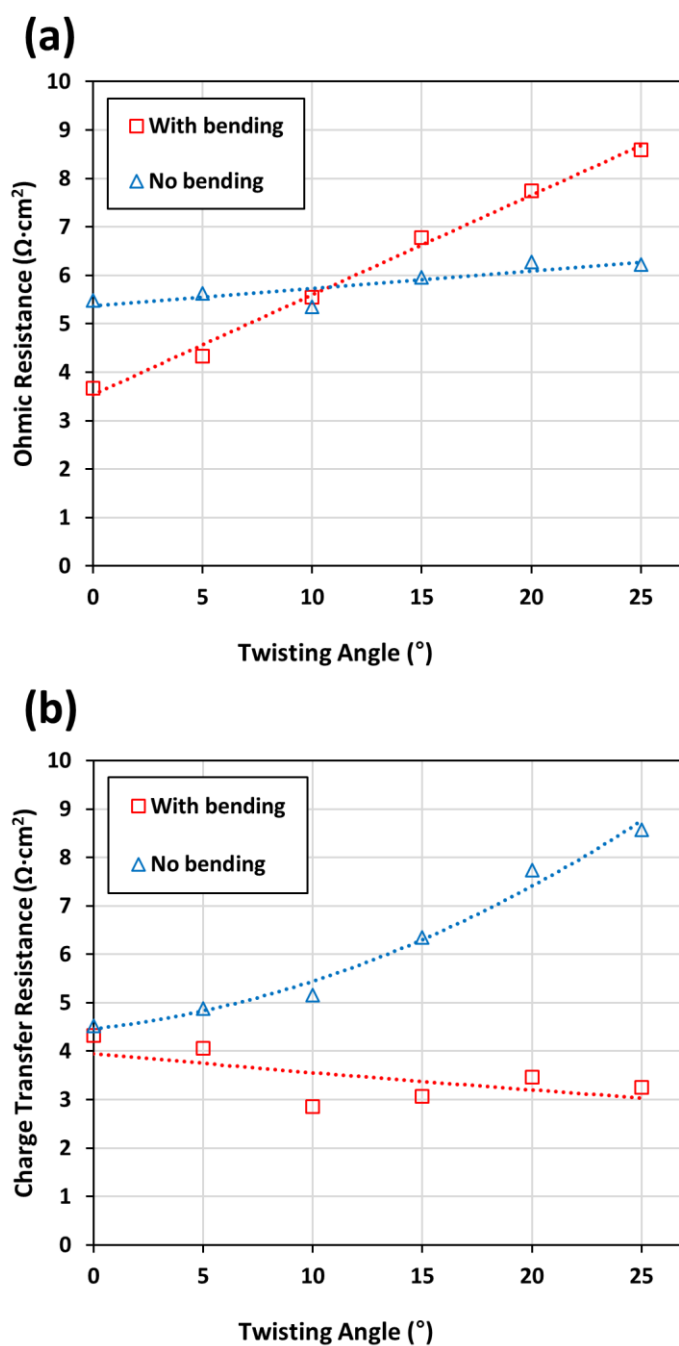


Fig. 3.3.4 The (a) electrolyte (ohmic) and (b) electrode (charge transfer) resistances with respect to the twisting angle corresponding to Fig. 3.3.2.

The effects on the performance by bending and twisting can also be found clearly in Fig. 3.3.4 where the variation of the estimated electrolyte and electrode resistances are plotted. The method of the calculation is described in our previous research [80]. Because the performance of typical PEFCs can be fitted to a standard polarization model, the flexible fuel cell can also be fitted into the model [16]. Particularly, since there is no mass transport loss at high current density region in all the curves in Fig. 3.3.2, the losses inside the flexible fuel cell can be specified into two resistances: electrolyte and electrode resistances. Because the overall performances in Fig. 3.3.2(b) are higher than in Fig. 3.3.2(a), it could be predicted that at least one or two of such resistances in the fuel cell with bending is lower than without bending. In real, the electrode resistance in Fig. 3.3.4(b) coincide with this prediction while it does not in Fig. 3.3.4(a). In Fig. 3.3.4(a), the electrolyte resistance of the fuel cell under bending load is lower at low degree of twisting ($< 10^\circ$). However, the electrolyte resistance is negligible if investigated in accordance with the standard polarization model. The ohmic loss is expressed as the multiplication of current density and the electrolyte resistance in Fig. 3.3.4(a). By subtracting the ohmic loss from the I-V curves in Fig. 3.3.2, the influence of the electrolyte and electrode resistances can be investigated. As a result, the influence of the electrode resistance is found out to be dominant. That is why the difference of the power densities in Figs. 3.3.2(a) and (b) is at low degree of twisting is small while it is higher at high degree of twisting. Identical variation of this difference can be found in Fig. 3.3.4(b) that the difference of the electrode resistances increases with the increasing degree of twisting.

3.3.4 Conclusion

The flexible fuel cells based on Ag nanowire current collectors and PDMS were fabricated. The I-V behaviors and corresponding impedance spectra were measured as the fuel cell was subject to bending and twisting simultaneously. As a result, the performance of the fuel cell under both bending and twisting load showed higher maximal power density than under only twisting. By calculating the distribution of the assembly pressure inside the fuel cell via FEM, it was found that the compressive stress on MEA by mixed bending and twisting is stronger than by only twisting. The higher performance in the fuel cell with mixed bending and twisting seems to come from this difference of the compressive stresses. The stress generated by twisting was not influential than by bending. Although twisting load also generated the compressive stress on MEA, the other factor coming with twisting such as strain seems to make the MEA deteriorate. From the impedance spectra, it was found that an electrode resistance is dominant in our flexible fuel cell. The electrode resistance of the fuel cell under only twisting gradually increased with the increasing degree of twisting while that under mixed bending and twisting was slightly decreased. It is thought that the advantageous effect from bending compensated the detrimental effect from twisting.

Chapter 4. Flexible PEFC: Direct Compression Test

4.1 Introduction

We have previously investigated the performance of this fuel cell as a function of the bending radius and twisting angle. Interestingly, the electrochemical performance increases with increasing curvature. This phenomenon was explained by analyzing the internal compressive stress inside the fuel cell, calculated using a finite element method (FEM) model. The performance enhancement was attributed to the compressive stress induced on membrane-electrode assembly (MEA) by bending, which was hypothesized to reduce both the contact and charge transfer resistances. This conclusion was indirectly proven by showing that even higher performance could be achieved by asymmetrically offsetting the MEA from the midline of the fuel cell assembly, where the FEM model predicted higher compressive stress under bending [47]. The performance of the flexible fuel cell was also examined under the more complex stress-state conditions caused by twisting [48].

This study examines effects on the performance at much lower assembly pressures compared to those applied in general nonflexible fuel cells. The relation between the electrochemical performance and the assembly pressure of standard (*i.e.*, nonflexible) PEFCs has been widely discussed in the literature [73–78]. However, the softer, more compliant materials especially used in flexible fuel cell construction prevent the application of high assembly stresses; this is an important issue facing

flexible fuel cells compared to their inflexible, rigid counterparts. To our knowledge, this is the first study to quantitatively examine PEFC performance beyond the flexible fuel cell at low assembly pressure (0 - 450 kPa). The goal of this study is to directly (*in-situ*) measure the pressure on the MEA, thereby enabling quantitative comparison with previous experiments that provided only an indirect estimation (via FEM simulations) of the relationship between the performance and assembly pressure [46,47]. By comparing these two datasets and the data from the simulation, insights into additional factors affecting fuel cell performance under bending, such as lateral shear stresses and deteriorative effect of bent flow channels, are obtained.

4.2 Experimental

As shown in Fig. 4.1(a), the assembled flexible fuel cell was sandwiched between two rigid plates made of acryl. Inlet and outlet holes were machined inside the rigid plates in order to supply hydrogen and air into the anode and cathode, respectively. Same silicone sealant used above was used again to provide a gas-tight seal between the rigid plates and fuel cell. The mounted fuel cell was oriented in the horizontal position. A metal support was located between the fuel cell and a force sensor (BS-5200, Bongshin Loadcell Co., Republic of Korea) to distribute the force homogeneously to the MEA. A picture of the test setup is shown in Fig. 1(b).

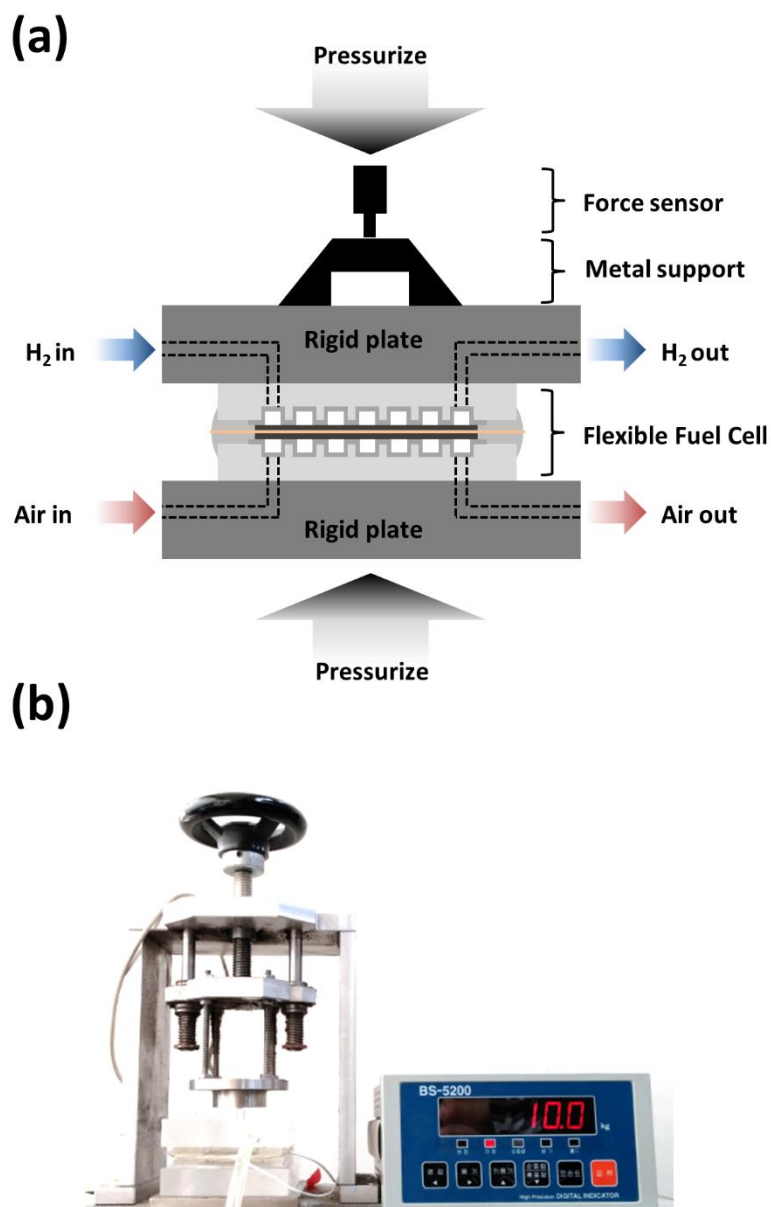


Fig. 4.1 (a) Schematic of experimental setup. (b) Picture of the force sensor and the experimental setup corresponding to (a).

Before measuring the performance of the fuel cell, it was operated at 0.4 V and 80 °C for 12 hours to fully activate the MEA and ensure stable steady-state operation. The volumetric flow rates of hydrogen and air were 500 and 1000 cm³/min, respectively both during the activation process and subsequent fuel cell testing. The fuel cell performance was measured under a range of compressive forces, which were all labeled in Table 4.1. The current-voltage (I-V) characteristics were measured using potentiodynamic mode starting from the open-circuit voltage (OCV) with a sweep rate of 30 mV/s using Solartron 1260/1287 electrochemical measurement system (Solartron Analytical Co., UK). The I-V sweeps were halted at 280 mA/cm² (2.5 A total current). Immediately after measuring each I-V polarization, an electrochemical impedance spectrum (EIS) corresponding to the measured I-V curve was measured at 0.5 V. EIS measurements used a 30 mV sinusoidal voltage amplitude with a frequency range from 10⁵ to 2 Hz. Z-View software was used to fit the impedance spectra to an equivalent circuit model in order to calculate charge transfer resistances. This measurement process was repeated at each compressive force in Table 1. In order to secure the reliability of the data, the measurement was repeated and representative voltages and corresponding power densities were averaged out to quantitatively match one to one the compressive force onto MEA and the performance.

Legend number	Compressive stress on MEA (kPa)
1	0
2	2
3	13
4	34
5	57
6	89
7	111
8	166
9	220
10	329
11	438

Table 4.1 The numbers marked in Figs. 4.2 and 4.3, and corresponding assembly pressure onto MEA.

4.3 Results and Discussion

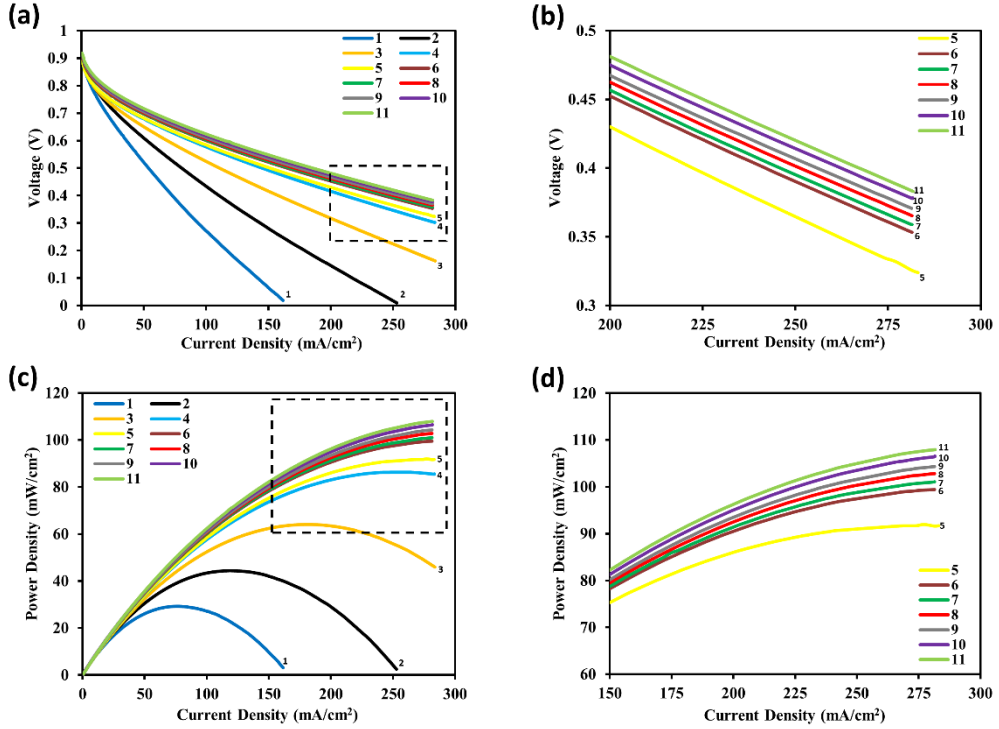


Fig. 4.2 (a) I-V curves of the flexible fuel cell under various assembly pressures shown in Table 1. (b) Magnified graph of the dashed box in (a). (c) I-P curves of the flexible fuel cell corresponding to (a). (d) Magnified graph of the dashed box in (c).

Figure 4.2 shows the I-V and current-power (I-P) curves of the flexible fuel cell as a function of the assembly pressure, *i.e.* the compressive stress onto the MEA. All measurements produced a stable and consistent OCV of approximately 0.95 V, indicating that the cell sealing is not compromised during the course of the loading and unloading experiment. The I-V results are consistent with previous observations

showing an increase in fuel cell performance under bending. Because significant excess hydrogen and air compared to stoichiometric amounts were supplied to the fuel cell to avoid mass transport loss, there is no sharp voltage drop in the I-V curves in Figs 4.2 (a) and (b). As indicated in Fig. 4.2 (d), the achieved maximal power density in this study was 110 mW/cm^2 and this is one of the highest values among the fully flexible fuel cells reported in the literature [27,28,31,46–48]. Although the maximal power density of 110 mW/cm^2 is appreciably lower than that of the state-of-the-art rigid PEFCs, it is still reasonable considering that the cell was operated with dry hydrogen/air at room temperature and has ‘flexibility’.

Previous bending studies using this same fuel cell architecture [46,47] showed a maximum in performance at an optimum bending radius, with a plateau or even a decrease in performance upon further bending. In this study, however, we observe a continuous increase in performance with increased load, although the performance gains begin to asymptote at the higher applied loads ($> 90 \text{ kPa}$) as shown in Figs. 4.2(c) and (d). This distinction points to important differences between the uniaxial compressive loads examined here and the more complex stress-states induced by the bending studies examined previously. This will be discussed in more detail later.

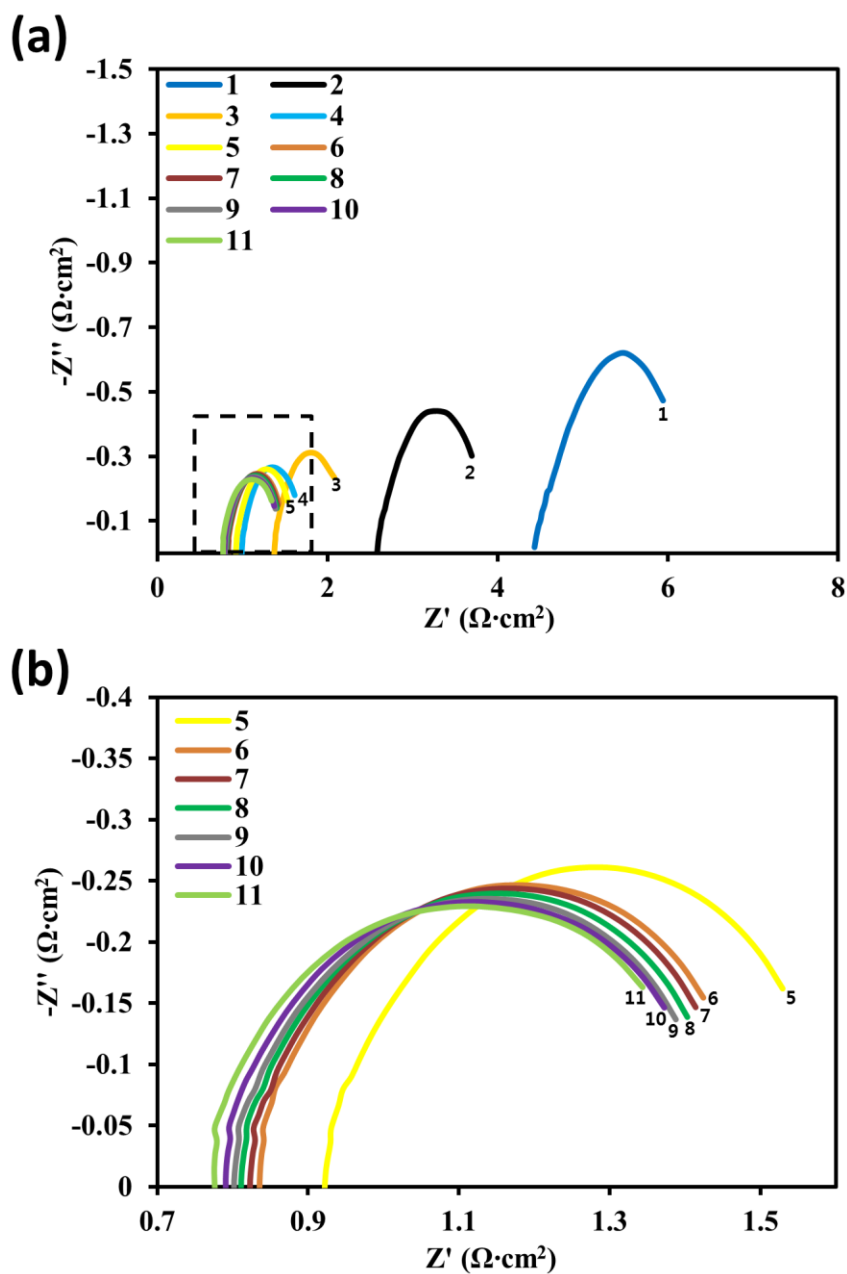


Fig. 4.3 (a) EIS corresponding to the current-voltage curves at 0.5 V in Fig. 4.2. (b) Magnified graph of the dashed box in (a).

Figure 4.3 shows the electrochemical impedance spectra at 0.5 V in I-V curves in Fig. 4.2. The impedances were also measured to compare the relation between the stress and ohmic/charge transfer resistances to those in [46] and [47]. As expected from the I-V curves, the performance enhancement by the increased compressive stress was attributed to the reduction of both ohmic and charge transfer resistances. Here, ohmic resistance was obtained from the first intersection of the impedance spectrum on Z' axis and charge transfer resistance from the diameter of the half-circle [16,80]. Like the variation tendency of the I-V curve, the ohmic and charge transfer resistances decrease exponentially (Fig. 4.3 (a)) but the decrement of both resistances gradually become small (Fig. 4.3 (b)). From this figure, it can be identified that the compressive stress on the MEA was the cause of the performance enhancement. The decrease of the ohmic resistance with the increasing pressure can be explained by the following equation:

$$R = \sum_i R_{\text{bulk}i} + \sum_j R_{\text{contact}j} \quad (4.1)$$

where R_Ω , R_{bulk} and R_{contact} indicate measured ohmic resistance, the resistance of the component itself and contact resistance, respectively. Because a fuel cell can be described as the serial connection of all the components, the total ohmic resistance can be described as the eq. (4.1). Among the terms, the contact resistances inside the fuel cell decrease exponentially as the compression increases [43,63]. Not only contact but also bulk resistances change when the assembly pressure of the fuel cell

changes. It was reported that the resistance of the GDL contributes certain portion of R_{Ω} [81]. It is thought that the decreased charge transfer resistance with the increasing assembly pressure is that the microstructure of the GDL might be stabilized by proper assembly pressure. The interfacial contact between Pt/C, Nafion[®], and pores might also be optimized from the assembly pressure. It would bear the easy diffusion of the reactants into the triple phase boundary (TPB).

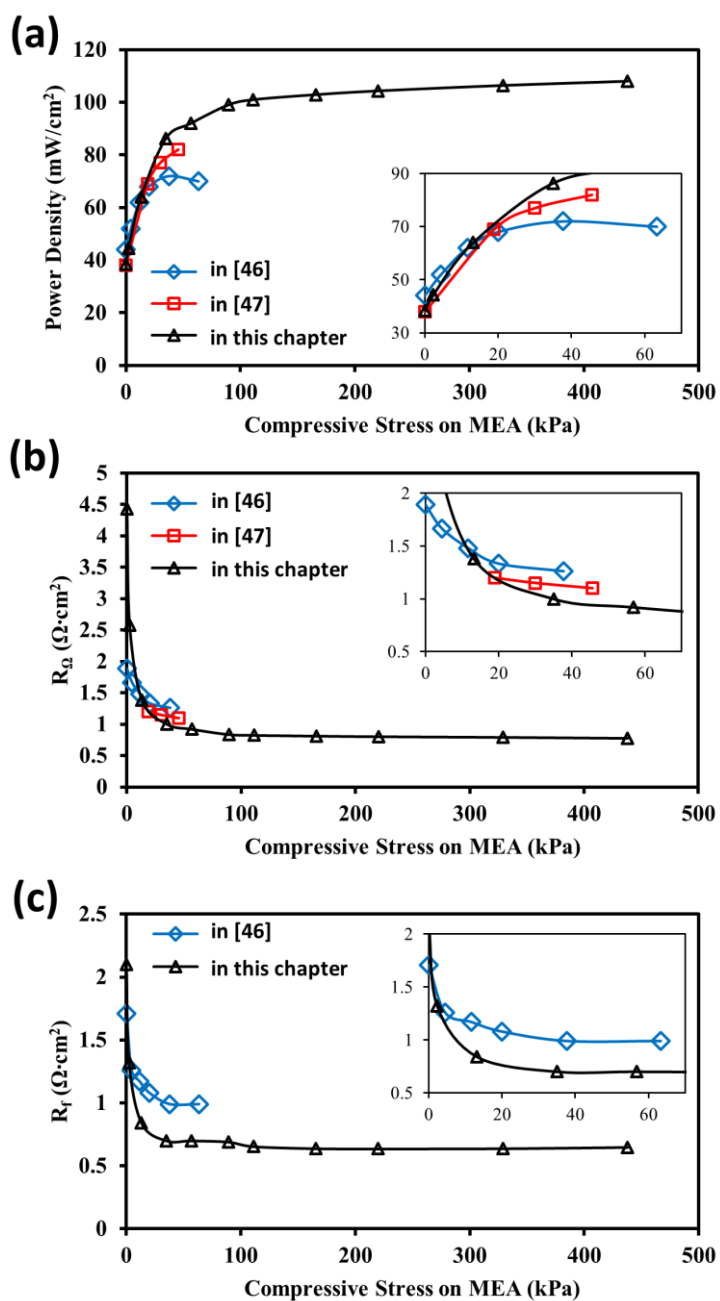


Fig. 4.4 (a) Quantitative comparison of (a) peak power densities, (b) ohmic and (c) charge transfer resistances at various assembly pressures. All insets are magnified graphs at low assembly pressure onto MEA.

In Fig. 4.4(a), the peak power densities in this study with respect to assembly pressures were compared with those of the previous researches. The variation tendencies of each maximal power density are similar with each other. The power densities in all studies increase clearly as the compressive stress onto MEA increase except the case of [46] at high compressive stress range. It is thought that this slight decrease of the result of [46] at relatively high compressive stress is attributed to the loss not from the compression but from bending, which is discussed later in detail. The corresponding variations of the ohmic and charge transfer resistances in Figs. 4.4(b) and (c) are matched with the power density variation in Fig. 4.4(a). The peak power densities in this study at low compressive stress (< 2 kPa) are almost same or even lower than those in [46] and [47] (Fig. 4.5(a)). It is because the clamps holding the flexible fuel cell in [46] and [47] generated small compressive stress to the MEA and it was propagated to where the MEA was located. That is why it is thought the compressive stress on MEA is higher in real than the calculated result. Although the propagated stress was very weak compared to that generated by bending, it can be found through the data of this study in Fig. 4.4 (a) that this weak compressive stress affects highly to the performance of the fuel cell at the lowest compressive stress range.

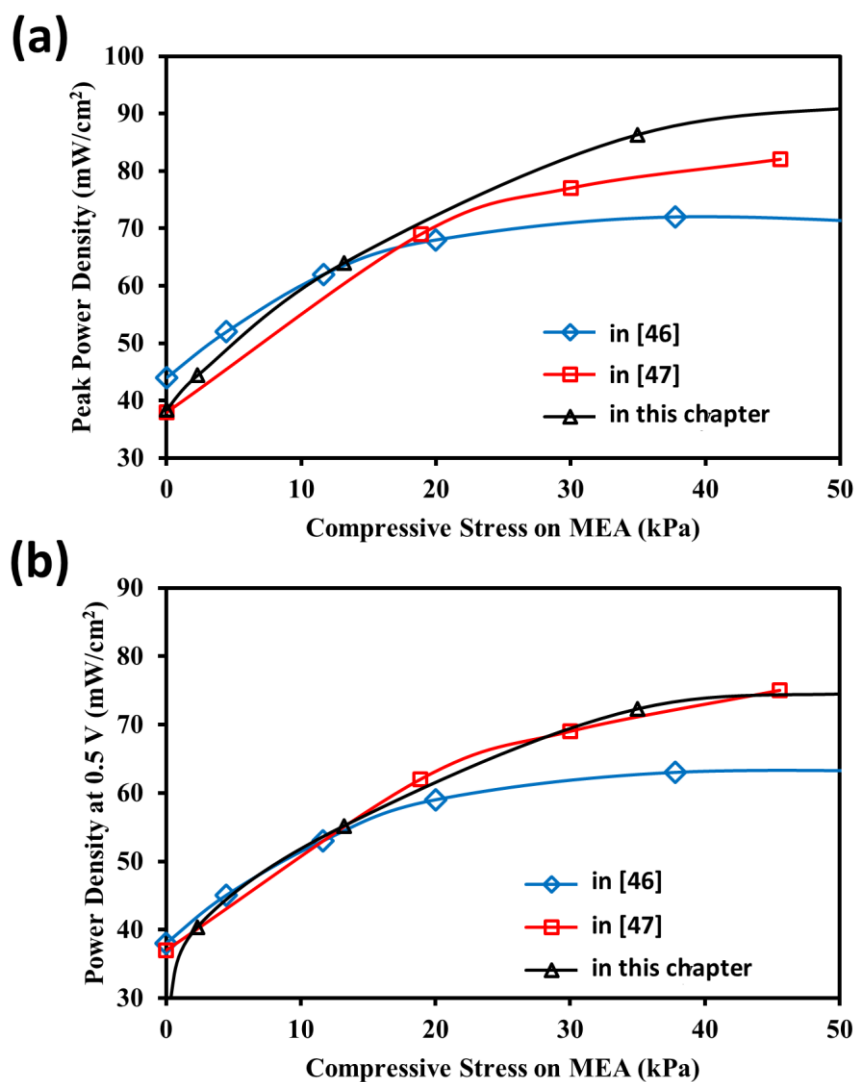


Fig. 4.5 (a) Magnified graph at low assembly pressure onto MEA in Fig. 4.4 (a). (b) Quantitative comparison of power densities at 0.5 V with respect to the assembly pressure. (a) is quite similar to the inset in Fig. 4.5(a) but shown here again to compare it to (b).

Especially, the power density at 0.5 V rather than the maximal power density was investigated in Fig. 4.5 (b) because the impedance was measured at 0.5 V so it is more reasonable and accurate to take the power densities at 0.5 V into account. According to Fig. 4.5 (b), the data of this study and [47] show good coincidence. Interestingly, the difference between the data of this study and [46] becomes larger as the compressive stress on MEA increases. It seems that this phenomenon comes from the difference of the bending radii of those in [47] and [46]. It was suggested and demonstrated previously in [47] that the compressive stress on MEA can be increased while the bending radius of the fuel cell is kept constant by just offsetting the location of the MEA slightly out of the center neutral line. In other words, the flexible fuel cell in [46] was bent more than in [47] at the same compressive stress on MEA. Accordingly, it is believed that the severely bent shape of the fuel cell caused the performance difference at the effective force range from 20 to 50 kPa. It can be also supported by the Figs. 4.4 (b) and (c) that the differences of the ohmic and charge transfer resistances become larger as the compressive stress increases (There is no result of [47] in Fig. 4.4 (c) because the charge transfer resistance was measured at a different voltage). Here are possible scenarios for it: inhomogeneous distribution of hydrogen and air, delamination between Nafion[®] and GDLs, etc. First possibility, inhomogeneous distribution of the reactants inside the fuel cell, can be induced by partially more-pressurized flow channels. According to Fig. 4.5 in [46], it can be found out that the stress distribution is actually inhomogeneous. There is higher compressive stress at the center part while the generated stress is weaker at the edge-

side. It means that the flow-channel at the center part might be excessively compressed, disturbing the reactants from flowing into. If it is the case, the mass transport loss can be found in the I-V curve in [46] at the lowest bending radius and, in real, there is a slight mass transport loss (The voltage and corresponding maximal power density drops a little as the fuel cell is bent the most). The effect of the mass transport here can be supported by comparing Fig. 4.5 (a) and (b). There is almost no difference of power densities at 0.5 V in [47] and this study while there is a difference in maximal power densities. Because the mass transport loss is visualized more clearly at high current density, it makes sense that the mass transport loss is more severe in maximal power densities than in power densities at 0.5 V. However, the power density in [47] is lower than that in this study in Fig. 4.5 (a). It means that the mass transport loss is higher in [47] considering that there is no other difference of experimental conditions between this study and [47]. Another possibility, damaged MEA by delamination between Nafion[®] and GDLs, might be the cause of the decrease in the charge transfer resistance. Although the Nafion[®] is a kind of polymers and has bendability and stretchability, the problem is a GDL. GDL can be bent but it has no stretchability. That is why there might be a delamination and it lowered the performance. Although nonflexible PEFCs could use hot-pressed MEA and show comparably high performance, it is because of the assembly pressure applied by some clamps. It is radically impossible in bendable PEFCs, meaning that the delamination between Nafion[®] and GDL could be critical to the performance. Accordingly, it can be found out that the performance variation of the flexible fuel cell was from not only the compressive stress on MEA but also the degree of bending. The compressive

stress and the degree of bending affect positively and negatively to the performance of the flexible fuel cell, respectively, although the compressive stress contributes more to the finalized performance.

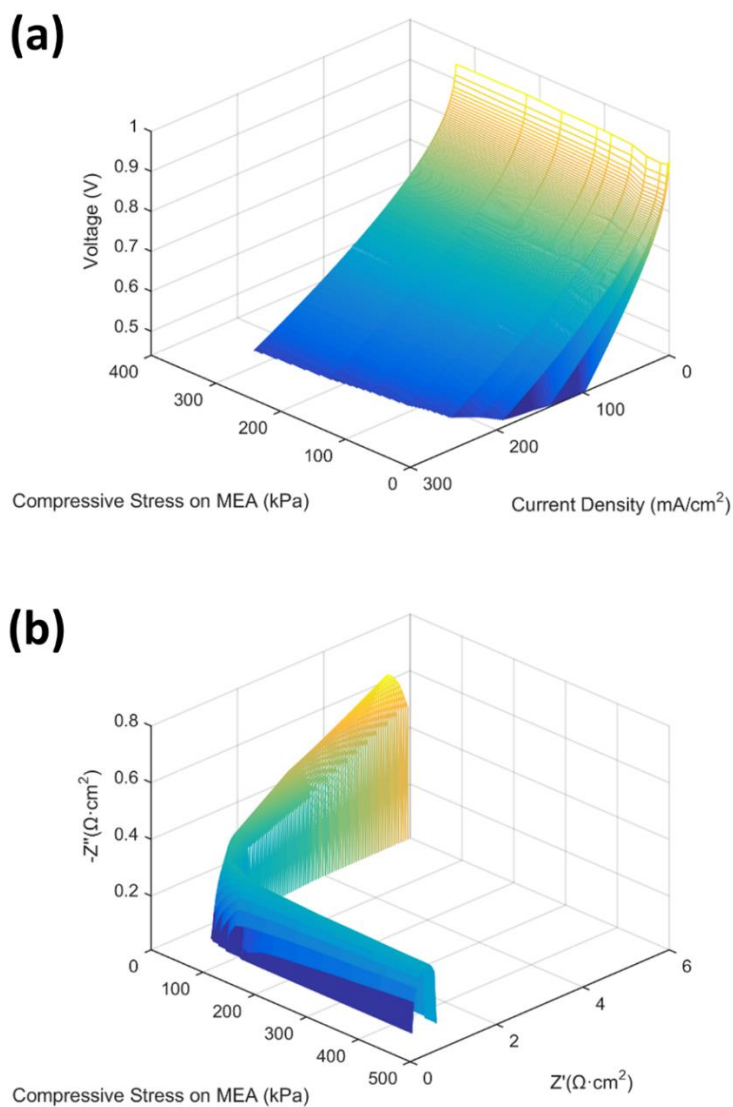


Fig. 4.6 3-dimensional mapping of (a) current-voltage-assembly pressure and (b) Z' - Z'' -assembly pressure of the flexible fuel cell.

In addition, from the I-V curves in Fig. 4.2, electrochemical kinetics parameters can be obtained. Ohmic resistances at each assembly pressure are already indicated in Figs. 4.3 and 4.4. In particular, I-V curves as well as the impedance spectra can be interpolated and mapped in 3-D map where the third axis is the assembly pressure (Fig. 4.6). It means that the performance of the flexible fuel cell can be estimated by using the data set in Fig. 4.6. It is expected that this map can be used as a reference data for further developed 3-d combined electrochemical and solid-mechanical model of the flexible fuel cell.

4.4 Conclusion

The flexible fuel cell was fabricated by using PDMS where Ag nanowire current collector was coated. Its performance was investigated at various precisely measured assembly pressures. The performance of the flexible fuel cell was increased with the increasing compressive stress. The maximal power density of the cell was exponentially increased as the assembly pressure was increased at the relatively low compressive stress range, but was increased slowly and somewhat linearly at the high compressive stress range. The maximal power density of the cell was 110 mW/cm^2 which is the highest power density among the flexible fuel cells based on this template. Through the impedance analysis, it was identified that the assembly pressure on MEA decreased both ohmic and charge transfer resistances. The performances and resistances measured in this study were compared with the previous researches [46,47]. It was also found that not only the assembly pressure but the degree of bending affect to the performance of the flexible fuel cell.

This research thus proved that the compressive stress onto MEA generated by bending actually increased the performance of the flexible fuel cell. In addition, it showed that the optimized flow-channel design especially for the flexible fuel cell is highly recommended in order to avoid the unknown loss of the performance from the inhomogeneous distribution of compressive stress generated by the bent shape of the fuel cell. It is also thought that ‘residual’ stress for the enhancement of the minimal power density of the flexible fuel cell is required because very low assembly pressure appreciably affects the performance. This will be the future work of this research.

Chapter 5. Flexible PEFC: Modeling and Validation

5.1 Introduction

The present study aims at developing a quantitative relationship between the performance of the flexible fuel cell and the assembly pressure generated by bending. In addition, the quantitative study enables to calculate the variation of the parameters of electrochemical kinetics such as transfer coefficient and exchange current density in Butler-Volmer equation with respect to assembly pressure. Using these parameters, this study proposes the modeling of the flexible fuel cell and validates the model by comparing the simulated results with several previously reported data [46,47] of the flexible fuel cell.

5.2 Model and Simulation

Normal PEFC can be described as a standard polarization model of the fuel cell [16,82]. The ideal (maximal voltage, E_{thermo}) of the fuel cell can be calculated from thermodynamics and activation (η_{act}), ohmic (η_{ohm}), and concentration (η_{conc}) losses are subtracted from the thermodynamic voltage. Although the reactive area of the fuel cell in this study is $3 \times 3 \text{ cm}^2$, which is larger than micro fuel cells, we described the fuel cell by 1-D model because the difference between the fuel cells with large and small reactive areas is the distribution of the reactants and this study supplied

abundant amount of the reactants so that there would be no mass transport loss. Accordingly, the fuel cell can be described as the following equations:

$$V = E_{thermo} - \eta_{act} - \eta_{ohm} - \eta_{conc} \quad (5.1)$$

The term, V , means the voltage of the fuel cell at specific current density (All the losses are the function of current density). In eq. (5.2.1) the concentration loss is actually not existing term because it is separated overvoltage from the activation loss and thermodynamic voltage of the cell. However, it was expressed as a separate term and will be ignored because there is no behavior of the mass transport loss at high current density range in Fig. 4.2. That is why the final equation estimating the flexible fuel cell in this study is expressed as follows:

$$V = E_{thermo} - \eta_{act} - \eta_{ohm} \quad (5.2)$$

Because the fuel cell was operated at room temperature and even the reactants applied in the fuel cell were all at room temperature and atmospheric pressure, we regarded the thermodynamic voltage as a constant. It was calculated by the equation, which is known as Nernst voltage:

$$E_{thermo} = E^0 - \frac{RT}{nF} \ln\left(\frac{1}{c_{H_2} c_{O_2}^{0.5}}\right) \quad (5.3)$$

The meaning of 0.5 on the concentration of oxygen is that every 0.5 out of 1 mol of hydrogen is reacted. In this equation, all the terms can be regarded as constants because they are independent of the current density. According to the table of standard electrode potentials in [10], the potential between the hydrogen and the oxygen is 1.229 V. R , T , n , and F used in this study are 8.314 J/mol·K, 298.15 K, 2, and 96485.34 C/mol. The concentrations of hydrogen and oxygen are 1 and 0.21, respectively. The E_{thermo} calculated by using these constants is 1.219 V.

The activation loss, η_{act} , can be divided into anodic and cathodic parts. The activation of the reaction in electrochemistry is known to follow Butler-Volmer equation. Because there are two interfaces in the fuel cell (anode and cathode), the activation loss is divided into two equations as follows:

$$j + j_{\text{leak}} = j_{0,\text{anode}} \left\{ \exp\left(\frac{\alpha_{\text{anode}} n F \eta_{\text{anode}}}{RT}\right) - \exp\left(\frac{-(1 - \alpha_{\text{anode}}) n F \eta_{\text{anode}}}{RT}\right) \right\} \quad (5.4)$$

$$j + j_{\text{leak}} = j_{0,\text{cathode}} \left\{ \exp\left(\frac{\alpha_{\text{cathode}} n F \eta_{\text{cathode}}}{RT}\right) - \exp\left(\frac{-(1 - \alpha_{\text{cathode}}) n F \eta_{\text{cathode}}}{RT}\right) \right\} \quad (5.5)$$

However, only the cathodic activation loss is considered here because the anodic activation loss is too small compared to the cathodic activation loss so that it is ignorable as two activation losses are considered together. According to these two equations, the voltage losses cannot be expressed explicitly by other terms. This study therefore calculated the losses numerically. In the activation losses, transfer

coefficients and exchange current density can be regarded as the variables with respect to the assembly pressure. It is because the other parameters such as n , F , R , and T are already fixed by its surroundings and independent of the assembly pressure. These parameters are same as in the calculation of the thermodynamic potential.

The conductivity of the electrolyte membrane in PEFCs is the function of thickness, humidity and temperature. The ohmic resistance is constant in all current density range so that the total ohmic loss can be expressed as follows:

$$\eta_{ohm} = j(ASR) \quad (5.6)$$

The area-specific resistance (ASR) can be expressed as:

$$ASR = \frac{t_{electrolyte}}{\sigma} \quad (5.7)$$

In this equation, it is noticed that the ohmic resistance is proportional to the thickness of the electrolyte. The conductivity (σ) was measured experimentally with respect to the water content within the electrolyte and the temperature. It was mathematically fitted and final equation was obtained as the followings:

$$\sigma = (0.005193\lambda - 0.00326) \exp \left\{ 1268 \left(\frac{1}{303} - \frac{1}{T} \right) \right\} \quad (5.8)$$

This is empirical equation; thus each unit was ignored. The water content was also expressed as the function of relative humidity as follows:

$$\lambda = 0.0043 + 17.81H_r - 39.85H_r^2 + 36H_r \quad (5.8)$$

All the parameters used in the equations above are indicated in Table 5.1.

Parameters	Value	unit
E^0	1.229	V
R	8.314	J/molK
T	298.15	K
n	2	
F	96485.34	C/mol
H_r	0.5	
$t_{\text{electrolyte}}$	50	μm
c_{H_2}	1	atm
c_{O_2}	0.21	atm
j_{leak}	0.01	A/cm ²

Table 5.1 Parameters and values used in the model of the PEFC.

The variables, *i.e.* an exchange current density, charge transfer coefficient, were obtained as follows. Ohmic loss is first subtracted from each I-V curves in Fig. 4.2 and Tafel method is used to extract transfer coefficient and exchange current density from the slope and intersection, respectively. Figure 5.2 shows the obtained transfer coefficient and exchange current density. The transfer coefficient decreases exponentially while the exchange current density increases with the increasing assembly pressure. Specifically, transfer coefficient asymptotes at 0.1 but the converging value of the exchange current density cannot be estimated from this data.

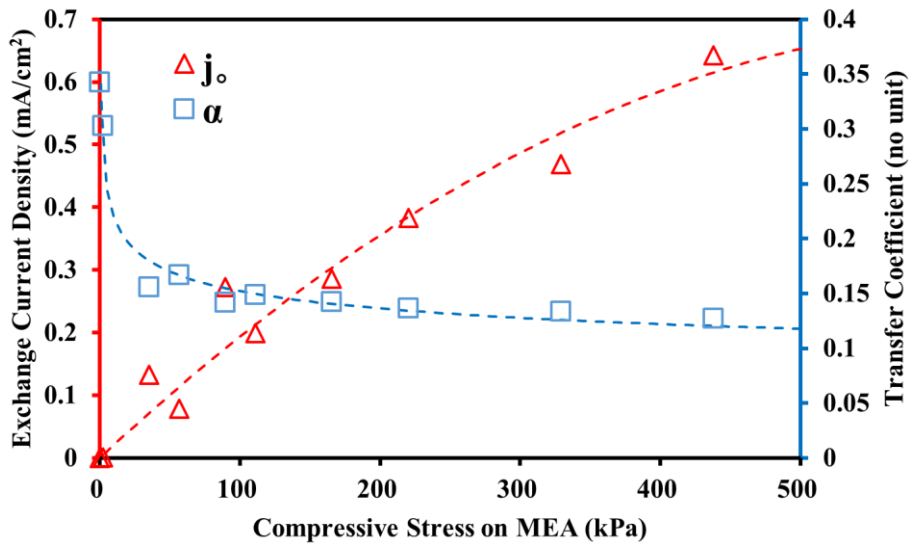


Fig. 5.1 The variations of an exchange current density and a charge transfer coefficient in the flexible fuel cell with respect to the variation of compressive stress.

α_{cathode} , $j_{0,\text{cathode}}$, and ASR are the variables with respect to the assembly pressure. The variations of such variables were fitted into the equation. Excel software was used to fit the data into the equation. The fitted curves for the exchange current density and transfer coefficient are indicated in Fig. 5.1. The fitted equations for α_{cathode} , $j_{0,\text{cathode}}$, and ASR are as follows:

$$j_{0,\text{cathode}} = -1.575 \cdot 10^{-9} p^2 + 2.0937 \cdot 10^{-6} p \quad (5.10)$$

$$\alpha_{\text{cathode}} = 0.3165 p^{-0.159} \quad (5.11)$$

$$ASR = 2.6216 p^{-0.227} \quad (5.12)$$

Like the equation of the conductivity of the electrolyte, the above equations are empirical equation so that the unit of each parameter should be fixed. The units of all parameters are indicated in Nomenclature.

5.3 Validation

Since the variations of the transfer coefficient, exchange current density, and ohmic resistance (Fig. 4.4 (b)) are known, it is possible to build up the electrochemical simulation model with the application of the assembly pressure by following the described eqs. (5.1) to (5.12). as described above, diffusion coefficient which is generally included in normal PEFC model does not have to be considered in our model because there is no behavior of mass transport in the region of high current density in I-V curves in Fig. 4.2.

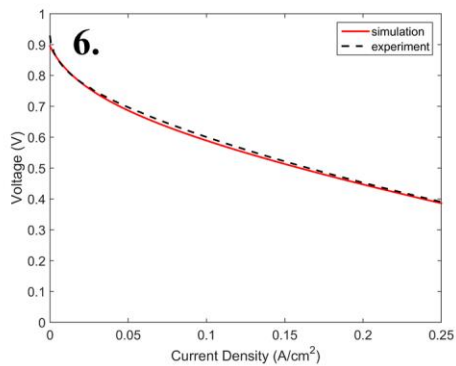
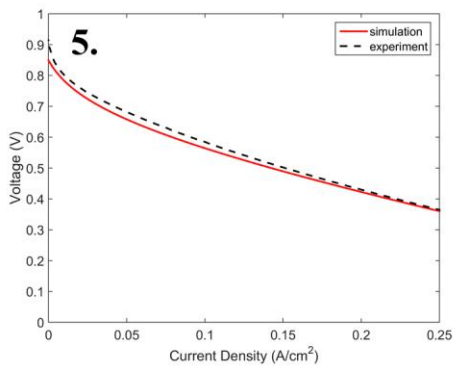
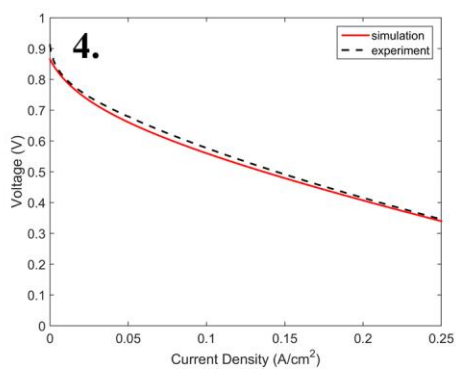
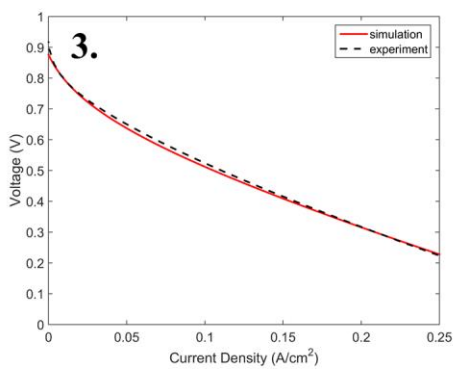
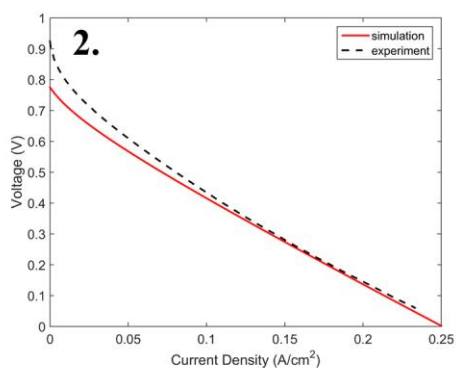
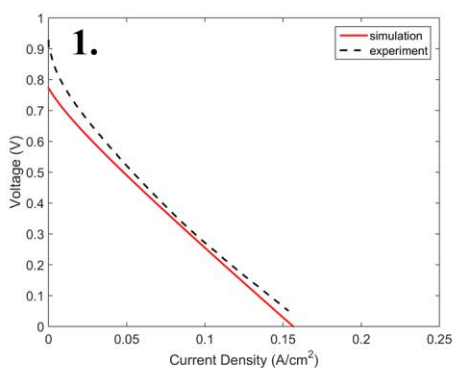


Fig. 5.2 (Continued next)

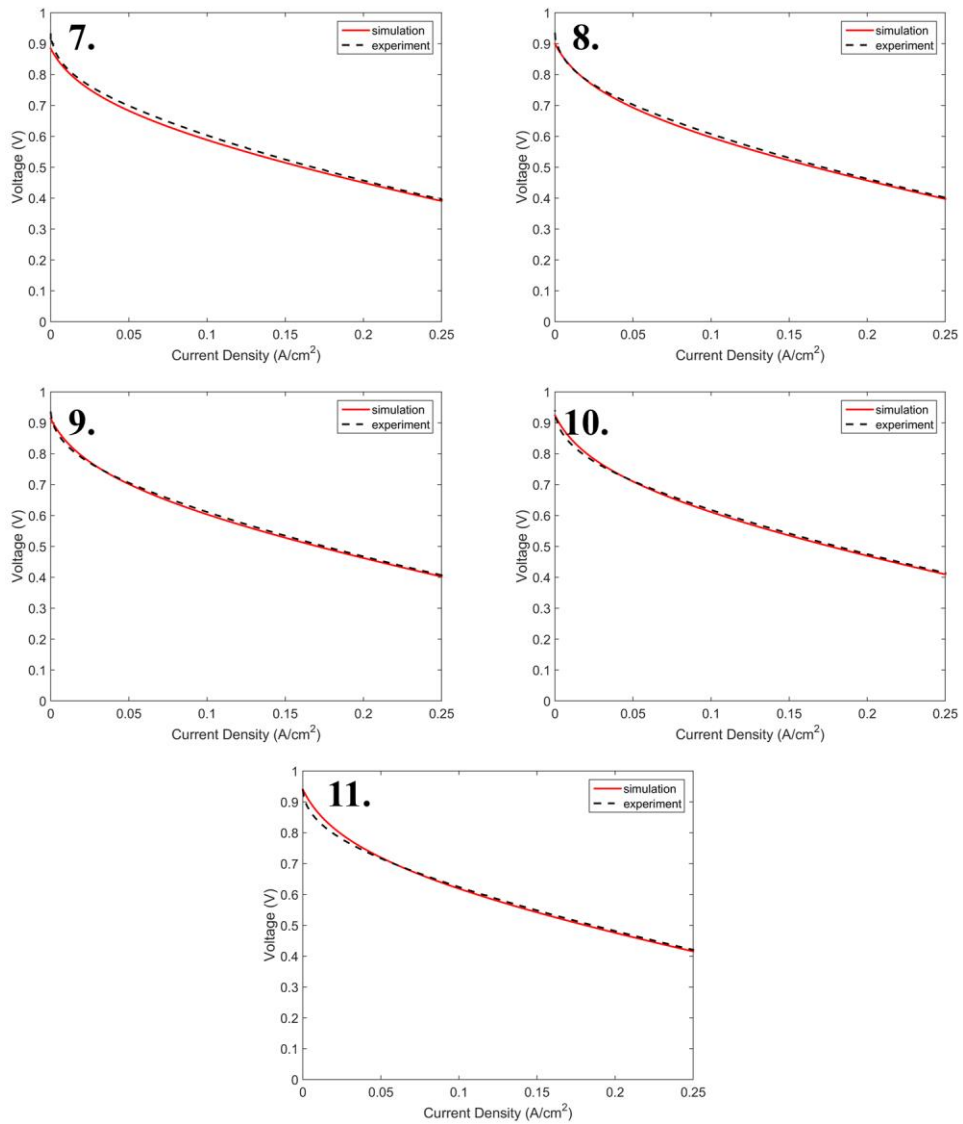


Fig. 5.2 (Continued) Comparison of the simulation and experimental I-V curves of the flexible fuel cell. The experimental data here is same as the I-V curves in Fig. 4.2. The numbers marked in the figure indicate the assembly pressure in Table 4.1.

Fig. 5.2 shows the results of the I-V curves calculated from the model and comparison with the experimental results. All the results show less than 5 % of error (voltages at each point were compared and averaged). Interestingly, the error increases with the assembly pressure increasing. It is thought that this tendency is due to the high deviation of the lower assembly pressure. For this reason, the deviations of the transfer coefficient and the exchange current density in Fig. 5.2 are high at lower stress region. When it comes to the data in [46] and [47], the experimental data was also compared with the simulated results in Fig. 5.3 and 5.4, respectively. The previous study was about the flexible fuel cell with same template (PDMS flow-field plates coated with Ag nanowires). Here, it was shown that even higher performance could be achieved by asymmetrically offsetting the MEA from the midline of the fuel cell assembly, where the FEM model predicted higher assembly pressure under bending (See Fig. 3.1.5) [47]. Here, it is also similar that the error between the experimental and simulation data is higher at low assembly pressure. Other interesting characteristic is that the difference between simulated and experimental data is generally higher in Fig. 5.3 than 5.4. It is speculated that the reason for this phenomenon resulted from the variation of the shape by bending. As mentioned above, for the flexible fuel cell to generate same intensity of the compressive stress by bending, the fuel cell characterized in Fig. 5.3 had to be bent more than that in Fig. 5.4. Accordingly, if there was another factor of the performance loss such as aforementioned inhomogeneous stress distribution, there should be an error between experimental and simulation data (In the simulation model, only basic ohmic and charge transfer resistances with the variation of key parameters were considered.). It

corresponds with the behaviors in Fig. 5.3 and 5.4 that the voltages of the experimental data at high current density are all slightly lower than the simulation data, which is almost not the case in Fig. 5.2.

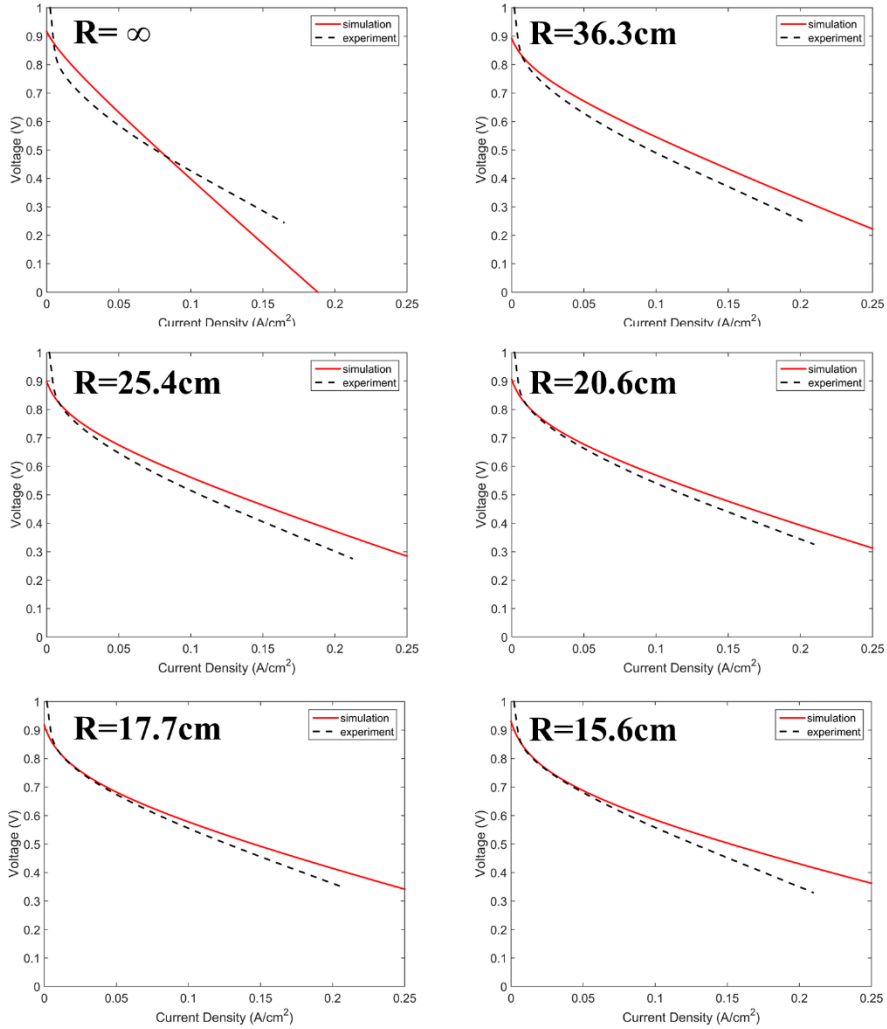


Fig. 5.3 Comparison of the simulation and experimental I-V curves of the flexible fuel cell in [46]. The numbers (1, 2, 3, 4, 5, and 6) in the figures indicate the bending radius of infinite (flat), 36.3, 25.4, 20.6, 17.7, and 15.6 cm, respectively.

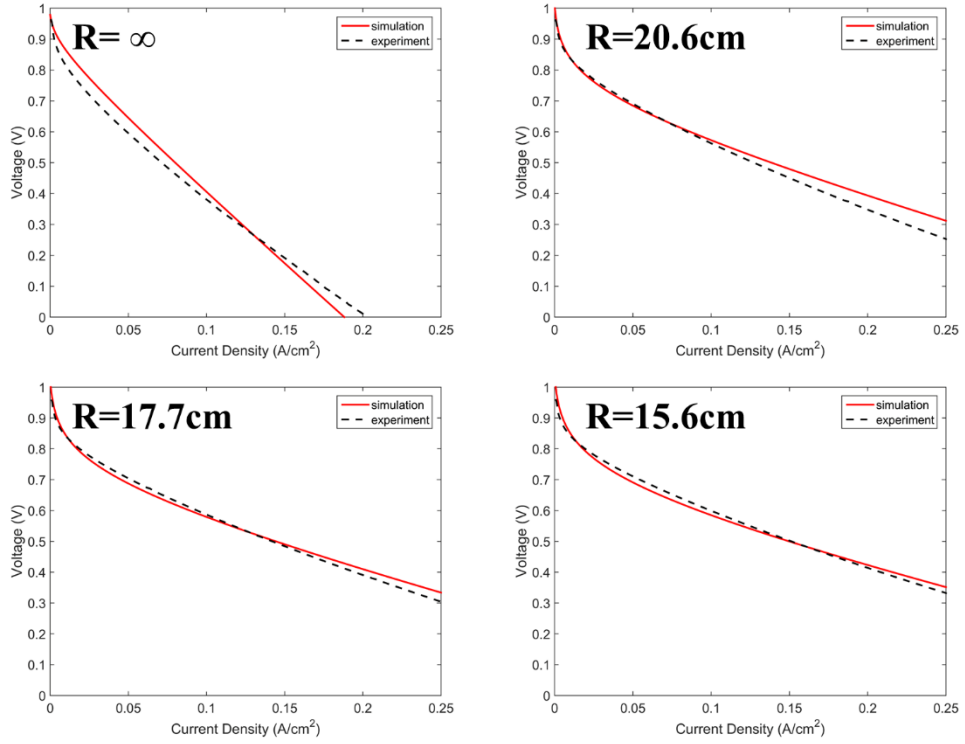


Fig. 5.4 Comparison of the simulation and experimental I-V curves of the flexible fuel cell in [47]. The numbers (1, 2, 3, and 4) in the figures indicate the bending radius of infinite (flat), 20.6, 17.7, and 15.6 cm, respectively.

Here, it should be noted that the transfer coefficient of 0.1 means that the flexible fuel cell here seems not easy to improve the maximal performance higher than measured here as long as this structure and the materials of the components are maintained. Butler-Volmer equation in representative form is described as follows;

$$j = j_0 \left\{ \exp \left(\frac{\alpha n F \eta_{act}}{RT} \right) - \exp \left(\frac{-(1-\alpha) n F \eta_{act}}{RT} \right) \right\} \quad (5.13)$$

According to eq. (5.13), the transfer coefficient is located in exponential term while j_0 in polynomial term. It means that transfer coefficient affects the current density dominantly. However, many literature show the transfer coefficient between 0.2 and 0.5 [16]. The value here is quite lower (0.1 vs. 0.2-0.5). Considering that transfer coefficient is included in exponential term, the resulting current density and related performance of the fuel cell would be highly limited. Although the exchange current density shows the opposite variation, *i.e.* increasing tendency with increasing assembly pressure, it cannot compensate the loss induced from the transfer coefficient. Even if the exchange current density seems still increasing, it increases logarithmically. It means that the compensated performance from the increased exchange current density cannot catch up with the loss from the transfer coefficient.

An exchange current density (j_0) is expressed as follows:

$$j_0 = \left(\frac{A'}{A}\right) n F c_R^* f_1 \exp\left(\frac{-\Delta G}{RT}\right) \quad (5.14)$$

where A' , A , c_R^* , f_1 , and ΔG represent an effective reaction area, projective reaction area, the concentration of the reactant near an electrode, the decay rate to a product, and an activation barrier. In the increasing assembly pressure of the flexible fuel cell, the components and structure were kept same: only assembly pressure was controlled. It means that the activation barrier and temperature were kept constant. The decay rate to a product was therewith kept same because it can be expressed as the function of temperature. The concentrations of the reactant, *i.e.* hydrogen or

oxygen in this study, would rather decrease since the reactants would be consumed in the electrochemical reaction more actively in the higher current (= higher power). However, the performance was actually increased with increasing assembly pressure. From this point of view, only one variable inside eq. (5.2) remains: effective reaction area. It is believed that the assembly pressure might affect the effective reaction area. It has been proposed in many literatures that the assembly pressure affects the number of TPB [73–78]. This relation corresponds to the result that the transfer coefficient is eventually related to the catalyst including effective reaction area. Consequently, this parametric study clearly shows that there should be residual compression on the MEA to make the fuel cell give serviceable power unless a specially designed MEA generating high power without the pressure is developed and adopted in the flexible fuel cell.

It is clear from the model that neither of the ohmic and charge transfer resistance is dominant for the performance loss of the flexible fuel cell. However, the charge transfer resistance is composed of two main parameters: a transfer coefficient and an exchange current density. As indicated in Fig. 5.1, the j_0 increases while α decreases as the compressive stress onto MEA increases. In this case, it is required to investigate which parameter affects dominantly on the charge transfer resistance. In addition, the mass transport effect on the charge transfer resistance should also be considered. Here, in order to check such contribution to the total performance by the charge transfer resistance, this resistance was also calculated from the simulation model described above. Although the activation loss was calculated from eq. (5.13), this form is only for the case that the concentrations of the reactants are negligible.

Here, if it is desired to investigate the effect of mass transport, eq. (5.13) can be described as follows:

$$j = j_0 \left\{ \frac{c^*}{c^0} \exp \left(\frac{\alpha n F \eta_{act}}{RT} \right) - \exp \left(\frac{-(1-\alpha) n F \eta_{act}}{RT} \right) \right\} \quad (5.14)$$

where c^* and c^0 represent bulk concentration and the concentration near the reaction surface, respectively. From the differential form of eq. (5.14), the equation of the charge transfer resistance can be described as follows:

$$R_{ct} = \frac{\frac{1}{j_0} + \frac{\delta}{n F D c^0} \exp \left(\frac{\alpha n F \eta_{act}}{RT} \right)}{\left\{ \left(1 - \frac{j \delta}{n F D c^0} \right) \alpha \exp \left(\frac{\alpha n F \eta_{act}}{RT} \right) + (1-\alpha) \exp \left(\frac{-(1-\alpha) n F \eta_{act}}{RT} \right) \right\} \frac{n F}{RT}} \quad (5.15)$$

If the limiting current density, *i.e.* $j_L = \frac{n F D c^0}{\delta}$, is substituted into the eq. (5.15), the eq. (5.15) is simplified as:

$$R_{ct} = \frac{\frac{1}{j_0} + \frac{1}{j_L} \exp \left(\frac{\alpha n F \eta_{act}}{RT} \right)}{\left\{ \left(1 - \frac{j}{j_L} \right) \alpha \exp \left(\frac{\alpha n F \eta_{act}}{RT} \right) + (1-\alpha) \exp \left(\frac{-(1-\alpha) n F \eta_{act}}{RT} \right) \right\} \frac{n F}{RT}} \quad (5.16)$$

According to eq. (5.16), the charge transfer resistance can be calculated and the sensitivities by α and j^0 can be visualized.

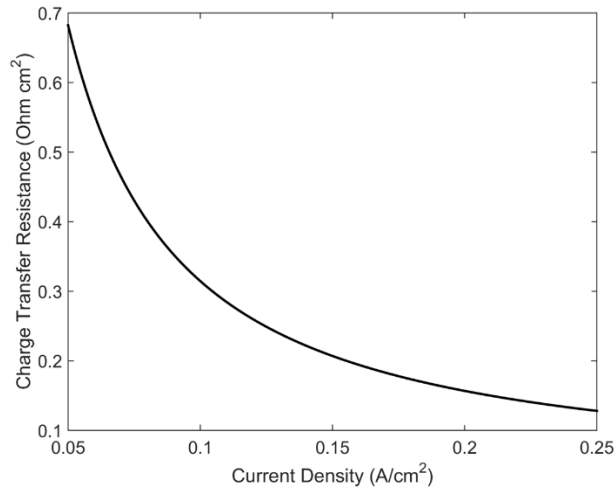


Fig. 5.5 The calculated charge transfer resistance of the I-V curve of the flexible fuel cell in Fig. 5.2, legend number 11 at 0.5 V.

Before investigating the sensitivities by α and j_0 , it was validated by calculating the charge transfer resistance in the case of Fig. 5.2, legend number 11 at 0.5 V. It is established clearly that a charge transfer resistance decreases with the increasing current density. Even it can be found in eq (5.14) that the forward reaction term in the differential expression is gradually decreased with the increasing current density. According to Fig. 5.6 (a), the charge transfer resistance is significantly affected by α by 8-fold of the minimal value at $\alpha = 0.9$. Although the transfer coefficient is known to have between 0.2-0.5, the charge transfer resistance can be doubled, meaning that α is significant factor of the performance in the flexible fuel cell. However, as shown in Fig. 5.6 (b), the situation is reversed as the concentration of the reactant is near the limiting current density. The charge transfer resistance arises up to $20 \Omega \cdot \text{cm}^2$ means that the fuel cell does not operate. In other words, in the

condition of abundant reactant, the charge transfer coefficient is the main factor for the performance of the fuel cell, while it is not as the reactant close to limiting current density is supplied to the fuel cell.

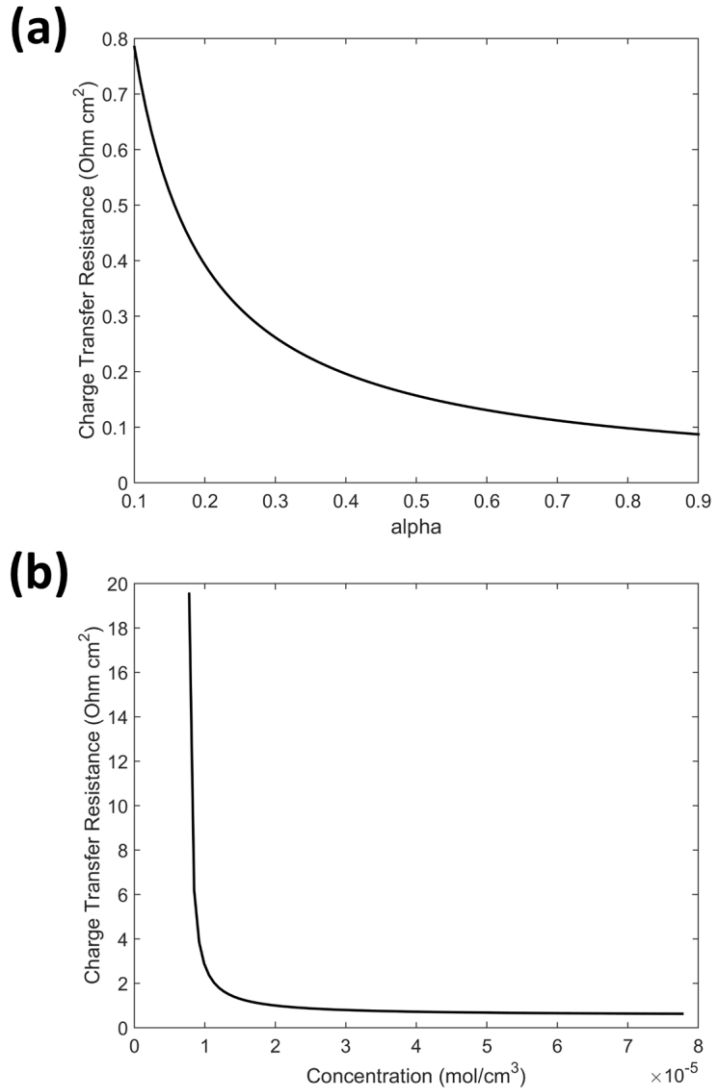


Fig. 5.6 The variations of charge transfer resistance with respect to (a) charge transfer coefficient and (b) concentration of hydrogen. The corresponding I-V model is from Fig. 5.2, legend number 11.

5.4 Conclusion

This chapter proposes the simulation model for the flexible fuel cell. Because quantitative relation between the assembly pressure and resulting I-V of the flexible fuel cell were investigated in Ch. 4, it has been possible to estimate the engineering parameters, *i.e.* an exchange current density and transfer coefficient. The parameters were used in the standard polarization model of the fuel cell. As a result, the predicted I-V behavior showed good coincidence with the experimental data in Ch. 4. In order to validate this model, another predicted I-V curves by following the same experimental conditions as [46] (Ch. 3) and [47] were compared with the real I-V curves in the experiment. It also showed good coincidence with each other. It means that it is possible to estimate the performance of the flexible fuel cell based on the template suggested here by using the electrochemical data and the fuel cell model here. In addition, from the sensitivity analysis, it was visualized that the performance of the flexible fuel cell depends mainly on a charge transfer resistance while it does not as the reactant of the amount close to limiting current density is supplied.

Chapter 6. Conclusion and Future Work

6.1 Conclusion

This research demonstrated flexible and thus bendable PEFCs. The purpose of realizing the flexible PEFC is to cope with the future demand for the high energy density in the applications such as flexible and epidermal electronics. Its flow-field plates were fabricated by using PDMS coated with Ag nanowire current collectors. The flexible fuel cell was tested as it was under three different loads: bending, twisting, and mixed bending & twisting.

The flexible fuel cell was first characterized as it was bent. The performance was increased as it was bent. The peak power density was increased from 43 to 71 mW/cm². The total reactive area was 9 cm², thus total absolute power of 639 mW was measured from the flexible fuel cell here. It was found from EIS that the decreased ohmic and charge transfer resistances led to the performance enhancement. If the performance of the flexible fuel cell was increased without the change of its components, it could be thought that the only one change, *i.e.* the deformation by bending, would increase the performance by bending. By using solid-mechanical FEM, it was identified that the assembly pressure (compressive stress) onto MEA was increased by bending. It was hypothesized that this compressive stress may significantly increase the performance of the flexible fuel cell. The flexible fuel cell also powered and operated successfully the small fan, meaning that the technological

level of this fuel cell can be directly used for real small (portable) applications.

Second test for the flexible fuel cell is to characterize it under twisting load. It is because not only bending but also twisting load is applied to the flexible electronics in real environment. As a result, the twisting load lowered the performance of the flexible fuel cell, which is reverse tendency of bending test. Stress distribution inside the fuel cell was also analyzed by using FEM again here but there was no significant change of the stress to the MEA. However, it was found that the performance of the fuel cell was permanently degraded before measuring the performance. It means that some components of the fuel cell were damaged permanently. The power density was decreased from 16 to 10 mW/cm², which is lower than one-fourth of the power density of the bending test as the fuel cell was in flat shape. It is thought that the decrease of the performance was induced from the damaged MEA. It was identified that the GDLs at both sides of the MEA were detached. Because the flexible fuel cell cannot pressurize the MEA like the normal PEFC, it is very important for the GDLs to be attached uniformly with the electrolyte membrane. However, twisting generates the strain so that the unstretchable GDL was detached from the electrolyte membrane (bending did not generate the strain at the neutral plane where the MEA was located). In this case, the TPB could be decreased and it was visualized in EIS results that both ohmic and charge transfer resistances were lowered by twisting.

The final flexibility test was implemented by applying both bending and twisting loads simultaneously to the flexible fuel cell. The real environment for the use of flexible electronics will be under mixed bending and twisting in various shapes.

The performance of the fuel cell was measured under the twisting angle from 0 to 25° with the bending component of $R = \infty$ (flat shape) to 36.3 cm. The result showed that the tendency of the decrease in the performance was same as the previous ‘only’ twisting test, while the performance at each twisting angle was increased. Using the same boundary conditions as in twisting test, the stress distribution inside the fuel cell was calculated. It was found that the assembly pressure generated by twisting was not dominant compared to that by bending. In addition, the twisting and bending components seems independently to generate the assembly pressure. That is why the I-V curves of the fuel cell under mixed bending and twisting loads were higher in general than under only twisting. In this experiment, the effect by the damaged MEA was visualized in EIS data that the charge transfer resistance rather decreases with the increasing twisting angle, which seems the detrimental effect by the twisting was compensated by the positive effect from the bending and corresponding generated assembly pressure.

The increase of the performance in the fuel cell was actually explained by the indirect way (calculation using FEM). Thus it was experimentally reenacted by characterizing the flexible fuel cell under various precisely controlled assembly pressure. As expected and hypothesized, the result showed that the performance of the fuel cell was increased as the assembly pressure was increased. Here, the electrochemical parameters were extracted from the polarization curves and those are fitted to the curve with respect to the assembly pressure. By using a standard polarization model of the fuel cell, it becomes able to predict the performance of the flexible fuel cell at specific stress distribution. The stress distribution can be estimated

as shown in this study. It means that the performance of the flexible fuel cell can be predicted through the model developed here.

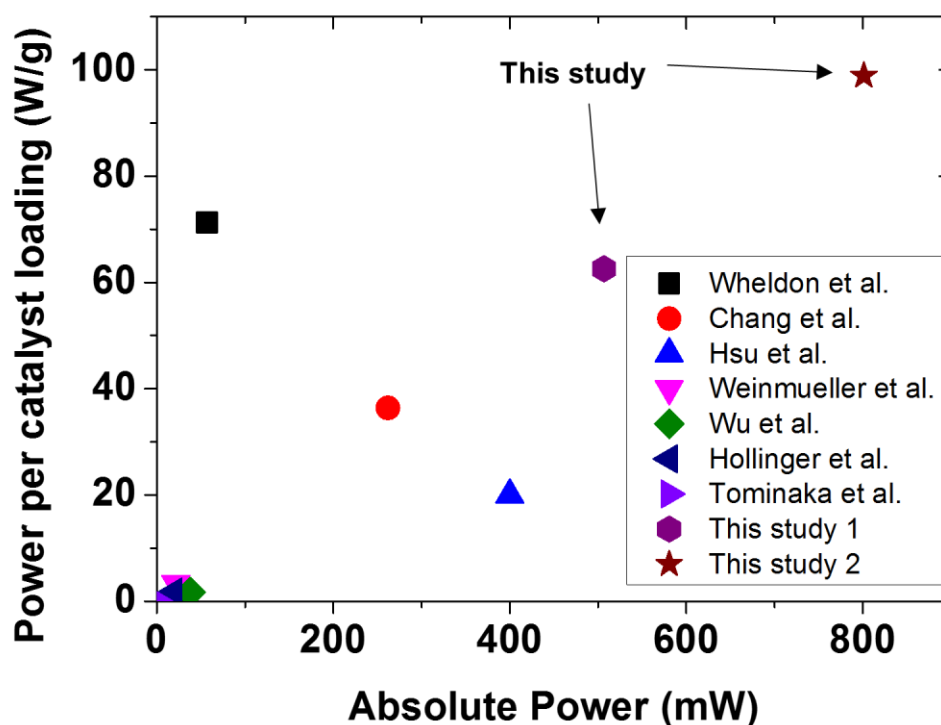


Fig. 6.1 Comparisons of (a) the power densities divided by their amount of catalyst and (b) the absolute powers measured from the flexible fuel cells including the research here [27–34,46,47].

This study thus showed that the flexible, thus bendable and twistable fuel cell can be realized. Even the performance level of the flexible fuel cell is up to the level of the power sources for real applications. As shown in Fig. 6.1, these power densities with respect to both the loading of catalyst and absolute scale are all higher than the previous studies about flexible fuel cells in the literature. The performance of the flexible fuel cell depends on the shape of the fuel cell, but this performance can be predicted by the simulation model developed here, meaning the flexible fuel cell can now be engineered for various applications.

6.2 Future Work

This study showed that the performance of the fuel cell is enough to power real applications. However, the performance is actually instable, depending on its shape and corresponding stress conditions. It can be coped with through engineering the fuel cell for each specific condition but it is desired to develop the fuel cell with a stable power regardless of its shape. This type of flexible fuel cells with a reliable power is believed to open up the broader applications of the flexible fuel cell. One example of developing the flexible fuel cell with reliable performance is to design it holding residual compressive stress. Another way will be to use micro-components generating an attractive force such as magnets.

In addition, although Ag nanowire has good corrosion resistance and high electric conductivity, the price will be not that cheap in mass-production scheme due to its bulk material price. For a cost-effectiveness, investigating another flexible and stretchable current collector may be other interesting future work. Likewise, this study employed PDMS as the material for the main body but other materials should be found out in order to improve the flexibility and performance of the flexible fuel cell. One of the candidate is a polymer films imprinted with the flow channels.

Bibliography

- [1] D.-H. Kim, N. Lu, R. Ma, Y.-S. Kim, R.-H. Kim, S. Wang, et al., Epidermal electronics, *Science* (80-.). 333 (2011) 838–843.
doi:10.1126/science.1206157.
- [2] J.J. Boland, Flexible electronics: Within touch of artificial skin., *Nat. Mater.* 9 (2010) 790–792. doi:10.1038/nmat2861.
- [3] D.-H. Kim, R. Ghaffari, N. Lu, J. a. Rogers, Flexible and Stretchable Electronics for Biointegrated Devices, *Annu. Rev. Biomed. Eng.* 14 (2012) 113–128. doi:10.1146/annurev-bioeng-071811-150018.
- [4] A. Russo, B.Y. Ahn, J.J. Adams, E.B. Duoss, J.T. Bernhard, J.A. Lewis, Pen-on-paper flexible electronics, *Adv. Mater.* 23 (2011) 3426–3430.
doi:10.1002/adma.201101328.
- [5] Q. Cao, H. Kim, N. Pimparkar, J.P. Kulkarni, C. Wang, M. Shim, et al., Medium-scale carbon nanotube thin-film integrated circuits on flexible plastic substrates., *Nature.* 454 (2008) 495–500. doi:10.1038/nature07110.
- [6] I. Yagi, N. Hirai, Y. Miyamoto, M. Noda, A. Imaoka, N. Yoneya, et al., A flexible full-color AMOLED display driven by OTFTs, *J. Soc. Inf. Disp.* 16 (2008) 15. doi:10.1889/1.2835023.
- [7] Y.H. Kwon, S.W. Woo, H.R. Jung, H.K. Yu, K. Kim, B.H. Oh, et al., Cable-type flexible lithium ion battery based on hollow multi-helix electrodes, *Adv. Mater.* 24 (2012) 5192–5197. doi:10.1002/adma.201202196.
- [8] E.H. Kil, K.H. Choi, H.J. Ha, S. Xu, J.A. Rogers, M.R. Kim, et al.,

- Imprintable, bendable, and shape-conformable polymer electrolytes for versatile-shaped lithium-ion batteries, *Adv. Mater.* 25 (2013) 1395–1400. doi:10.1002/adma.201204182.
- [9] M. Koo, K. Il Park, S.H. Lee, M. Suh, D.Y. Jeon, J.W. Choi, et al., Bendable inorganic thin-film battery for fully flexible electronic systems, *Nano Lett.* 12 (2012) 4810–4816. doi:10.1021/nl302254v.
- [10] A.J. Bard, L.R. Faulkner, *Electrochemical Methods: Fundamentals and Applications*, 2nd ed., John Wiley & Sons, Hoboken, 2001.
- [11] A.G. Castiglioni, M.B. Bigdeli, C. Palamini, D. Martinoia, L. Frezza, B. Matassini, et al., Spaceship Earth. Space-driven technologies and systems for sustainability on ground, *Acta Astronaut.* 115 (2015) 195–205. doi:10.1016/j.actaastro.2015.05.029.
- [12] L. Piper, S. Rajakaruna, Comparison of performance of diesel and fuel cell based submarine power supplies, *Sustain. Energy Technol.* (2010) 1–6. doi:10.1109/ICSET.2010.5684460.
- [13] M. Romer, G.H. Miley, N. Luo, R.J. Gimlin, Ragone Plot Comparison of Radioisotope Cells and the Direct Sodium Borohydride/Hydrogen Peroxide Fuel Cell With Chemical Batteries, *IEEE Trans. Energy Convers.* 23 (2008) 171–178. doi:10.1109/TEC.2007.914159.
- [14] T. Christen, M.W. Carlen, Theory of Ragone plots, *J. Power Sources.* 91 (2000) 210–216. doi:10.1016/S0378-7753(00)00474-2.
- [15] M. Winter, R.J. Brodd, What Are Batteries, Fuel Cells, and Supercapacitors?, *Chem. Rev.* 104 (2004) 4245–4270.

doi:10.1021/cr020730k.

- [16] R. O'Hayre, S.-W. Cha, W. Colella, F.B. Prinz, *Fuel Cell Fundamentals*, 2nd ed., John Wiley & Sons, New York, 2009.
- [17] S.K. Kamarudin, F. Achmad, W.R.W. Daud, Overview on the application of direct methanol fuel cell (DMFC) for portable electronic devices, *Int. J. Hydrogen Energy*. 34 (2009) 6902–6916.
doi:10.1016/j.ijhydene.2009.06.013.
- [18] K. Cowey, K.J. Green, G.O. Mepsted, R. Reeve, Portable and military fuel cells, *Curr. Opin. Solid State Mater. Sci.* 8 (2004) 367–371.
doi:10.1016/j.cossms.2004.12.004.
- [19] C.K. Dyer, Fuel cells for portable applications, *J. Power Sources*. 106 (2002) 31–34. doi:10.1016/S0378-7753(01)01069-2.
- [20] J.H. Wee, Which type of fuel cell is more competitive for portable application: Direct methanol fuel cells or direct borohydride fuel cells?, *J. Power Sources*. 161 (2006) 1–10. doi:10.1016/j.jpowsour.2006.07.032.
- [21] C.A. Cottrell, S.E. Grasman, M. Thomas, K.B. Martin, J.W. Sheffield, Strategies for stationary and portable fuel cell markets, *Int. J. Hydrogen Energy*. 36 (2011) 7969–7975. doi:10.1016/j.ijhydene.2011.01.056.
- [22] R. O'Hayre, D. Braithwaite, W. Hermann, S.J. Lee, T. Fabian, S.W. Cha, et al., Development of portable fuel cell arrays with printed-circuit technology, *J. Power Sources*. 124 (2003) 459–472. doi:10.1016/S0378-7753(03)00802-4.
- [23] P. Agnolucci, Economics and market prospects of portable fuel cells, *Int. J.*

- Hydrogen Energy. 32 (2007) 4319–4328.
doi:10.1016/j.ijhydene.2007.03.042.
- [24] T. Henriques, B. C??sar, P.J.C. Branco, Increasing the efficiency of a portable PEM fuel cell by altering the cathode channel geometry: A numerical and experimental study, *Appl. Energy*. 87 (2010) 1400–1409.
doi:10.1016/j.apenergy.2009.09.001.
- [25] S.H. Kim, H.Y. Cha, C.M. Miesse, J.H. Jang, Y.S. Oh, S.W. Cha, Air-breathing miniature planar stack using the flexible printed circuit board as a current collector, *Int. J. Hydrogen Energy*. 34 (2009) 459–466.
doi:10.1016/j.ijhydene.2008.09.088.
- [26] <http://www.treehugger.com/gadgets/panasonics-new-micro-fuel-cell-for-portable-electronics.html> http://hfcletter.com/issues/XIX_7/stories/144-1.html <http://www.myfcpower.com/> www.myfcpower.com/
www.nectarpower.com www.horizonfuelcell.com <http://inhabitat.c>, (n.d.).
- [27] J. Wheldon, W.-J. Lee, D.-H. Lim, A.B. Broste, M. Bollinger, W.H. Smyrl, High-Performance Flexible Miniature Fuel Cell, *Electrochem. Solid-State Lett.* 12 (2009) B86. doi:10.1149/1.3095682.
- [28] S. Tominaka, H. Nishizeko, J. Mizuno, T. Osaka, Bendable fuel cells: on-chip fuel cell on a flexible polymer substrate, *Energy Environ. Sci.* 2 (2009) 1074. doi:10.1039/b915389f.
- [29] S. Tominaka, H. Nishizeko, S. Ohta, T. Osaka, On-chip fuel cells for safe and high-power operation: investigation of alcohol fuel solutions, *Energy Environ. Sci.* 2 (2009) 849–852. doi:10.1039/b906216e.

- [30] F.-K. Hsu, M.-S. Lee, C.-C. Lin, Y.-K. Lin, W.-T. Hsu, A flexible portable proton exchange membrane fuel cell, *J. Power Sources*. 219 (2012) 180–187. doi:10.1016/j.jpowsour.2012.07.054.
- [31] C. Weinmueller, G. Tautschnig, N. Hotz, D. Poulikakos, A flexible direct methanol micro-fuel cell based on a metalized, photosensitive polymer film, *J. Power Sources*. 195 (2010) 3849–3857. doi:10.1016/j.jpowsour.2009.12.092.
- [32] I. Chang, M.H. Lee, J.-H. Lee, Y.-S. Kim, S.W. Cha, Air-breathing flexible Polydimethylsiloxane (PDMS)-based fuel cell, *Int. J. Precis. Eng. Manuf.* 14 (2013) 501–504. doi:10.1007/s12541-013-0067-1.
- [33] R. Hahn, S. Wagner, A. Schmitz, H. Reichl, Development of a planar micro fuel cell with thin film and micro patterning technologies, *J. Power Sources*. 131 (2004) 73–78. doi:10.1016/j.jpowsour.2004.01.015.
- [34] A.S. Hollinger, P.J.A. Kenis, Manufacturing all-polymer laminar flow-based fuel cells, *J. Power Sources*. 240 (2013) 486–493. doi:10.1016/j.jpowsour.2013.04.053.
- [35] R.A. Antunes, M.C.L. De Oliveira, G. Ett, V. Ett, Carbon materials in composite bipolar plates for polymer electrolyte membrane fuel cells: A review of the main challenges to improve electrical performance, *J. Power Sources*. 196 (2011) 2945–2961. doi:10.1016/j.jpowsour.2010.12.041.
- [36] H. Tawfik, Y. Hung, D. Mahajan, Metal bipolar plates for PEM fuel cell-A review, *J. Power Sources*. 163 (2007) 755–767. doi:10.1016/j.jpowsour.2006.09.088.

- [37] E.. Cho, U.-S. Jeon, H.. Ha, S.-A. Hong, I.-H. Oh, Characteristics of composite bipolar plates for polymer electrolyte membrane fuel cells, *J. Power Sources*. 125 (2004) 178–182. doi:10.1016/j.jpowsour.2003.08.039.
- [38] A. Shanian, O. Savadogo, TOPSIS multiple-criteria decision support analysis for material selection of metallic bipolar plates for polymer electrolyte fuel cell, *J. Power Sources*. 159 (2006) 1095–1104. doi:10.1016/j.jpowsour.2005.12.092.
- [39] J. Wind, R. Späh, W. Kaiser, G. Böhm, Metallic bipolar plates for PEM fuel cells, in: *J. Power Sources*, 2002: pp. 256–260. doi:10.1016/S0378-7753(01)00950-8.
- [40] V. V. Nikam, R.G. Reddy, Copper alloy bipolar plates for polymer electrolyte membrane fuel cell, *Electrochim. Acta*. 51 (2006) 6338–6345. doi:10.1016/j.electacta.2006.04.019.
- [41] X. Li, I. Sabir, Review of bipolar plates in PEM fuel cells: Flow-field designs, *Int. J. Hydrogen Energy*. 30 (2005) 359–371. doi:10.1016/j.ijhydene.2004.09.019.
- [42] M.C.L. De Oliveira, G. Ett, R.A. Antunes, Materials selection for bipolar plates for polymer electrolyte membrane fuel cells using the Ashby approach, *J. Power Sources*. 206 (2012) 3–13. doi:10.1016/j.jpowsour.2012.01.104.
- [43] H. Wang, M.A. Sweikart, J.A. Turner, Stainless steel as bipolar plate material for polymer electrolyte membrane fuel cells, *J. Power Sources*. 115 (2003) 243–251. doi:10.1016/S0378-7753(03)00023-5.

- [44] V. Mehta, J.S. Cooper, Review and analysis of PEM fuel cell design and manufacturing, *J. Power Sources*. 114 (2003) 32–53. doi:10.1016/S0378-7753(02)00542-6.
- [45] R.L. Borup, N.E. Vanderborgh, Design and testing criteria for bipolar plate materials for PEM fuel cell applications, in: *Mater. Res. Soc. Symp. - Proc.*, 1995: pp. 151–155. <http://www.scopus.com/inward/record.url?eid=2-s2.0-0029530337&partnerID=40&md5=09907abb31872c6ae71f04c811333ee0>.
- [46] I. Chang, T. Park, J. Lee, M.H. Lee, S.H. Ko, S.W. Cha, Bendable polymer electrolyte fuel cell using highly flexible Ag nanowire percolation network current collectors, *J. Mater. Chem. A*. 1 (2013) 8541. doi:10.1039/c3ta11699a.
- [47] I. Chang, T. Park, J. Lee, H.B. Lee, S. Ji, M.H. Lee, et al., Performance enhancement in bendable fuel cell using highly conductive Ag nanowires, *Int. J. Hydrogen Energy*. 39 (2014) 7422–7427. doi:10.1016/j.ijhydene.2014.03.017.
- [48] T. Park, I. Chang, J. Lee, S.H. Ko, S.W. Cha, Performance Variation of Flexible Polymer Electrolyte Fuel Cell with Ag Nanowire Current Collector under Torsion, *ECS Trans*. 64 (2014) 927–934. doi:10.1149/06403.0927ecst.
- [49] I. Chang, T. Park, J. Lee, H.B. Lee, S.H. Ko, S.W. Cha, Flexible fuel cell using stiffness-controlled endplate, *Int. J. Hydrogen Energy*. 41 (2016) 6013–6019. doi:10.1016/j.ijhydene.2016.02.087.
- [50] T. Park, I. Chang, J.H. Jung, H.B. Lee, S.H. Ko, S.J. Yoo, et al., Effect of Assembly Pressure on the Performance of a Bendable Polymer Electrolyte

- Fuel Cell Based on a Silver Nanowire Current Collector, *J. Power Sources*. (2016) Submitted.
- [51] T. Park, I. Chang, H.B. Lee, S.H. Ko, S.W. Cha, Performance Variation of Bendable Polymer Electrolyte Fuel Cell Based on Ag Nanowire Current Collector under Mixed Bending and Twisting Load, *Int. J. Hydrogen Energy*. (2016) Submitted.
- [52] P. Lee, J. Lee, H. Lee, J. Yeo, S. Hong, K.H. Nam, et al., Highly stretchable and highly conductive metal electrode by very long metal nanowire percolation network, *Adv. Mater.* 24 (2012) 3326–3332. doi:10.1002/adma.201200359.
- [53] S. De, T.M. Higgins, P.E. Lyons, E.M. Doherty, P.N. Nirmalraj, W.J. Blau, et al., Silver nanowire networks as flexible, transparent, conducting films: Extremely high DC to optical conductivity ratios, *ACS Nano*. 3 (2009) 1767–1774. doi:10.1021/nn900348c.
- [54] A. Kumar, C. Zhou, The race to replace tin-doped indium oxide: Which material will win?, *ACS Nano*. 4 (2010) 11–14. doi:10.1021/nn901903b.
- [55] J.Y. Lee, S.T. Connor, Y. Cui, P. Peumans, Solution-processed metal nanowire mesh transparent electrodes, *Nano Lett.* 8 (2008) 689–692. doi:10.1021/nl073296g.
- [56] A.R. Madaria, A. Kumar, F.N. Ishikawa, C. Zhou, Uniform, highly conductive, and patterned transparent films of a percolating silver nanowire network on rigid and flexible substrates using a dry transfer technique, *Nano Res.* 3 (2010) 564–573. doi:10.1007/s12274-010-0017-5.

- [57] A.R. Rathmell, S.M. Bergin, Y.L. Hua, Z.Y. Li, B.J. Wiley, The growth mechanism of copper nanowires and their properties in flexible, transparent conducting films, *Adv. Mater.* 22 (2010) 3558–3563.
doi:10.1002/adma.201000775.
- [58] Y. Sun, B. Mayers, T. Herricks, Y. Xia, Polyol Synthesis of Uniform Silver Nanowires: A Plausible Growth Mechanism and the Supporting Evidence, *Nano Lett.* 3 (2003) 955–960. doi:10.1021/nl034312m.
- [59] B. Wiley, Y. Sun, Y. Xia, Polyol Synthesis of Silver Nanostructures: Control of Product Morphology with Fe(II) or Fe(III) Species, *Langmuir.* 21 (2005) 8077–8080. doi:10.1021/la050887i.
- [60] H. Chen, Y. Gao, H. Zhang, L. Liu, H. Yu, H. Tian, et al., Transmission-Electron-Microscopy Study on Fivefold Twinned Silver Nanorods, *J. Phys. Chem. B.* 108 (2004) 12038–12043. doi:10.1021/jp048023d.
- [61] J.G. Pharoah, K. Karan, W. Sun, On effective transport coefficients in PEM fuel cell electrodes: Anisotropy of the porous transport layers, *J. Power Sources.* 161 (2006) 214–224. doi:10.1016/j.jpowsour.2006.03.093.
- [62] S.W. Cha, R. O’Hayre, Y. Il Park, F.B. Prinz, Electrochemical impedance investigation of flooding in micro-flow channels for proton exchange membrane fuel cells, *J. Power Sources.* 161 (2006) 138–142.
doi:10.1016/j.jpowsour.2006.04.123.
- [63] S. Asghari, A. Mokmeli, M. Samavati, Study of PEM fuel cell performance by electrochemical impedance spectroscopy, in: *Int. J. Hydrogen Energy*, 2010: pp. 9283–9290. doi:10.1016/j.ijhydene.2010.03.069.

- [64] Y.H. Lee, T. Park, I. Chang, S. Ji, S.W. Cha, Metal-coated polycarbonate monopolar plates for portable fuel cells, *Int. J. Hydrogen Energy*. 37 (2012) 18471–18475. doi:10.1016/j.ijhydene.2012.09.017.
- [65] N.P. Suh, An overview of the delamination theory of wear, *Wear*. 44 (1977) 1–16. doi:10.1016/0043-1648(77)90081-3.
- [66] S. Hosmane, A. Fournier, R. Wright, L. Rajbhandari, R. Siddique, I.H. Yang, et al., Valve-based microfluidic compression platform: single axon injury and regrowth, *Lab Chip*. 11 (2011) 3888. doi:10.1039/c1lc20549h.
- [67] Y.-S. Yu, Y.-P. Zhao, Deformation of PDMS membrane and microcantilever by a water droplet: Comparison between Mooney–Rivlin and linear elastic constitutive models, *J. Colloid Interface Sci.* 332 (2009) 467–476. doi:10.1016/j.jcis.2008.12.054.
- [68] S.-H. Yoon, V. Reyes-Ortiz, K.-H. Kim, Y.H. Seo, M.R.K. Mofrad, Analysis of Circular PDMS Microballoons With Ultralarge Deflection for MEMS Design, *J. Microelectromechanical Syst.* 19 (2010) 854–864. doi:10.1109/JMEMS.2010.2049984.
- [69] S.J. Lee, J.C.-Y. Chan, K.J. Maung, E. Rezler, N. Sundararajan, W.S.T. Nguyen N-T, et al., Characterization of laterally deformable elastomer membranes for microfluidics, *J. Micromechanics Microengineering*. 17 (2007) 843–851. doi:10.1088/0960-1317/17/5/001.
- [70] D. Natarajan, T. Van Nguyen, Current distribution in PEM fuel cells. Part 1: Oxygen and fuel flow rate effects, *AIChE J.* 51 (2005) 2587–2598. doi:10.1002/aic.10545.

- [71] D. Armani, C. Liu, N. Aluru, Re-configurable fluid circuits by PDMS elastomer micromachining, in: Tech. Dig. IEEE Int. MEMS 99 Conf. Twelfth IEEE Int. Conf. Micro Electro Mech. Syst. (Cat. No.99CH36291), IEEE, 1999: pp. 222–227. doi:10.1109/MEMSYS.1999.746817.
- [72] I. Chang, T. Park, J. Lee, H.B. Lee, S.H. Ko, S.W. Cha, Flexible fuel cell using stiffness-controlled endplate, *Int. J. Hydrogen Energy*. (2016) In press.
- [73] J. Ge, A. Higier, H. Liu, Effect of gas diffusion layer compression on PEM fuel cell performance, *J. Power Sources*. 159 (2006) 922–927. doi:10.1016/j.jpowsour.2005.11.069.
- [74] H.S. Chu, C. Yeh, F. Chen, Effects of porosity change of gas diffuser on performance of proton exchange membrane fuel cell, *J. Power Sources*. 123 (2003) 1–9. doi:10.1016/S0378-7753(02)00605-5.
- [75] S.J. Lee, C.D. Hsu, C.H. Huang, Analyses of the fuel cell stack assembly pressure, *J. Power Sources*. 145 (2005) 353–361. doi:10.1016/j.jpowsour.2005.02.057.
- [76] W.K. Lee, C.H. Ho, J.W. Van Zee, M. Murthy, Effects of compression and gas diffusion layers on the performance of a PEM fuel cell, *J. Power Sources*. 84 (1999) 45–51. doi:10.1016/S0378-7753(99)00298-0.
- [77] Y. Zhou, G. Lin, a. J. Shih, S.J. Hu, Multiphysics Modeling of Assembly Pressure Effects on Proton Exchange Membrane Fuel Cell Performance, *J. Fuel Cell Sci. Technol*. 6 (2009) 041005. doi:10.1115/1.3081426.
- [78] Y.-H. Lai, D.P. Miller, C. Ji, T.A. Trabold, Stack Compression of PEM Fuel Cells, in: 2nd Int. Conf. Fuel Cell Sci. Eng. Technol., ASME, 2004: pp. 567–

571. doi:10.1115/FUELCELL2004-2522.

- [79] J.M. Gere, *Mechanics of Materials*, 6th ed., Thomson, Nelson, 2006.
- [80] T. Park, I. Chang, Y.H. Lee, S. Ji, S.W. Cha, Analysis of operational characteristics of polymer electrolyte fuel cell with expanded graphite flow-field plates via electrochemical impedance investigation, *Energy*. 66 (2014) 77–81. doi:10.1016/j.energy.2013.11.051.
- [81] W. Vielstich, A. Lamm, H.A. Gasteiger, *Handbook of Fuel Cells*, vol. 3, John Wiley & Sons, New York, 2003.
- [82] T.E. Springer, T.A. Zawodzinski, S. Gottesfeld, Polymer electrolyte fuel cell model, *J. Electrochem. Soc.* 138 (1991) 2334–2342. doi:10.1149/1.2085971.

국 문 초 록

21 세기에 접어들면서 전자기기 관련 기술은 다양한 방면에서 괄목할 만한 발전을 일궈냈으며, 이러한 전자기기를 위한 에너지원 또한 기술적으로 많은 발전을 해왔다. 이 발전은 또한 여러 전자기기를 소형화하여 휴대용 전자기기를 위한 에너지원에 대한 기술적 수요를 증가시켰다. 현재 리튬 기반의 이차전지가 현재 그 기술 수요에 대한 시대적 패러다임을 장악하고 있으며 휴대전자기기 대부분의 분야의 에너지원으로 사용되고 있으나, 현재 리튬 전지 기술은 에너지 밀도에 있어서 이론적 한계치에 근접해 더 이상의 무게 및 부피 대비 에너지 밀도를 향상시키기는 불가능하다. 그러나 다른 전자기기 부품에 대한 성능은 더욱 고도화되어 휴대용 에너지원에 있어 더 많은 에너지 밀도가 요구되는 실정이다. 따라서 본 리튬 전지를 대체할 만한 미래 에너지원에 대한 개발이 필요하다.

또다른 미래 전자기기 변화의 경향은 본 전자기기가 ‘유연성’을 요구한다는 것이다. 플렉서블 디스플레이 및 이를 적용한 굽힘형 스마트폰 등이 현재 이미 출시되고 있는 등, 차세대 전자기기의 기술로 유연성을 지닌 웨어러블(Wearable) 및 피부이식 전자기기가 각광받고 있다. 웨어러블 전자기기 또한 휴대용 전자기기의 한 형태이므로

에너지원을 필요로 하고, 이것은 유연성과 고에너지밀도 모두를 갖춘 휴대용 에너지원이 필요하다는 것을 뜻한다.

본 연구는 이러한 미래 에너지원에 대한 수요를 대응하기 위해 새로운 형태의 연료전지를 제안한다. 이른바 ‘굽힐 수 있는 연료전지’인 플렉서블 (Flexible) 연료전지는 현재 리튬 전지의 에너지 밀도의 한계를 극복할 수 있는 후보 기술인 연료전지에 유연성을 부여했다. 본 플렉서블 연료전지의 집전체로 사용된 Ag 나노와이어 네트워크는 길이를 늘이거나 굽혀도 전기전도성이 저하되지 않으며, 내부식성과 내화화성이 좋아 연료전지의 각 전극에서의 작동환경에 잘 견딜 수 있다. 이를 화학적으로 매우 안정한 폴리머의 일종인 PDMS (Polydimethylsiloxane)에 코팅하여 플렉서블 연료전지용 유로판 및 이를 이용하여 플렉서블 연료전지를 제작하였다.

플렉서블 연료전지는 굽힘의 정도에 따른 전기화학적 성능의 변화를 중심으로 성능을 평가하였으며, 비굽힘 상태에서는 43 mW/cm^2 , 굽힘 상태에서는 71 mW/cm^2 의 최대전력밀도를 보였다. 본 성능변화 경향은 유한 요소 해석기법을 이용하여 굽힘에 따른 내부 응력의 변화를 계산하여, MEA (Membrane-electrode assembly, 막-전극 집합체)에 수직방향으로 가해지는 응력이 굽힘에 따라 기하급수적으로 증가함에 따라 발생한 것으로 보였다. 각 플렉서블 연료전지의 굽힘반지름에 따라 분극곡선 외에 전기화학 임피던스를 측정한 결과, 굽힘이 증가할수록

전해질 저항과 전극저항이 모두 감소하여 성능이 증가했던 것을 확인하였다. 특히, 이 플렉서블 연료전지를 이용하여 전기모터를 돌리는데 성공함으로써 본 플렉서블 연료전지 기술의 수준이 상용화 전자기기수준에 근접함을 보였다.

그러나 굽힘이 아닌 뒤틀림 환경에서의 최대전력밀도는 이보다 낮은 17 mW/cm^2 를 보였다. 이는 MEA가 뒤틀림 환경에서는 심하게 손상된 데에서 기인한 것으로 추정된다. 뒤틀림에 대해서 굽힘과 동일하게 응력에 대한 유한요소해석 결과, 굽힘과 달리 뒤틀림 부하에서는 MEA가 위치한 부분의 응력의 변화가 거의 없었다. 그러나 뒤틀림에 따른 각 그리드의 변위 변화를 계산한 결과 굽힘과 달리 늘임(Strain)이 많이 나타나는 것을 확인했다. 이 늘임에 의해 핫프레스된 MEA의 GDL과 전해질막이 떨어져 전기화학적 삼상계면이 줄어들고, 유연성이 없는 GDL 자체의 손상으로 성능이 감소된 것으로 생각된다. 같은 MEA를 사용했을 때 굽힘 실험에서는 평평한 상태에서의 성능이 43 mW/cm^2 라는 것을 고려하면, 이는 뒤틀림 실험 대비 3배 이상 높은 수치이다. 따라서 일반 연료전지에서 사용되는 MEA를 플렉서블 연료전지에서 사용할 경우 굽힘에서는 비교적 고내구도를 보이거나 뒤틀림에서는 매우 취약한 내구성을 보이며, 이는 플렉서블 연료전지 전용 MEA의 개발이 필요함을 의미한다.

실제 플렉서블 연료전지가 사용되는 환경은 위에서 묘사한 굽힘

또는 뒤틀림이 아닌 굽힘과 뒤틀림이 섞인 환경이다. 따라서 이러한 복합 부하에서의 플렉서블 연료전지의 성능을 평가하였다. 본 실험에서는 굽힘에서는 두 가지 포지션, 평평한 상태와 굽힘반지름 36.3 cm, 뒤틀림에서는 5가지 뒤틀림각($0 \sim 25^\circ$, 5° 간격)에서 성능을 측정하였다. 분극 성능은 굽힘실험과 동일하게 굽힘상태에서는 뒤틀림 없이 최대전력밀도 27 mW/cm^2 였으며 순수 뒤틀림 시험과 같이 뒤틀림이 가해지게 되면 성능이 감소하는 경향을 보였다. 본 성능의 절대수치도 굽힘실험에서의 비굽힘 상태에서의 기본 성능인 43 mW/cm^2 에 비하면 매우 낮으며, 뒤틀림 실험에서 보인 MEA 손상으로 인해 성능이 저하된 결과와 일치한다. 이에 대한 내부응력 해석 결과 복합 부하에서 굽힘과 뒤틀림은 각각 독립적으로 MEA의 응력에 영향을 주는 것으로 확인됐으며, 굽힘 성분만 MEA에 수직방향 응력이 작용하는 것으로 확인됐다. 복합 부하에서 비록 뒤틀림에 의해 MEA가 손상되더라도 압축 응력에 의해 기존의 저하된 성능에 대하여도 상대적인 성능증가가 있는 것으로 보였다.

본 플렉서블 연료전지의 굽힘에 의한 성능 증가 원인이 압축응력에 의한 것임은 실험적으로도 증명됐다. 압축 응력을 정량적으로 측정하며 연료전지의 성능을 측정한 결과, 압축 응력이 계속적으로 증가하면 성능이 110 mW/cm^2 정도에서 수렴했다. 이는 기존의 굽힘 환경에서 실험하였을 때의 성능의 최대치로 볼 수 있으며, 플렉서블 연료전지의

성능이 구조적 개선을 통해 성능을 더욱 증가시킬 수 있음을 확인할 수 있다. 이 실험에선 전기화학적 성능을 정량적으로 측정된 굽힘응력 치수와 비교하여 압력과 성능에 관한 전기화학적 상수들의 데이터를 얻을 수 있으며, 이를 이용한 1차원 플렉서블 연료전지 모델링의 결과 기존의 실험결과에 매우 근접하였다. 본 모델을 기존의 문헌상 보고된 플렉서블 연료전지의 실험결과와 비교하였을 때도 잘 일치함을 확인했다. 이는 본 연료전지가 임의의 형상으로 있을 때에도 압력에 관한 계산이 선행되면 본 플렉서블 연료전지의 성능을 예측할 수 있음을 의미한다.

주요어: 플렉서블 연료전지, 고분자 전해질 연료전지, 분리판, 은 나노와이어, 플렉서블 전자기기, 폴리디메틸실록산

학 번: 2010-23216